Universidade de Vigo

EIDO.TC32

Formulario/Form EIDO - TC32. Membros tribunais e directores/as / Jury members and supervisors

Datos persoais / Datos personales / Personal data

Apelidos(s) / Apellido(s) / Surname(s):	Amin El-Sakka
Nome / Nombre / First-Middle name(s):	Ragab Riad
Sexo / Sex:	Male
Data de nacemento / Fecha de nacimiento / Birth date:	14 – 12 - 1961
Nacionalidade / Nacionalidad /Nationality:	Egyptian
DNI-pasaporte / ID-passport:	A30029972
Enderezo para notificacións / Dirección para notificaciones / Correspondence address:	Prof. Of Chemistry, Basic Science department, Faculty of Engineering, Nahda University , Beni – Sueff – EGYPT www.nub.edu.eg
Teléfono / Phone no.:	+201023806704
Correo electrónico / E-mail:	Ragab.amin@nub.edu.eg

Datos académicos / Academic data

Denominación do título de doutor/a / Denominación del título de doctor/a / Doctorate degree:	***Ph.D. degree:*** *Inorganic Chemistry, Chemistry department, Faculty of Science, Ain Shams University, 24th December 1994.*
Univ. de expedición / University issuing the doctoral degree:	Universidad de Ain Shams – Cairo, Egypt
Ano do título / Año del título / Year of the doctoral degree:	1994

Datos profesionais / Datos profesionales / Professional data

Centro / Centre:	***https://scholar.google.com/citations?hl=en&user=epvBjEYAAAAJ&view_op=list_works***
Categoría profesional / Professional position:	
Situación / Status:	
Liñas de investigación / Líneas de investigación / Research lines:	

Méritos de investigación / Research requirements: Sexenios (only Spanish instructors)

Sexenio: ano_inicio, ano_final (sistema universitario español) / Sexenio: año_inicio, año_final / (Only for Spanish professors):	

Méritos de investigación / Research requirements: Patente / Patent

Denominación de patente en explotación / Title of patent in use:	
Inventor/a(/es/as) / Inventor(s):	
Número de patente / Patent number:	
Data de concesión / Fecha de concesión / Date of patent granting:	
Entidade titular / Entidad titular / Patent holder entity:	
Entidade que explota a patente / Entidad que explota la patente / Entity using the patent:	
Enlace a documentación / Link to documents:	

Méritos de investigación / Research requirements: IP dun proxecto de I+D+i / IP de un proyecto de I+D+i / PI of a R&D project

Título do proxecto / Título del proyecto / Project title:	
Referencia do proxecto / Referencia del proyecto / Project code:	
Entidade financiadora / Entidad financiadora / Funding body:	

Duración (data inicio/fin) / (fecha inicio/fin) / Duration (start/end dates):

Méritos de investigación / Research requirements: Artigo/Artículo/Article I

1) Nome da revista / Nombre de la revista / Journal name:
1) Autores/as / Author(s):
1) Título do artigo / Título del artículo / Article title:
1) ISSN:
1) Ano da publicación / Año de la publicación / Year of publication:
1) Enlaces xustificativos do impacto / Enlaces justificativos del impacto / Links to impact information:

Electro-synthesis approach for some metal ion complexes derived from thiosemicarbazide; characterization, conformational, inhibitory simulation and Hirshfeld surface properties

2020

Appl Organomet Chem. 2020;e5766. Wileyonlinelibrary.com/journal/aoc 2020 John Wiley & Sons, Ltd**, pages 1-13, April 2020 (I.F. 3.14)**

Méritos de investigación / Research requirements: Artigo/Artículo/Article II

2) Nome da revista / Nombre de la revista / Journal name:
2) Autores/as / Author(s):
2) Título do artigo / Título del artículo / Article title:
2) ISSN:
2) Ano da publicación / Año de la publicación / Year of publication:
2) Enlaces xustificativos do impacto / Enlaces justificativos del impacto / Links to impact information:

Journal of Molecular Liquids 309 (2020) 113119**,** Available online 15 April 2020**, (I.F. 5.0).**

Moamen Refat, Nashwa El-Metwaly, Ali Sayqal, Ismail Althagafi, Hana M. Abumelha, Hanadi Katouah, Amerah M. Al-Solimy, Reem Shah, **Ragab R. Amin**, Yamany B. Yamany, Jehan Y. Al-Humaidi

Elaborated computational studies for Zn(II) and Sn(II) complexes, electro-synthesis, spectral, thermal and electrochemical analysis

2020

Méritos de investigación / Research requirements: Artigo/Artículo/Article III

3) Nome da revista / Nombre de la revista / Journal name:
3) Autores/as / Author(s):
3) Título do artigo / Título del artículo / Article title:
3) ISSN:
3) Ano da publicación / Año de la publicación / Year of publication:
3) Enlaces xustificativos do impacto / Enlaces justificativos del impacto / Links to impact information:

25 May 2020, Springer-Verlag GmbH Germany, part of Springer Nature, Environmental Science and Pollution Research, https://doi.org/10.1007/s11356-020-09431-7, **(May 2020-I.F. 4.0).**

Mohamed Shaban, Ahmed Hamd, Ragab R. Amin, Mostafa R. Abukhadra, Ahmed Abdel Khalek, Aftab Aslam Parwaz Khan & Abdullah M. Asiri

Preparation and characterization of MCM-48/nickel oxide composite as an efficient and reusable catalyst for the assessment of photocatalytic activity

Preparation and characterization of MCM-48/nickel oxide composite as an efficient and reusable catalyst for the assessment of photocatalytic activity

2020

Méritos de investigación / Research requirements: Dirección de teses / Dirección de tesis / PhD supervision

Título da tese / Título de la tesis / Thesis title:	
Autor/a / Author:	
Universidade / Universidad / University:	
Cualificación / Calificación / Grade:	
Data de defensa / Fecha de defensa / Viva date:	
Título do artigo derivado da tese / Título do artículo derivado de la tesis / Title of the rticle derived from the thesis:	
Nome da revista / Nombre de la revista / Journal name:	
ISSN:	
Autores/as / Author(s):	

Ano da publicación / Año de la publicación / Year of publication:	

Méritos de investigación / Research requirements: outros méritos / otros méritos / other contributions

Mérito 1 / Merit 1 (se é unha publicación, indíquese ISSN/ISBN y título / si es una publicación, indíquese ISSN/ISBN y título / if this is a publication, indicate ISSN/ISBN and title):	
Mérito 2 / Merit 2 (se é unha publicación, indíquese ISSN/ISBN y título / si es una publicación, indíquese ISSN/ISBN y título / if this is a publication, indicate ISSN/ISBN and title):	
Mérito 3 / Merit 3 (se é unha publicación, indíquese ISSN/ISBN y título / si es una publicación, indíquese ISSN/ISBN y título / if this is a publication, indicate ISSN/ISBN and title):	
Mérito 4 / Merit 4 (se é unha publicación, indíquese ISSN/ISBN y título / si es una publicación, indíquese ISSN/ISBN y título / if this is a publication, indicate ISSN/ISBN and title):	
Mérito 5 / Merit 5 (se é unha publicación, indíquese ISSN/ISBN y título / si es una publicación, indíquese ISSN/ISBN y título / if this is a publication, indicate ISSN/ISBN and title):	

Sinatura / Firma / Signature

A persoa asinante declara que os datos son certos e acepta a normativa da UVigo / La persona firmante declara que los datos son ciertos y acepta la normativa de la UVigo / The person signing herein declares that this information is correct and accepts the regulations of UVigo.:	
Acepta dirixir a tese de doutoramento indicada abaixo / Acepta dirigir la tesis doctoral indicada abajo / Acceps to supervise the doctoral doctoral dissertation indicated below:	
Acepta ser membro do tribunal que xulgará a tese de doutoramento indicada abaixo / Acepta ser miembro del tribunal que juzgará la tesis doctoral indicada abajo / Accepts to join the examination board responsible for the assessment of the doctoral dissertation indicated below:	
Doutorando/a / Doctorando/a / PhD student:	Abdelrahman Hamdeldein Geneidy Aly
Lugar e data / Lugar y fecha / Place and date (Este formulario asinado manual ou dixitalmente debe enviarse a / Este formulario firmado manual o digitalmente debe enviarse a / This form, signed manually or digitally, must be sent to: Escola Internacional de Doutoramento. Edificio Filomena Dato, 1º andar. Campus Universitario. E-36310 Vigo; 3ciclo1@uvigo.es):	

PROPOSTA DO TRIBUNAL DA TESE DE DOUTORAMENTO

PROGRAMA DE DOCTORADO/PROGRAMA DOUTORAMENTO: Ciencia e Tecnoloxía de Coloides e Interfaces

TÍTULO DA TESE: Design of Transition Metal Oxide-based Nanomaterials for Environmental Applications
DOUTORANDO: Abdelrahman Hamdeldein Geneidy Aly
DNI/NIE/PASAPORTE: 60270864P PASAPORTE **PAS416237**
DIRECTOR/A/AS/ES DA TESE: Miguel A. Correa Duarte / Begoña Puértolas Lacambra

PROPOSTA DE COMPOSICIÓN DO TRIBUNAL

	Apelidos e Nome	Universidade ou Institución	Proposta
1	Salgueiriño Maceira, Verónica	Universidade de Vigo	Presidenta
2	Carbo Argibay, Enrique	Laboratorio Ibérico Internacional de Nanotecnología	Secretario
3	Amin El-Sakka, Ragab Riad	Nahda University , Beni – Sueff – EGYPT	Vocal
4	Comesaña Hermo, Miguel	Université Paris Cité, Laboratoire ITODYS	Suplente Pres.
5	Vázquez González, Margarita	Universidade de Vigo	Suplente Secr.
6	Del Pino González de la Higuera, Pablo Alfonso	Universidad De Santiago de Compostela	Suplente Vocal
7	Rodríguez Lorenzo, Laura	Laboratorio Ibérico Internacional de Nanotecnología	Suplente

Vigo, 25 de 6 de 2024

O Presidente/a da Comisión Académica/*El Presidente de la Comisión Académica*

Universidade Vigo
Servizo de Xestión de Estudos de Posgrao
Escola Internacional de Doutoramento (EIDO)

ASUNTO: Autorización participación por videoconferencia

Debido a la imposibilidad de traslado de Don/Doña Ragab Riad Amin El-Sakka vocal del tribunal que juzgará la tesis doctoral de Abdelrahman Hamdeldein Geneidy Aly, al acto de defensa de la citada tesis y, en aplicación del artículo 38 del Reglamento de Estudios de Doctorado de la Universidad de Vigo, se autoriza su participación por videoconferencia.

Vigo, 28 de octubre de 2024
El Director de la Escuela Internacional de Doctorado

Antonio Collazo Fernández

Documento firmado electrónicamente

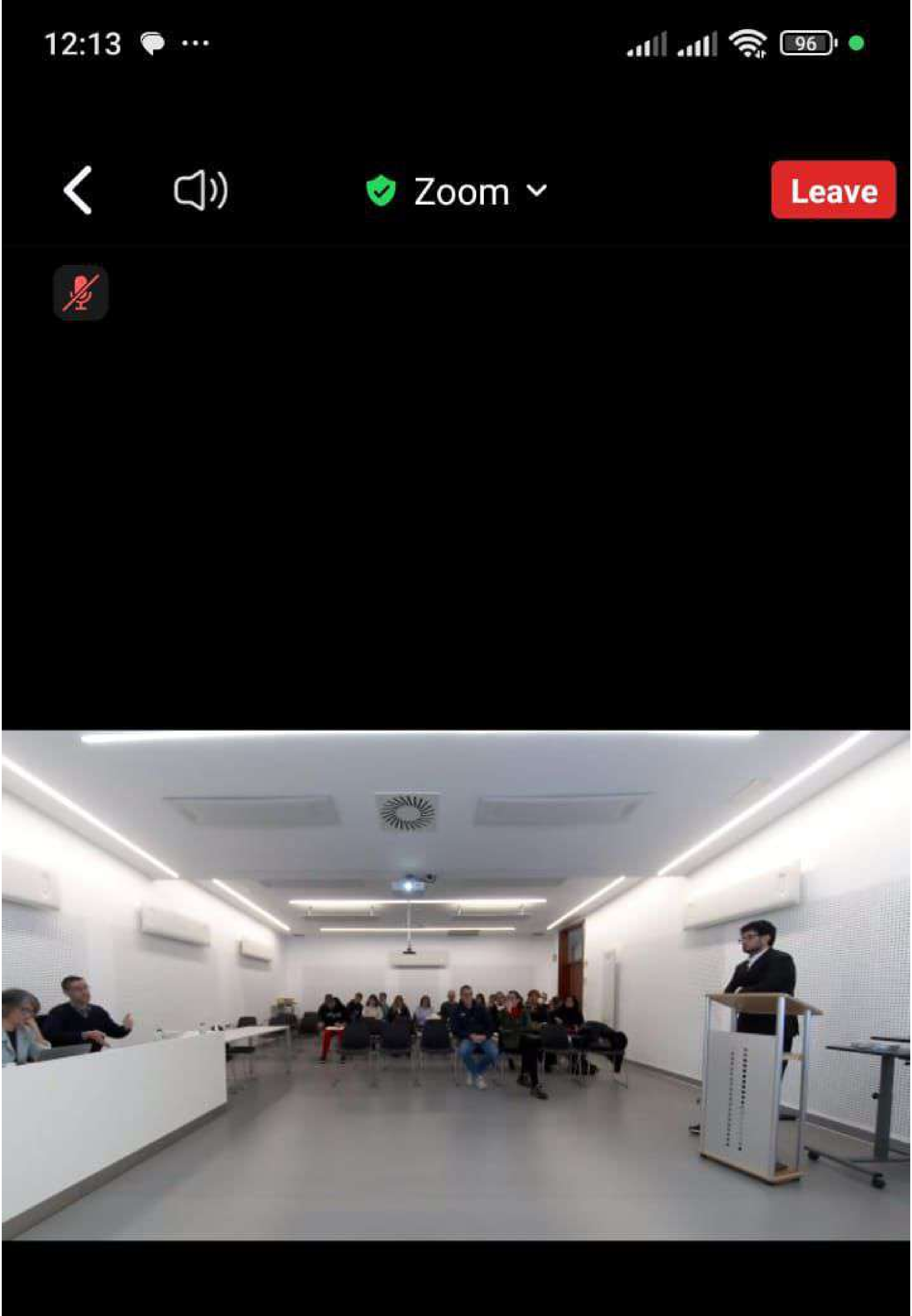
12:13
96
Zoom
Leave


Au NRs
CdS QDs
TiO2
SiO2

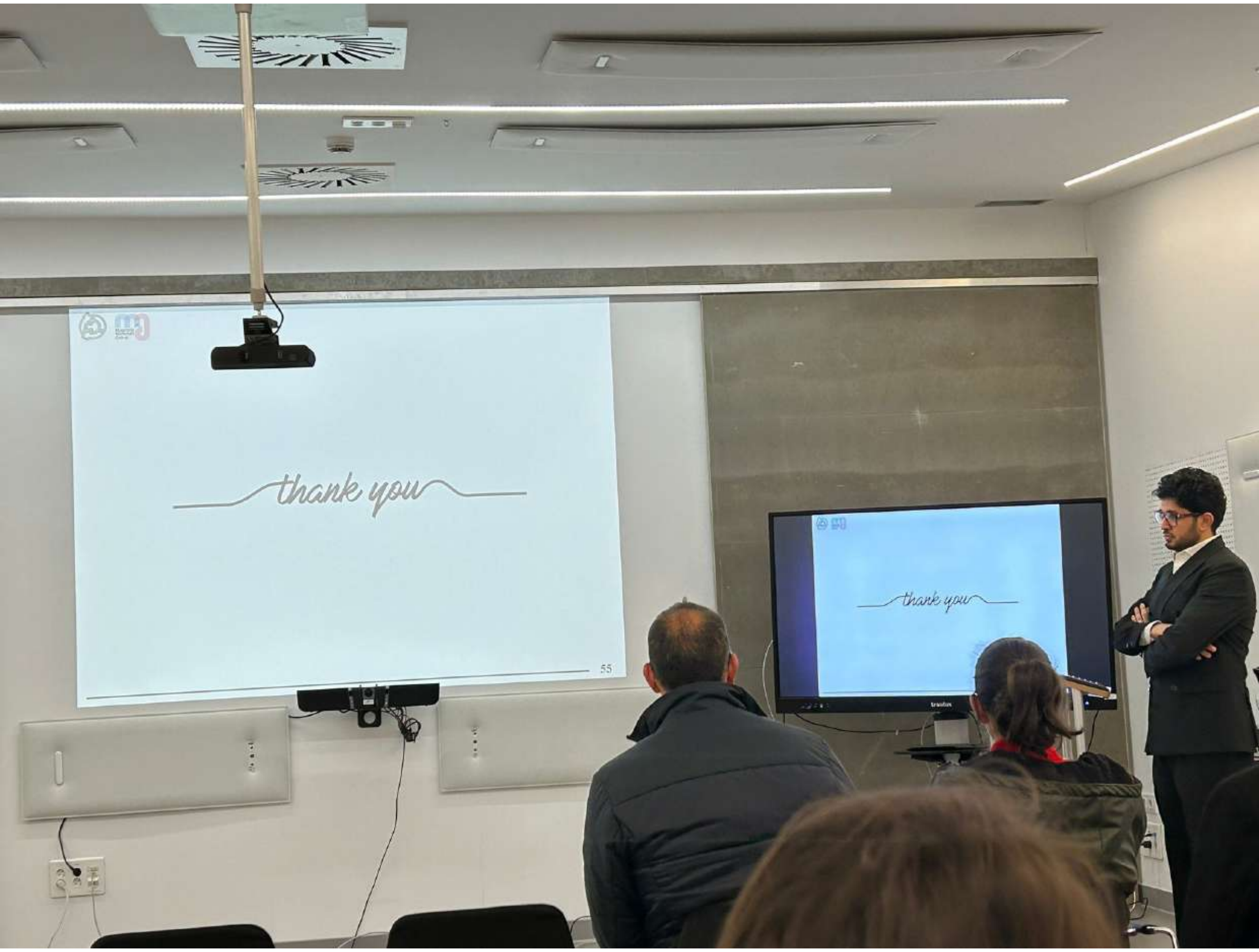
thank you
55
thank you

Universidade Vigo

DOCTORAL DISSERTATION

Design of Transition Metal Oxide-based Nanomaterials for Environmental Applications

Abdelrahman Hamdeldein Geneidy Aly

2024

Universidade Vigo

EIDO
Escola Internacional
de Doutoramento

UniversidadeVigo

International Doctoral School

Abdelrahman Hamdeldein Geneidy Aly

DOCTORAL DISSERTATION

Design of Transition Metal Oxide-based Nanomaterials for Environmental Applications

Supervised by:

D. MIGUEL Á. CORREA DUARTE

D. Begoña Puértolas Lacambra

UniversidadeVigo

International Doctoral School

Dr. Miguel Ángel Correa Duarte and Dr. Begoña Puértolas Lacambra

DECLARE that the present work, entitled "Design of Transition Metal Oxide-based Nanomaterials for Environmental Applications", submitted by Abdelrahman Hamdeldein Geneidy Aly to obtain the title of Doctor, was carried out under their supervision in the PhD programme in "science and technology of colloids and interfaces.

The supervisors,   Vigo,   de   2024

ACKNOWLEDGEMENT

No words can ever express my sincere gratitude to **Allah** who guides, aids, and blesses me in everything and everywhere in my life. Also, I need to confirm my deep gratitude to **Allah** that he sent us **prophet Mohamed**, the Prophet of peace and mercy.

I would like to express my deep thanks to **Dr. MIGUEL Á. CORREA DUARTE and Dr. Begoña Puértolas Lacambra*u*,** for their always provided valuable support and guidance. Without their kindest help and encouragement, this project would not be possible.

I owe great support sincere love to my family, my wife, son, father, mother, siblings, and my dear friends who stood beside me during difficult and hard times.

Abdelrahman Hamdeldein

Content

Thesis scope

This doctoral thesis tackles the fabrication of transition metal oxides (TMO)-based nanoparticles (NPs) and their utilization in relevant environmental applications including renewable energy production and water treatment. The synthesized particles are classified into two main classes: nickel cobaltite nanosheets ($NiCo_2O_4$), and Cobalt-nickel mixed oxide nanoparticles with different Ni:Co molar ratios prepared *via* hydrothermal synthesis for formate production in direct methanol fuel cells (DMFCs), and plasmonic quantum dots nanohybrids composed by cadmium sulfide quantum dots (CdS, QDs), titanium dioxide (TiO_2), and Au NPs as building blocks. The efficiency of the developed materials to absorb more light of the electromagnetic spectrum (visible band) was evaluated via catalytic activity. These hybrids were implemented for Rhodamine B (RB) degradation and removal; they offered a superior photocatalytic activity in the visible and near-IR regions. These hybrids can find wide environmental applications particularly wastewater treatment.

Outline of the Thesis

This work has been carried out at Universidade de Vigo. Part of the results included here have been obtained in collaboration with external groups that have contributed with complementary inputs ranging from theoretical modeling to advanced characterization of the synthetized materials.

This dissertation has been structured in four main chapters. Chapter 1 tackles a brief summary on the nanoscale features in materials science including a short description of the chemical methods which have been used to synthesize the reported nanomaterials, and the assembly protocols applied to fabricate the nanohybrids. Different synthetic protocols including colloidal, hydrothermal, and layer by layer approaches are discussed. Chapter 2 presents the development of an Au@CdS@TiO_2 nanohybrid by a layer by layer technique with a high ability for light-harvesting in the visible electromagnetic spectrum that can suppress the charge recombination as well as supply reactive sites for photocatalysis. The synthesized catalyst is tested in Rhodamine B degradation as a model reaction of waste water treatment. It is good to mention that this fabrication process proceeded with theoretical study to hypothesize the more suitable crystallographic structure for the new catalysis system as well as a prediction for the surface interaction energies between the catalyst and the RB dye that maybe found in the wastewater stream. Chapter 3 reports nickel cobaltite nanosheets and Cobalt-nickel mixed oxide nanoparticles as catalysts for methanol oxidation to formate. The synthesized $NiCo_2O_4$ exhibits nearly 100% electrochemical conversion of methanol to formate, which was rationalized *via* a set of characterization techniques that includes XRD, SEM-EDS, HRTEM, and ICP-OES. Chapter 4 summarizes the key conclusions and implications of this work in a wider context and identifies future challenges and research directions.

Chapter 1

1. Introduction

World overpopulation imposes significant pressure on environmentally sustainable energy resources. More recently, much attention has been directed to renewable energy resources as well as water pollution treatment. The careful engineering of advanced nanomaterials offers novel features to face the future energy demand including the design of solar cells, supercapacitors, or photocatalysts to produce sustainable fuels or reduce water pollution *via* photo-degradation. Nonrenewable energy faces significant challenges, including limited production capacity and additional contamination such as the harmful gases: COx, SOx, and NOx, these gases can cause hazardous problems for humans, animal, and all environments [1].

1.1 Nanotechnology and Nanomaterials

Nanotechnology involves the manipulation of matter at the nanoscale at dimensions between 1 and 100 nm to produce new structures, materials, and devices [2]. Feynman highlighted in his classical science lecture entitled "There's Plenty of Room at the Bottom" the primary differences in materials properties at bulk and nanoscales [3]. While bulk materials demonstrate constant physical properties regardless of its size, the laws of quantum physics, rather than classical physics, start to control the performance of the material and its behavior at the nanoscale [4, 5]. For instance, metallic compounds such as copper that are opaque at the bulk scale become transparent at the nanoscale; inert bulk platinum exhibits catalytic properties when it is in the form of nanoparticles; silicon that is an insulator at the bulk scale behaves as a conductor at the nanoscale, *etc.*

1.2 Synthesis of nanomaterials

Nanoparticle synthesis with uniform size, crystalline structure and controlled stoichiometry is a great aim for scientists and researchers. To this aim, many methods have been developed to synthesize nanostructured materials [11, 12], which can be classified into two main categories: top-down and bottom-up approaches (Figure 1.1) [6, 7].

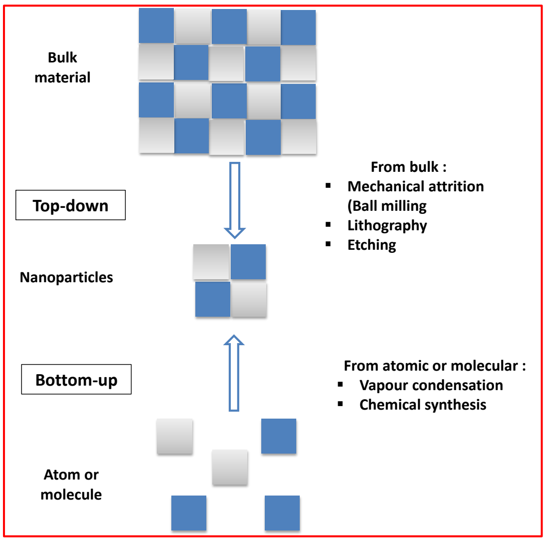

Fig. 1.1: Nanomaterial synthesis and assembly approaches

The top-down synthetic procedures begin with the bulk of a material whose size is reduced to the nanometric size *via* mechanical milling, lithography, and other forms of energy, being ball milling the most widely used. On the contrary, in the bottom-up synthetic protocols, molecules or atomic components area used as construction units for the development of complex structures. This approach enables the nanomaterial synthesis *via* vapor condensation/deposition or chemical reactions using molecule by molecule, atom by atom, layer by layer, or cluster by cluster such as the colloidal dispersion, hydrothermal synthesis, chemical vapor deposition, plasma arcing, electrodeposition, and sol-gel synthesis, among others. This technique provides a large variety of structures in a controlled manner. However, particle size control, particle agglomeration, and reaction completion are the main difficulties facing this technique.

1.2.1 Hydrothermal synthesis

Hydrothermal synthesis refers to any homogenous or heterogeneous reaction in an aqueous solvent under controlled conditions of temperature and pressure *by heating the reactants to their critical point.* The adequate selection of temperature, pH, and reactant concentrations enable a precise morphology control, narrow particle size distribution, and controlled stoichiometry with downstream consequences in the catalytic activity. It allows synthesis reproducibility, scalability, and superior nanostructure control. It is generally conducted under batch conditions using autoclaves although there have been many attempts to establish continuous hydrothermal synthesis techniques. The vapor/liquid phase boundary diminishes near the critical point; as the gas becomes denser and the liquid becomes less dense. Above the critical point, the phase boundary disappears and a homogenous supercritical phase exists (Figure 1.2).

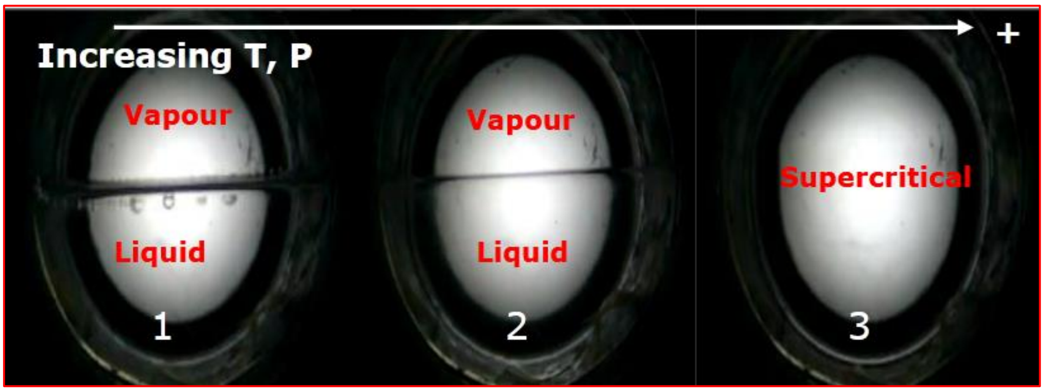

Fig. 1.2: Phase boundary of fluid with temperature and pressure adapted [8].

Water is the most common fluid for hydrothermal synthesis. Water dissociation constant (Kw) is represented by Equation 1.1 [9].

$$H_2O \leftrightarrow H^+ + \mathrm{OH}^- \qquad Kw = \frac{[H^+][OH^-]}{H_2O} \qquad \text{Eq. (1.1)}$$

Water has a constant K_w value of 1×10^{-14} mol/l [10]. Water dissociation constant increases orders of magnitude near its critical point. Therefore water becomes a suitable solvent for ionic compounds and free radical processing. However, Kw decreases radically over the critical point [11]. Figure 1.3, shows the changes in dielectric constant, density, and ionic product of water with temperature at 24 MPa.

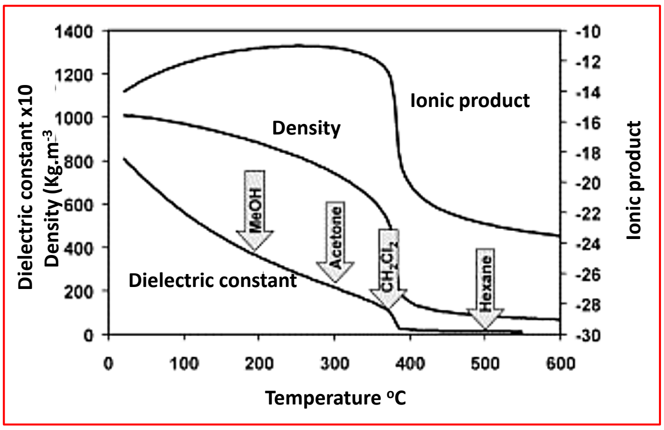

Fig. 1.3: Water properties versus temperature at 24 MPa, adapted from[12].

The enhanced OH^- level at the critical point can be exploited for nanoparticle synthesis. This can be achieved through hydrolysis of metal salt (Equation1.2) immediately followed by a dehydration step (Equation 1.3) [12].

$$Hydrolysis\ ML_x + \mathrm{xOH}^- \rightarrow H^+ + M(\mathrm{OH})_x + \mathrm{xL}^- \qquad \mathrm{Eq.\,(1.2)}$$

$$Dehydration\ \ M(\mathrm{OH})_x \rightarrow MO\frac{x}{2} + \frac{x}{2}\ H_2O \qquad \mathrm{Eq.\,(1.3)}$$

Synthesis of metal-oxide nanoparticles can be carried out through these two reactions [13].

1.2.2 Colloidal synthesis for plasmonic nanoparticles

The application of plasmonic nanoparticles with precisely controlled composition, size, shape, and surface chemistry in catalysis is gaining increasing attention. Common synthesis protocols include electron beam lithography (EBL), nanosphere lithography (NSL), and colloidal synthesis, the latter being a facile fabrication technique with high capability to develop complex structures. It enables the synthesis of plasmonic nanoparticles with different shapes, compositions, sizes, and surface chemistry by the appropriate selection of different capping, reducing agents, solvent systems, and reaction conditions [14-19]. Nobel metal NPs such as gold (Au), platinum (Pt), and silver (Ag) are among the most important plasmonic materials. Colloidal Ag and Au NPs can experience strong absorption in the

UV/visible spectral range due to Localized Surface Plasmon Resonance (LSPR) phenomenon. This results in high intense surface plasmon absorption bands and local electromagnetic field enhancement, which broaden the signal for several optical applications such as enhanced Raman surface scattering [20-22], surface infrared absorption [23], and enhanced surface fluorescence [24-26]. The LSPR enhancement depends on the shape, composition, and size of the NPs, and the dielectric properties of the surrounding medium [27-30]. Coupling of noble metal NPs with semiconductors could lead to enhanced catalytic properties which could be ascribed to the localization of the plasmonic material in the hybrid and the resonance effect over the semiconductor materials that generally host the active sites for catalysis. Upon irradiation, the electrons are transferred to the conducting band and then then go through the surface that increases the optical absorption regions. Therefore, incorporating the plasmonic material not only enhances the light absorption but also widens the absorption region of the semiconductor.

1.2.3 Hybrid structure using layer by layer (LBL) method

Among these rationalistic methods that have been developed recently, LBL construction method which is used to synthesize hybrids with new functionalities, thanks to its flexibility and simplicity as shown in Figure 1.4 [31-33].

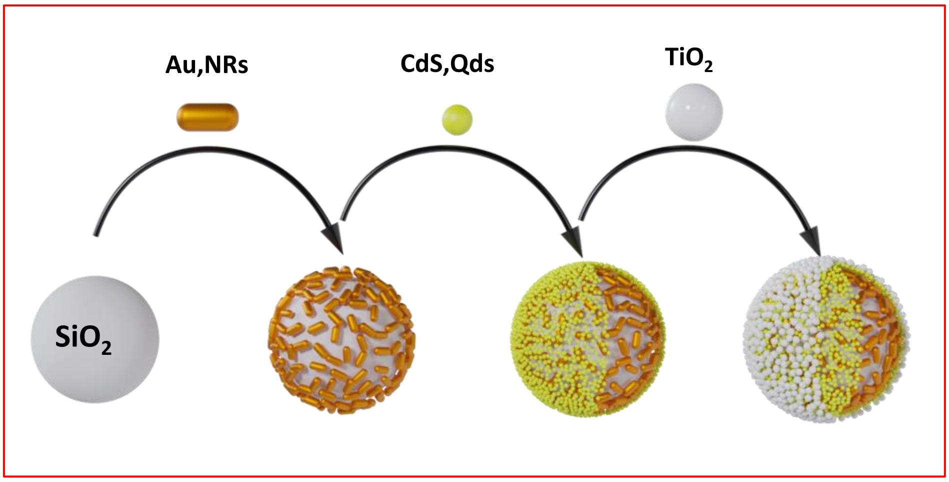

Fig. 1.4: Schematic illustration of the LBL assembly technique using PAH/PSS polyelectrolytes

The electrostatic interaction relies on covalent, hydrogen bonding, and hydrophobic interactions that can secure multilayer constructions with novel photocatalytic properties [34-40]. The LBL technique allows the incorporation of a wide range of functionalities oxides, which allows the synthesis of noble materials for potential applications such as photocatalytic materials in water splitting, solar cell, and optoelectronic [34, 39, 41-43]. Recently, the LBL attracted the attention of many researchers because of their precise structure and function [44-46]. Yet, the surface charge of the individual components can be controlled and a variety of materials as proteins, organic dyes, polymers, and colloidal particles can be easily synthesized [47-49]. However, there are many associated problems, such as the separate preparation of inorganic nanoparticles before electrostatic adsorption, adopting a strong organic solvent to dissolve the reactive alkoxide precursors, and the troublesome optimization of the solution preparation conditions should be improved.

1.3 Metal oxides

Metal oxide nanoparticles have attracted increasing attention as catalysts, especially at the nanometer size [62, 63], in a number of applications including photocatalytic applications. Bulk oxides are stable and with well-known crystallographic structures. By changing the particle size, there is change in the structural characteristics change, at which the lattice and cell parameters changed. Moreover, there is created under atom coordination (corners or edges) or oxygen vacancies in an oxide nanoparticle. Therefore, oxide NPs could differ greatly from the bulk one in their atomic arrangements, as well as the electronic states, centered on the valence band of the corresponding bulk material. These promising characteristics could offer high catalytic activity; therefore oxide NPs could find wide applications as photo-devices, ceramic materials, and catalysts for reducing environmental pollutants, transforming hydrocarbons, and producing new materials [2].

1.3.1 Optical properties of metal oxides

Metal oxides NPs with finely tunable optical properties offer a number of advantages in photocatalysis [64-66]. They are a function of the intrinsic band gap energy and can be tailored *via* different techniques including doping, or careful engineering of the band gap [67, 68].

The control of the metal oxide optical properties can carry out through controlling the size, in which with increasing of the surface area, the active sites are increase and then the optical properties enhances. So the metal oxide with a nanorods, nanowires, nanofiber, or sheets has a great surface area and then the optical properties.

1.3.2 Electrochemical properties of metal oxides

Electrical energy plays an important role in green technologies especially in electrical vehicles (EVs). Hence, electrical energy storage has attracted researchers to study new high-performance supercapacitors (SCs), DMFCs, and batteries. SCs are energy storage devices from a traditional capacitor with attractive advantages like high cycle life and high energy density. According to charge storage, SCs can be divided into three categories including chemical reaction, electrochemical double-layer capacitor (EDLC), and hybrid SC as a combination between the pseudo capacitor and EDLC [69]. Transition metal oxides and conducting polymers can store charges via a fast redox reaction. The main challenges that face researchers are related to the transition metal oxides, conducting polymers, power density, cycle stability, and cost-effectiveness [70, 71]. Metal oxides like iron oxide, chromium oxide, cobalt oxide are promising materials showing a high-performance behavior. However, these oxides require additional enhancements in their bandgap energy to be commercially applicable. For this purpose, binary metal oxides, such as nickel cobaltite, have been widely attracted researchers due to their unique properties such as their lesser bandgap, low cost, non-toxicity, thermal, and chemical stability [71, 72]. These features enabled them to be widely applied in many fields as chemical, biosensors, photo and electrocatalysis, and anti-resistant bacteria and therapeutic agents [73-75]. Metal oxides nanoparticles show typical assorted electronic ionic conductivity which is originated to ensure high conduction, electron transfer, and dyes degradation properties [75]. In the meanwhile, the electrocatalytic behavior of MO, NPs gained scientific attention due to their tunable bandgap energies. According to the abovementioned methods, the hydrothermal technique is mainly used as a valuable, easy, and economic method for the synthesis of MO nanoparticles.

1.3.3 Titanium dioxide nanoparticles

Titanium dioxide (TiO_2) was first discovered from ilmenite in 1791. It is also known as titania. TiO_2 is an n-type semiconductor found in nature as anatase, brookite, and rutile with band gaps of 3.2 eV, 3.2 eV, and 3.0 eV, respectively and was first commercially manufactured in 1916 as a white pigment [89]. TiO_2 nanoparticles are known for their varied applications, from popular products, like sunscreens, to advanced devices, photovoltaic cells, and other sets of biomedical and environmental applications, like photocatalytic degradation of toxic materials, biosensors, water refining, and drug delivery. The importance and diversity of these applications generated tremendous interest and advances in the fabrication, characterization, and basic understanding of TiO_2 nanoparticles [90-94]. The major goal of this impartial case is to synthesis of this TiO_2 nanoparticles material with highly optical properties, which enables us to have a better understanding of this material. TiO_2 nanoparticles can be synthesized using different techniques to get different dimensions varied from 0D to 3D at which 0D is specified for the spherical nanoparticles, 1D for nanorods, nanobelts, nanowires, and nanotubes, 2D for nanosheets, and 3D for porous nanostructures [94-96]. TiO_2 photocatalytic activity was first observed in 1929 when developing pigments containing TiO_2 bleached under solar irradiation. The first scientific report on TiO_2 photocatalytic activity was first published in 1932–1934 [89, 97, 98]. It was noticed that in the presence of TiO_2 ammonia and ammonium salt are oxidized when irradiated by sun lights [98, 99]. The oxidation of organic solvents and the formation of H_2O_2 were observed under UV irradiation which produces active oxygen species on TiO_2 surfaces, causing dyes degradation [89]. The water-splitting reaction was demonstrated for the first time using TiO_2 under irradiation of a 500 Wxenon lamp at which water decomposed to O_2 on the TiO_2 electrode, H_2 was produced on the Pt electrode [100, 101]. TiO_2 nanoparticles attracted much attention compared with the bulk materials as they provide a higher surface volume ratio and higher surface area. On the one hand, the latter factor improves greatly the light absorption rate, photocarrier density, photoreduction rate, leading to a surface with higher photoactivity. On the other hand, the higher surface volume ratio of the nanoparticles improves the surface absorption of OH and H_2O, increasing the photocatalytic reaction rate. When TiO_2 nanoparticles were irradiated with UV light, a series of electrochemical reactions start to emerge as a result in a generation of electrons and holes (e^- and h^+). In aqueous solutions, these created e^- and h^+ are very active sites with reducing and oxidizing capacity. These active sites are able to react with surface electrons, water, and oxygen molecules with the formation of reactive oxygen species (ROS) that may be utilized for pollutant photodegradation [102, 103]. TiO_2 nanoparticles are widely applied in many photocatalytic reactions such as self-cleaning [104], antibacterial [104, 105], in photovoltaics [106] water splitting reactions [107, 108], pollutants purification [106, 109], and photosynthesis [106]. Using the plasmonic is an effective way to improve the solar cells and photocatalysts' performance. Visible light irradiation of nanonoble metals such coupled with semiconductors, show collective oscillation of the plasmon conduction electrons onto the semiconductors affecting the electromagnetic energy distribution, which significantly changes the photocatalytic activity and semiconductor response in the visible region. This enables a potential path to fabricate new semiconductors capable of achieving new missions[110, 111]. Recent articles show that metal oxide semiconductors' physicochemical properties may depend on defects and extrinsic impurities as oxygen vacancy, which is introduced into wide bandgap semiconductors to expand optical absorption range and enhance the reactivity [112, 113]. The ability of plasmonic nanoparticles to use visible and NIR light is a strong motivation point to photosensitize the semiconductor, increasing its photocatalytic activity to a wider electromagnetic spectrum. Enhanced light-harvesting can be achieved for those energies higher than the Eg of the semiconductor (i.e when the photon energy is equivalent or more than the semiconductor bandgap). Hence, plasmonic nanoparticles increase the total transport of photons within the semiconductor, working as an antenna that concentrates the light allowing the excited electron-hole pairs formation [114]. In the hot electron injection strategy, the LSPR created over the metal nanoparticles produces a flow of excited electrons that enter the incoming field resonance. This flow of excited electrons is composed of low energies close charges near the metal Fermi level, and a small flow of highly energetic charges which are well known as hot electrons. The accumulated electrons at the CB of the semiconductor and the holes at the Fermi level of the metal can be utilized for photocatalytic applications [115]. To achieve an efficient injection between the metal and semiconductor, many factors should be considered as a correct band alignment between the CB of the semiconductor, the Fermi level of the metal, and the formation of a physical interface (e.g. Schottky barrier) between both components [116].

1.3.4 Nickel cobaltite nanoparticles

Nickel cobaltite ($NiCo_2O_4$) is considered one of the most promising materials in the cobaltite family with a spinel structure AB_2O_4 (A=Ni and B=Co) [50-52]. The higher redox chemistry of the binary system over the single metal oxides comes from the synergistic effect of the two metals which arises from the co-existence of both the Ni and Co species as illustrated in Figure 1.5 [53]. Other advantages include their higher conductivity, catalytic behavior, low cost, stability, low electrically resistance, and environmentally friendly nature. These features enabled them to be widely applied as electrocatalysts, magnetic materials, optical limiters, chemical sensors, and lithium-ion batteries [50]. Hence, the fabrication of nano-structured $NiCo_2O_4$ has recently attracted much attention. Mesoporous materials have been synthesized by the microwave-assisted method showing promise for further applications [54].

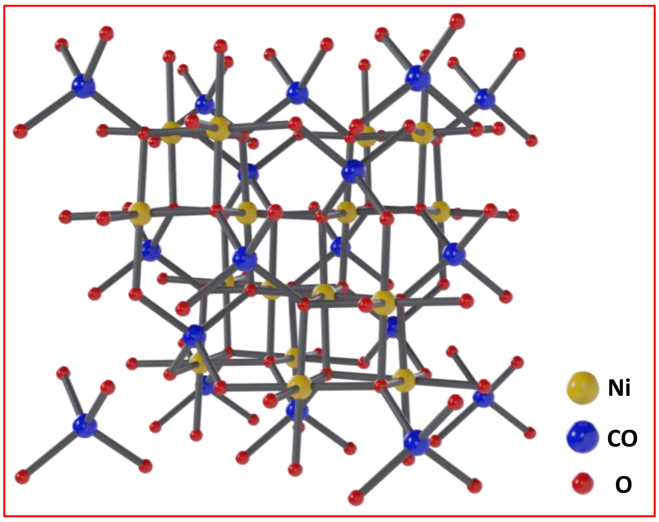

Fig. 1.5: Crystal structures of $NiCo_2O_4$unit cell.

$NiCo_2O_4$ can be synthesized in various morphologies via different methods such as spray pyrolysis, co-precipitation hydroxide decomposition route, pulsed laser, combustion, and reverse micellar pathway (Figure 1.6).

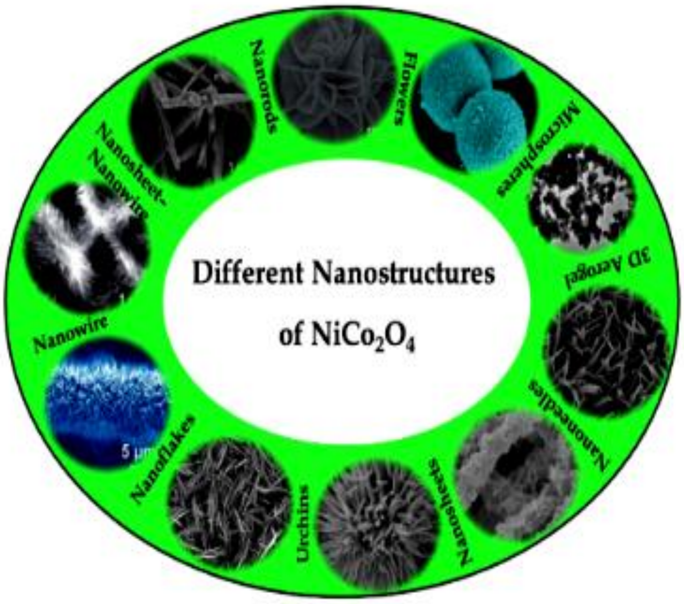

Fig. 1.6: Different nanostructures of $NiCo_2O_4$ to fabricate high-performance catalysts [55].

Other methods used alternative growth control such as polyvinyl chloride to obtain uniformity in morphology [52, 56, 57]. Simple techniques have been used to prepare highly modified nanorods catalysts to detect glucose levels [58, 59]. Among all these methods, traditional and facile chemistry methods have been widely used to synthesize nanosized materials with controlled morphology. In particular, the hydrothermal treatment technology is facile technique, without the use of any mold. Until now, various $NiCo_2O_4$ nanostructures have been extensively synthesized with markedly improved properties. Recently, $NiCo_2O_4$ nano-structure materials based on the hollow, mesoporous, nanowire, and nano-flower morphologies have demonstrated improved electrochemical properties [60, 61].

1.4 Applications of metal oxides nanoparticles

Metal oxide-based nanoparticles find wide applications in sensors, microelectronic circuits fabrication, fuel cells, coatings, and catalysis among other as illustrated in Figure 1.7. For example, metal oxide-based catalysts are applied to control the gaseous emissions that come from the combustion of fossil fuels such as CO, NO_x, or SO_x [76] or in the semiconductor industry as a component of the computer chips for instance [77].

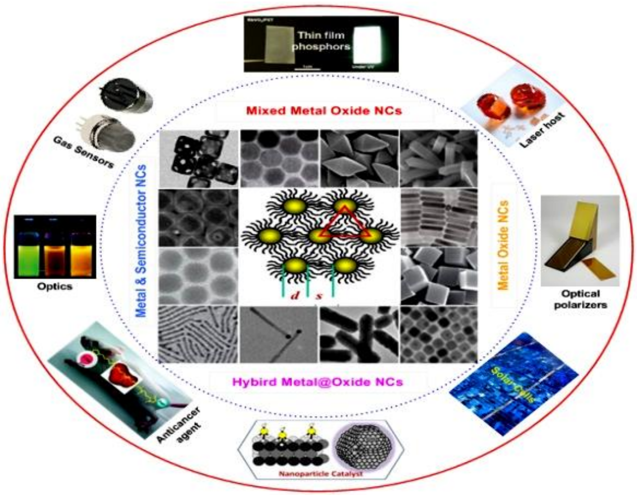

Fig. 1.7: Schematic diagram illustrating some applications of metal oxides [78].

Metal oxide applications are frequently related to their sizes. For example, the materials used for supercapacitors depend on the large surface area per weight or per the thickness of the film for their function. This geometrical consideration is not related to the unique size-dependent on physical properties. Furthermore, attempts to apply ZnO nanoparticles in tunable light-emitting devices depend on the size [79-81]. It is expected that both surface active sites and energy are expected to be based on the size of the particle, and thus, the catalytic activity can be enhanced due to the change of the surface properties with the size. Controlled nanoparticle synthesis which produces with small size distribution, has many advantages including better control of the deposition thickness and film properties. Likewise, better control of nanoparticle synthesis for a variety of materials would be expected to result in better electrochromic or smart windows, transparent conductive oxides, etc. It has been found that the efficiency of these solar cells is greatly improved if the TiO_2 nanoparticles are synthesized in a controlled manner

[82-84]. Many attempts have been conducted to synthesize low-cost single metal oxides as electrodes in a methanol oxidation reaction. However, binary oxides such as metal cobaltite allow high redox reactions using the dual action of both cobalt and metal ions.

The electrocatalytic oxidation of alcohol plays an interesting role in fuel cell reactions. Direct methanol fuel (DMFCs) attracted much attention due to their friendly impact on electronic and portable equipment. DMFCs can be classified into alkaline or acidic according to the type of electrolyte. Alkaline DMFCs has more priority and is widely used because of its economic low cost with its less corrosive alkaline action which makes the electrodes last longer (Figure 1.8).

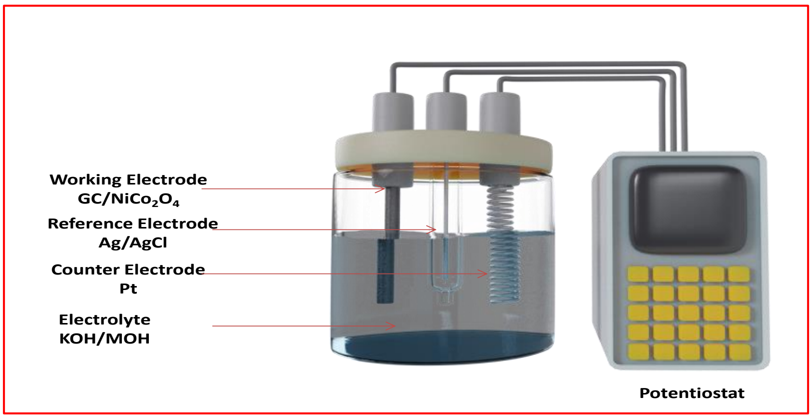

Fig. 1.8: Schematic diagram of three-electrode direct methanol fuel cells.

The rechargeable alkaline batteries as DMFCs provide high energy densities making them more favorable over most other energy systems such as hydrogen gas or nonchargeable batteries [85-87]. Methanol is widely used thanks to its availability and effective low reagent cost. It is used also as fuel in direct methanol fuel cells and as a building unit in the production of other chemical elements. While DMFCs operate at low temperatures and provide high efficiency and easy refueling properties. So, the selective oxidation would allow extraction of the largest part of the fuel energy producing a chemical product with higher commercial value than the fuel itself. However, the low current density exchange of their electrodes makes them much less energetic than the product hydrogen. A precious metal catalyst such as platinum is needed to get high reaction rates. Also, the poising effect caused by intermediates from the oxidation of organic fuels reduces platinum performance. This reduction made the researchers focus on the development of organic fuel cells.

1.4.1 photocatalytic water treatment

The man-made photocatalytic materials are similar to the plant photosynthesis. The chlorophyll of plants is a type of photocatalyst. Photocatalysis compared to photosynthesis, in which chlorophyll captures sunlight to turn water and carbon dioxide into oxygen and glucose, photocatalysis creates a strong oxidation agent to break down any organic matter to carbon dioxide and water in the presence of photocatalyst, light, and water [88]. Photocatalyst together with a light source can oxidize organic pollutants into nontoxic materials, such as CO_2, and H_2O, as well as disinfect certain bacteria. This technology is very effective at eliminating further risky organic compounds (TOCs), diversity of bacteria, and some viruses in the secondary wastewater treatment. To date, utmost research in heterogeneous photocatalysis has been focused on increasing the activity of metal-oxide photocatalysts and commonly used TiO_2. The photocatalyst's optimization can be controlled by certain factors such as, material type and particle size, then the optical properties, through controlling of the optical properties, the bandgap and hen the photocatalytic efficiency are controlled

1.5 Metal sulfides

Recently, metal sulfides, gained much interest due to their unique properties and structure. They share an important role in secondary batteries, lubricants catalysis, and semiconductors [117]. Metal sulfides demonstrate unique electrical and optical properties, allowing them to be a part of devices fabrication. Many fabrication methods can be used to synthesize metal sulfide semiconductor nanoparticles, such as microwave irradiation, electrochemical method, chemical deposition method, spray pyrolysis, thermal decomposition method, and direct element reaction at high temperature [118-123] [124].

1.5.1 CdS, QDs, and their role in enhancing photocatalytic activity

A key goal in nanomaterial research is the incorporation of multiple functionalities of different nanoscale materials inside one structure by controlling and integration spatial organization. Semiconductor QDs in the periodic table are those which have atoms from groups II-VI or III–V, with physical dimensions smaller than 20 nm [124, 125]. CdS,QDs attracted much attention in the last decades due to their excellent features like high absorption coefficients, large intrinsic dipole moments, multiple, better photostability compared to the traditional fluorescent labels, and narrower and symmetric emission spectra [126-131]. Although these are excellent features, their performance is very low and requires an improvement. The electron recombination process is considered to be one of the most serious problems behind the lower photocatalytic performance QDS at TiO_2/QDS/electrolyte. Therefore, to reduce the charge recombination effect a layer insulating the QDs was used, which acts as a passivation layer and controls the charge recombination [132].

1.6 Summary of literature review and background

This Chapter has highlighted energy production and wastewater treatment and their impact on economic and environmental aspects. Different nonmaterial fabrication technologies were represented. The characteristics physical and chemical behaviors of the bespoke nanoparticles via hydrothermal, LBL, and colloidal synthesis; signified the possible approaches for integrating nanoparticles alone or into a composite structure with superior catalytic performance.

This Chapter has highlighted energy production and wastewater treatment and their impact on economic and environmental aspects using renewable energy resources through the fabrication of advanced nanomaterials. Metal oxide-based nanoparticles applications have been handled especially those used in water treatment. Metal sulfides especially CdS,QDs, and their rule to enhance the Photocatalytic activity was also highlighted. Different nonmaterial fabrication technologies were represented with a detailed explanation of top-down and bottom-up approaches. The characteristics physical and chemical behaviors of the bespoke nanoparticles via hydrothermal, LBL, and colloidal synthesis; signified the possible approaches for integrating nanoparticles alone or into a composite structure with superior catalytic performance

Metal oxide particles were explained carefully specially the nanometer size. The effect of the size on the lattice parameters as well as the optical and the electrochemical properties was mentioned. Metal oxide-based nanoparticles applications have been handled especially those used in water treatment.

1.7 References

1. Flavelle, C., *Climate Change Could Cut World Economy by $23 Trillion in 2050, Insurance Giant Warns.* The New York Times, 2021. **22**.
2. Fierro, J., *Metal Oxides: chemistry and applications*. Vol. 108. 2006: CRC press.
3. Feynman, R.P., *There's plenty of room at the bottom.* Engineering and Science, 1960. **23**(5): p. 22-36.
4. Pritchard, D., *Literature review: explosion hazards associated with nanopowders*. 2004: Health and Safety Laboratory.
5. DAS, P., *Nano materials & their welding.* Indian Welding Journal, 2009. **42**(2): p. 1-1.
6. Thiagarajan, S.J., W. Wang, and R. Yang, *Nanocomposites as high efficiency thermoelectric materials.* Annual Review of Nano Research, 2010. **3**: p. 441-486.
7. Waseda, Y. and M. Isshiki, *Purification process and characterization of ultra high purity metals: application of basic science to metallurgical processing*. 2012: Springer Science & Business Media.

8. Elbasuney, S. and M. Yehia, *Ammonium perchlorate encapsulated with TiO 2 nanocomposite for catalyzed combustion reactions.* Journal of Inorganic and Organometallic Polymers and Materials, 2019. **29**(4): p. 1349-1357.
9. Parry, W., J. Ballantyne, and D. Jacobs, *Geochemistry of hydrothermal sericite from Roosevelt Hot Springs and the Tintic and Santa Rita porphyry copper systems.* Economic Geology, 1984. **79**(1): p. 72-86.
10. Anthony, J.L., et al., *Physicochemical Properties ofIonic Liquids.* Ionic liquids in synthesis, 2006: p. 41.
11. Akiya, N. and P.E. Savage, *Roles of water for chemical reactions in high-temperature water.* Chemical reviews, 2002. **102**(8): p. 2725-2750.
12. Kumar, S., *Hydrothermal treatment for biofuels: lignocellulosic biomass to bioethanol, biocrude, and biochar*. 2010.
13. Adschiri, T., et al., *Hydrothermal synthesis of metal oxide nanoparticles at supercritical conditions.* Journal of Nanoparticle Research, 2001. **3**(2): p. 227-235.
14. Burda, C., et al., *Chemistry and properties of nanocrystals of different shapes.* Chemical reviews, 2005. **105**(4): p. 1025-1102.
15. Cao, Y., R. Jin, and C.A. Mirkin, *DNA-modified core− shell Ag/Au nanoparticles.* Journal of the American Chemical Society, 2001. **123**(32): p. 7961-7962.
16. Daniel, M.-C. and D. Astruc, *Gold nanoparticles: assembly, supramolecular chemistry, quantum-size-related properties, and applications toward biology, catalysis, and nanotechnology.* Chemical reviews, 2004. **104**(1): p. 293-346.
17. Kim, F., et al., *Titelbild: Platonic Gold Nanocrystals (Angew. Chem. 28/2004).* Angewandte Chemie, 2004. **116**(28): p. 3699-3699.
18. Link, S., Z.L. Wang, and M. El-Sayed, *Alloy formation of gold− silver nanoparticles and the dependence of the plasmon absorption on their composition.* The Journal of Physical Chemistry B, 1999. **103**(18): p. 3529-3533.
19. !!! INVALID CITATION !!! [15-19].
20. Campion, A. and P. Kambhampati, *Surface-enhanced Raman scattering.* Chemical society reviews, 1998. **27**(4): p. 241-250.
21. McFarland, A.D., et al., *Wavelength-scanned surface-enhanced Raman excitation spectroscopy.* The Journal of Physical Chemistry B, 2005. **109**(22): p. 11279-11285.
22. Tian, Z.-Q., B. Ren, and D.-Y. Wu, *Surface-enhanced Raman scattering: from noble to transition metals and from rough surfaces to ordered nanostructures.* The Journal of Physical Chemistry B, 2002. **106**(37): p. 9463-9483.
23. Hutter, E. and J.H. Fendler, *Exploitation of localized surface plasmon resonance.* Advanced materials, 2004. **16**(19): p. 1685-1706.
24. Calander, N., *Theory and simulation of surface plasmon-coupled directional emission from fluorophores at planar structures.* Analytical Chemistry, 2004. **76**(8): p. 2168-2173.
25. Ekgasit, S., et al., *Evanescent field in surface plasmon resonance and surface plasmon field-enhanced fluorescence spectroscopies.* Analytical chemistry, 2004. **76**(8): p. 2210-2219.
26. Levi, S.A., et al., *Fluorescence of dyes adsorbed on highly organized, nanostructured gold surfaces.* Chemistry–A European Journal, 2002. **8**(16): p. 3808-3814.
27. Zhao, J., et al., *Localized surface plasmon resonance biosensors.* 2006.
28. Liang, H.-P., et al., *Gold hollow nanospheres: tunable surface plasmon resonance controlled by interior-cavity sizes.* The Journal of Physical Chemistry B, 2005. **109**(16): p. 7795-7800.
29. Mulvaney, P., *Surface plasmon spectroscopy of nanosized metal particles.* Langmuir, 1996. **12**(3): p. 788-800.

30. Noguez, C., *Surface plasmons on metal nanoparticles: the influence of shape and physical environment.* The Journal of Physical Chemistry C, 2007. **111**(10): p. 3806-3819.
31. Decher, G., *Fuzzy nanoassemblies: toward layered polymeric multicomposites.* science, 1997. **277**(5330): p. 1232-1237.
32. Tang, Z., et al., *Biomedical applications of layer-by-layer assembly: from biomimetics to tissue engineering.* Advanced materials, 2006. **18**(24): p. 3203-3224.
33. Wang, Y., A.S. Angelatos, and F. Caruso, *Template synthesis of nanostructured materials via layer-by-layer assembly.* Chemistry of Materials, 2008. **20**(3): p. 848-858.
34. Quinn, J.F., et al., *Next generation, sequentially assembled ultrathin films: beyond electrostatics.* Chemical Society Reviews, 2007. **36**(5): p. 707-718.
35. Kohli, P. and G. Blanchard, *Applying polymer chemistry to interfaces: layer-by-layer and spontaneous growth of covalently bound multilayers.* Langmuir, 2000. **16**(10): p. 4655-4661.
36. Yang, L., et al., *Hierarchical Assembly of Organic/Inorganic Building Molecules with π–π Interactions.* Advanced Functional Materials, 2008. **18**(10): p. 1526-1535.
37. Stockton, W. and M. Rubner, *Molecular-level processing of conjugated polymers. 4. Layer-by-layer manipulation of polyaniline via hydrogen-bonding interactions.* Macromolecules, 1997. **30**(9): p. 2717-2725.
38. Wang, L., et al., *A new approach for the fabrication of an alternating multilayer film of poly (4-vinylpyridine) and poly (acrylic acid) based on hydrogen bonding.* Macromolecular rapid communications, 1997. **18**(6): p. 509-514.
39. Zhang, X., H. Chen, and H. Zhang, *Layer-by-layer assembly: from conventional to unconventional methods.* Chemical Communications, 2007(14): p. 1395-1405.
40. Quinn, A., et al., *Polyelectrolyte blend multilayers: a versatile route to engineering interfaces and films.* Advanced Functional Materials, 2008. **18**(1): p. 17-26.
41. Benkirane-Jessel, N., et al., *Short-time tuning of the biological activity of functionalized polyelectrolyte multilayers.* Advanced Functional Materials, 2005. **15**(4): p. 648-654.
42. Dierich, A., et al., *Bone formation mediated by synergy-acting growth factors embedded in a polyelectrolyte multilayer film.* Advanced Materials, 2007. **19**(5): p. 693-697.
43. Schultz, P., et al., *Polyelectrolyte multilayers functionalized by a synthetic analogue of an anti-inflammatory peptide, α-MSH, for coating a tracheal prosthesis.* Biomaterials, 2005. **26**(15): p. 2621-2630.
44. Caruso, F., R.A. Caruso, and H. Möhwald, *Nanoengineering of inorganic and hybrid hollow spheres by colloidal templating.* Science, 1998. **282**(5391): p. 1111-1114.
45. Huguenin, F., et al., *Layer-by-layer hybrid films incorporating WO3, TiO2, and chitosan.* Chemistry of materials, 2005. **17**(26): p. 6739-6745.
46. Laugel, N., et al., *Nanocomposite silica/polyamine films prepared by a reactive layer-by-layer deposition.* Langmuir, 2007. **23**(7): p. 3706-3711.
47. Gentile, P., et al., *Layer-by-layer assembly for biomedical applications in the last decade.* Nanotechnology, 2015. **26**(42): p. 422001.
48. He, J.-A., et al., *Electrostatic multilayer deposition of a gold− dendrimer nanocomposite.* Chemistry of Materials, 1999. **11**(11): p. 3268-3274.
49. Marín-Caba, L., et al., *Tobacco Mosaic Virus-Functionalized Mesoporous Silica Nanoparticles, a Wool-Ball-like Nanostructure for Drug Delivery.* Langmuir, 2018. **35**(1): p. 203-211.
50. Khalil, M.M., W.M. El Rouby, and M.A. Korany, *Potentiometric sensor based on novel flowered-like Mg-Al layered double hydroxides/multiwalled carbon nanotubes*

nanocomposite for bambuterol hydrochloride determination. Materials Science and Engineering: C, 2019. **100**: p. 186-195.

51. Al-Hoshan, M., et al., *Synthesis, physicochemical and electrochemical properties of nickel ferrite spinels obtained by hydrothermal method for the oxygen evolution reaction (OER).* Int. J. Electrochem. Sci, 2012. **7**: p. 4959-4973.
52. Wang, W. and W. Ye, *Simple Hydrothermal Synthesis for Mesoporous Pebble-Like NiCo 2 O 4 Nanostructures and Their Attractive Magnetic Properties.* Journal of Superconductivity and Novel Magnetism, 2018. **31**(12): p. 3989-3994.
53. Dao, V.-D., et al., *Graphene-based RuO2 nanohybrid as a highly efficient catalyst for triiodide reduction in dye-sensitized solar cells.* Carbon, 2015. **81**: p. 710-719.
54. Karunakaran, G., et al., *Ascorbic Acid-Assisted Eco-friendly Synthesis of NiCo 2 O 4 Nanoparticles as an Anode Material for High-Performance Lithium-Ion Batteries.* Jom, 2018. **70**(8): p. 1416-1422.
55. Dubal, D.P., et al., *Nickel cobaltite as an emerging material for supercapacitors: an overview.* Nano Energy, 2015. **11**: p. 377-399.
56. Liu, S., et al., *Nickel cobaltite nanostructures for photoelectric and catalytic applications.* Small, 2015. **11**(34): p. 4267-4283.
57. Yuan, C., et al., *Facile template-free synthesis of ultralayered mesoporous nickel cobaltite nanowires towards high-performance electrochemical capacitors.* Journal of Materials Chemistry, 2012. **22**(31): p. 16084-16090.
58. Klissurski, D. and E. Uzunova, *Synthesis of nickel cobaltite spinel from coprecipitated nickel-cobalt hydroxide carbonate.* Chemistry of materials, 1991. **3**(6): p. 1060-1063.
59. Ding, R., et al., *Sodium dodecyl sulfate-assisted hydrothermal synthesis of mesoporous nickel cobaltite nanoparticles with enhanced catalytic activity for methanol electrooxidation.* Journal of Power Sources, 2014. **251**: p. 287-295.
60. Zhang, L., et al., *One-dimensional mesoporous Co 3 O 4 tubules for enhanced performance supercapacitor and enzymeless glucose sensing.* Ionics, 2019. **25**(11): p. 5445-5458.
61. Khalid, S., et al., *Microwave assisted synthesis of porous NiCo 2 O 4 microspheres: application as high performance asymmetric and symmetric supercapacitors with large areal capacitance.* Scientific reports, 2016. **6**: p. 22699.
62. Rao, C., et al., *Inorganic nanowires.* Progress in Solid State Chemistry, 2003. **31**(1-2): p. 5-147.
63. Patzke, G.R., F. Krumeich, and R. Nesper, *Oxidic nanotubes and nanorodsâ€"anisotropic modules for a future nanotechnology.* Angewandte Chemie International Edition, 2002. **41**(14): p. 2446-2461.
64. Masaaki, I., et al., *Magneto-Optical Properties of Wider Gap Semiconductors ZnMnTe and ZnMnSe Films Prepared by MBE.* Journal of Electronic Science and Technology, 2020: p. 100056.
65. Sathiyaraj, E. and S. Thirumaran, *Structural, morphological and optical properties of iron sulfide, cobalt sulfide, copper sulfide, zinc sulfide and copper-iron sulfide nanoparticles synthesized from single source precursors.* Chemical Physics Letters, 2020. **739**: p. 136972.
66. Sangeetha, G., S. Rajeshwari, and R. Venckatesh, *Green synthesis of zinc oxide nanoparticles by aloe barbadensis miller leaf extract: Structure and optical properties.* Materials Research Bulletin, 2011. **46**(12): p. 2560-2566.
67. Sadovnikov, S.I., A.V. Ishchenko, and I.A. Weinstein, *Synthesis and optical properties of nanostructured ZnS and heteronanostructures based on zinc and silver sulfides.* Journal of Alloys and Compounds, 2020: p. 154846.

68. Zhu, G., J. Wen, and L.-G. Wang, *Terahertz optical properties of surface magnetoplasmons in both prism-semiconductor-metal and prism-metal–semiconductor coupled systems.* Optics Communications, 2020: p. 126068.
69. Burke, A., *Ultracapacitors: why, how, and where is the technology.* Journal of power sources, 2000. **91**(1): p. 37-50.
70. Zheng, J., P. Cygan, and T. Jow, *Hydrous ruthenium oxide as an electrode material for electrochemical capacitors.* Journal of the Electrochemical Society, 1995. **142**(8): p. 2699.
71. Grupioni, A. and T. Lassali, *Effect of the Co3 O 4 Introduction in the Pseudocapacitive Behavior of IrO2-Based Electrode.* Journal of the Electrochemical Society, 2001. **148**(9): p. A1015.
72. Salunkhe, R.R., et al., *Chemical synthesis and electrochemical analysis of nickel cobaltite nanostructures for supercapacitor applications.* Journal of Alloys and Compounds, 2011. **509**(23): p. 6677-6682.
73. Artini, C., et al., *Yb-doped Gd2O2CO3: structure, microstructure, thermal and magnetic behaviour.* Journal of Physics and Chemistry of Solids, 2017. **103**: p. 59-66.
74. Mathew, T., et al., *Graphene-based functional nanomaterials for biomedical and bioanalysis applications.* FlatChem, 2020. **23**: p. 100184.
75. Liu, Y., et al., *Superionic conductivity of Sm3+, Pr3+, and Nd3+ triple-doped ceria through bulk and surface two-step doping approach.* ACS applied materials & interfaces, 2017. **9**(28): p. 23614-23623.
76. Delmon, B., et al., *Handbook of heterogeneous catalysis.* Ertl, G, 1997: p. 264.
77. Jolivet, J.P., M. Henry, and J. Livage, *Metal Oxide Chemistry and Synthesis: From Solution to Oxide*. 2000: John Wiley.
78. Nguyen, T.-D. and T.-O. Do, *Size-and shape-controlled synthesis of monodisperse metal oxide and mixed oxide nanocrystals.* Nanocrystal, 2011. **2**: p. 55-84.
79. Kannan, K., et al., *Nanostructured metal oxides and its hybrids for biomedical applications.* Advances in Colloid and Interface Science, 2020: p. 102178.
80. Bukkitgar, S.D., et al., *Functional nanostructured metal oxides and its hybrid electrodes–Recent advancements in electrochemical biosensing applications.* Microchemical Journal, 2020: p. 105522.
81. Gupta, N., et al., *Enhanced thermophysical properties of Metal oxide nanoparticles embedded magnesium nitrate hexahydrate based nanocomposite for thermal energy storage applications.* Journal of Energy Storage, 2020. **32**: p. 101773.
82. Wang, Y., et al., *Application of MOFs-derived mixed metal oxides in energy storage.* Journal of Electroanalytical Chemistry, 2020: p. 114576.
83. Wu, T., G. Deng, and C. Zhen, *Metal oxide mesocrystals and mesoporous single crystals: synthesis, properties and applications in solar energy conversion.* Journal of Materials Science & Technology, 2020.
84. Raizada, P., et al., *Surface defect engineering of metal oxides photocatalyst for energy application and water treatment.* Journal of Materiomics, 2020.
85. Karade, S.S., D.P. Dubal, and B.R. Sankapal, *MoS 2 ultrathin nanoflakes for high performance supercapacitors: room temperature chemical bath deposition (CBD).* RSC advances, 2016. **6**(45): p. 39159-39165.
86. Sun, S., et al., *Asymmetric supercapacitors based on a NiCo 2 O 4/three dimensional graphene composite and three dimensional graphene with high energy density.* Journal of Materials Chemistry A, 2016. **4**(47): p. 18646-18653.
87. Abouali, S., et al., *NiCo2O4/CNT nanocomposites as bi-functional electrodes for Li ion batteries and supercapacitors.* Carbon, 2016. **102**: p. 262-272.

88. Oppelt, K.T., et al., *Photocatalytic reduction of artificial and natural nucleotide co-factors with a chlorophyll-like tin-dihydroporphyrin sensitizer.* Inorganic chemistry, 2013. **52**(20): p. 11910-11922.
89. Lan, Y., Y. Lu, and Z. Ren, *Mini review on photocatalysis of titanium dioxide nanoparticles and their solar applications.* Nano energy, 2013. **2**(5): p. 1031-1045.
90. Fujishima, A. and K. Honda, *Electrochemical photolysis of water at a semiconductor electrode.* nature, 1972. **238**(5358): p. 37-38.
91. Linsebigler, A.L., G. Lu, and J.T. Yates Jr, *Photocatalysis on TiO2 surfaces: principles, mechanisms, and selected results.* Chemical reviews, 1995. **95**(3): p. 735-758.
92. Park, J.S. and W. Choi, *Enhanced remote photocatalytic oxidation on surface-fluorinated TiO2.* Langmuir, 2004. **20**(26): p. 11523-11527.
93. Thompson, T.L. and J.T. Yates, *Surface science studies of the photoactivation of TiO2 new photochemical processes.* Chemical reviews, 2006. **106**(10): p. 4428-4453.
94. Chen, X. and S.S. Mao, *Titanium dioxide nanomaterials: synthesis, properties, modifications, and applications.* Chemical reviews, 2007. **107**(7): p. 2891-2959.
95. Chen, H., C.E. Nanayakkara, and V.H. Grassian, *Titanium dioxide photocatalysis in atmospheric chemistry.* Chemical reviews, 2012. **112**(11): p. 5919-5948.
96. Zhang, Z. and J.T. Yates Jr, *Band bending in semiconductors: chemical and physical consequences at surfaces and interfaces.* Chemical reviews, 2012. **112**(10): p. 5520-5551.
97. Keidel, E., *Die Beeinflussung der Lichtechtheit von Teerfarblacken durch Titanweiss.* Farben-Zeitung, 1929. **34**: p. 1242-1243.
98. Rao, G.G., *Newer aspects of nitrification: I.* Soil Science, 1934. **38**(2): p. 143-160.
99. Boucher, D.L., et al., *An investigation of the putative photosynthesis of ammonia on iron-doped titania and other metal oxides.* Journal of Photochemistry and Photobiology A: Chemistry, 1995. **88**(1): p. 53-64.
100. O'regan, B. and M. Grätzel, *A low-cost, high-efficiency solar cell based on dye-sensitized colloidal TiO 2 films.* nature, 1991. **353**(6346): p. 737-740.
101. Fujishima, A., *Photosensitized Electrolytic Oxidation at a TiO_2 Electrode.* J. Chem. Soc. Japan, 1969. **72**(108): p. 108-113.
102. Sousa-Castillo, A., et al., *Remote Activation of Hollow Nanoreactors for Heterogeneous Photocatalysis in Biorelevant Media.* Nano Letters, 2020. **20**(10): p. 7068-7076.
103. Lawless, D., N. Serpone, and D. Meisel, *Role of hydroxyl radicals and trapped holes in photocatalysis. A pulse radiolysis study.* The Journal of Physical Chemistry, 1991. **95**(13): p. 5166-5170.
104. Hashimoto, K., H. Irie, and A. Fujishima, *Invited review papers-TiO2 photocatalysis: a historical overview and future prospects.* Japanese Journal of Applied Physics-Part 1 Regular Papers and Short Notes, 2005. **44**(12): p. 8269-8285.
105. Fujishima, F., *TiO_2 photocatalysis fundamentals and applications.* A Revolution in cleaning technology, 1999: p. 14-21.
106. Carp, O., C. Huisman, and A. Reller, *Environmental toxicity and antimicrobial efficiency of titanium dioxide nanoparticles in suspension.* Progress Solid State Chemical, 2004. **32**(1-2): p. 33-38.
107. Fujishima, A., T.N. Rao, and D.A. Tryk, *Titanium dioxide photocatalysis.* Journal of photochemistry and photobiology C: Photochemistry reviews, 2000. **1**(1): p. 1-21.
108. Ni, M. and M.K. Leung, *DYC, and K. Sumathy, A review and recent developments in photocatalytic water-splitting using TiO2 for hydrogen production.* J. renewable and sustainable energy reviews, 2007. **11**: p. 401-425.
109. Wold, A., *Photocatalytic properties of titanium dioxide (TiO2).* Chemistry of Materials, 1993. **5**(3): p. 280-283.

110. Jang, Y.H., et al., *Plasmonic solar cells: from rational design to mechanism overview.* Chemical reviews, 2016. **116**(24): p. 14982-15034.
111. Warren, S.C. and E. Thimsen, *Plasmonic solar water splitting.* Energy & Environmental Science, 2012. **5**(1): p. 5133-5146.
112. Wang, S., et al., *Titanium-defected undoped anatase TiO2 with p-type conductivity, room-temperature ferromagnetism, and remarkable photocatalytic performance.* Journal of the American Chemical Society, 2015. **137**(8): p. 2975-2983.
113. Dhumal, S.Y., et al., *Synthesis of visible light-active nanostructured TiOx (x< 2) photocatalysts in a flame aerosol reactor.* Applied Catalysis B: Environmental, 2009. **86**(3-4): p. 145-151.
114. Zhang, P., T. Wang, and J. Gong, *Mechanistic understanding of the plasmonic enhancement for solar water splitting.* Advanced Materials, 2015. **27**(36): p. 5328-5342.
115. Yu, Y., et al., *Quantifying wavelength-dependent plasmonic hot carrier energy distributions at metal/semiconductor interfaces.* ACS nano, 2019. **13**(3): p. 3629-3637.
116. Sousa-Castillo, A., et al., *Boosting hot electron-driven photocatalysis through anisotropic plasmonic nanoparticles with hot spots in Au–TiO2 nanoarchitectures.* The Journal of Physical Chemistry C, 2016. **120**(21): p. 11690-11699.
117. Chen, D., et al., *Microwave-assisted synthesis of metal sulfides in ethylene glycol.* Materials Chemistry and Physics, 2003. **82**(1): p. 206-209.
118. Kaito, C., Y. Saito, and K. Fujita, *Studies on the structure and morphology of ultrafine particles of metallic sulfides.* Journal of crystal growth, 1989. **94**(4): p. 967-977.
119. Henshaw, G., I. Parkin, and G. Shaw, *Convenient, low-energy synthesis of metal sulfides and selenides; PbE, Ag2E, ZnE, CdE (E= S, Se).* Chemical Communications, 1996(10): p. 1095-1096.
120. Skrabalak, S.E. and K.S. Suslick, *Porous MoS2 synthesized by ultrasonic spray pyrolysis.* Journal of the American Chemical Society, 2005. **127**(28): p. 9990-9991.
121. Routkevitch, D., et al., *Electrochemical fabrication of CdS nanowire arrays in porous anodic aluminum oxide templates.* The Journal of Physical Chemistry, 1996. **100**(33): p. 14037-14047.
122. from Solution, F., *Chemical deposition of chalcogenide thin films from solution.* Advances in electrochemical science and engineering, 2008. **12**: p. 165.
123. Venturelli, A., *Mobile metal-metal bonds in platinum metal sulfide clusters*. 1996: University of Illinois at Urbana-Champaign.
124. Trindade, T., P. O'Brien, and N.L. Pickett, *Nanocrystalline semiconductors: synthesis, properties, and perspectives.* Chemistry of Materials, 2001. **13**(11): p. 3843-3858.
125. Qu, L. and X. Peng, *Control of photoluminescence properties of CdSe nanocrystals in growth.* Journal of the American Chemical Society, 2002. **124**(9): p. 2049-2055.
126. Tsay, J.M., et al., *Hybrid approach to the synthesis of highly luminescent CdTe/ZnS and CdHgTe/ZnS nanocrystals.* Journal of the American Chemical Society, 2004. **126**(7): p. 1926-1927.
127. Li, L.-s., et al., *Band gap variation of size-and shape-controlled colloidal CdSe quantum rods.* Nano Letters, 2001. **1**(7): p. 349-351.
128. Zhao, D., et al., *Quantum dot− ruthenium complex dyads: recognition of double-strand DNA through dual-color fluorescence detection.* Analytical Chemistry, 2009. **81**(9): p. 3537-3543.
129. Xu, Y., et al., *A hydrogen peroxide biosensor based on the direct electrochemistry of hemoglobin modified with quantum dots.* JBIC Journal of Biological Inorganic Chemistry, 2007. **12**(3): p. 421-427.

130. Yu, W.W., et al., *Experimental determination of the extinction coefficient of CdTe, CdSe, and CdS nanocrystals.* Chemistry of Materials, 2003. **15**(14): p. 2854-2860.
131. Kamat, P.V., *Quantum dot solar cells. The next big thing in photovoltaics.* The journal of physical chemistry letters, 2013. **4**(6): p. 908-918.
132. Tachan, Z., et al., *The importance of the TiO 2/quantum dots interface in the recombination processes of quantum dot sensitized solar cells.* Physical Chemistry Chemical Physics, 2013. **15**(11): p. 3841-3845.

Chapter 2

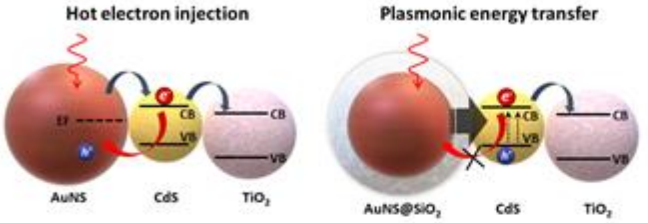
Hot electron injection
EF
e^-
CB
VB
h^+
CB
VB
AuNS
CdS
TiO_2
Plasmonic energy transfer
e^-
CB
VB
h^+
CB
VB
AuNS@SiO_2
CdS
TiO_2

Bolstering hot electron-dependent photocatalysis using dual action Effect of plasmonic and cadmium sulfide quantum dots nanoparticles for preparing SiO_2@Au-SiO_2@CdS,Qds@TiO_2 novel catalyst.

Photocatalysis presents a highly promising alternative to photovoltaics for harnessing solar energy, as it allows for storing energy in chemical products through a single-step process. However, a major obstacle to its widespread adoption is its low conversion efficiency, driving research across various fields to achieve a breakthrough in this technology. Using plasmonic materials to photosensitize traditional semiconductor photocatalysts is a popular strategy with untapped potential. In this work, we use CdS quantum dots as a bridge system, harvesting energy from Au nanostructures and transferring it to TiO_2 nanoparticles, which serve as catalytic centers. The quantum dots facilitate this process either by acting as an intermediate in a charge-transfer cascade initiated by the plasmonic system or by generating electron-hole pairs at an improved rate due to their interaction with the enhanced near field created by the plasmonic nanoparticles. Our results demonstrate a significant acceleration in the reaction when combining these elements in hybrid colloidal photocatalysts that enhance the near-field effect. We illustrate how to engineer complexes that exploit this approach and explore the complex interplay between the various mechanisms involved in the photocatalytic process. Additionally, we highlight the importance of the morphology of Au nanoparticles in their photosensitizing capabilities.

2.1 Introduction

TiO_2 has been a groundbreaking material because of its exceptional physical and chemical properties. These properties include excellent chemical stability, low toxicity, cost-effectiveness, strong supportability on various substrates, and high photocatalytic activity under ultraviolet (UV) light.[1] As a semiconductor, TiO_2 absorbs photons with enough energy to promote an electron from its valence band (VB) to its conduction band (CB), generating an electron-hole pair. These charged species can lead to the formation of reactive species in solution, which participate in oxidation or reduction reactions.[2] Due to the good alignment of its VB and CB with the redox potential of key reactions, there have been many different implementations of TiO_2 nanoparticles as a photo-active component in applications such as air and water purification, hydrogen evolution, sterilization or the formation of self-cleaning devices and anti-fogging surfaces.[1,3–6] Nevertheless, the main disadvantage for the use of TiO_2 as a photocatalyst is related with its large band gap (3.2 eV for anatase), leading to excitations restricted to the UV segment of the solar spectrum, and thus rendering a relatively inefficient material to exploit solar radiation.[7]

The potential of this wide band gap semiconductor for photocatalysis has led to the pursuit of different strategies to overcome its limitations in terms of external quantum efficiency, including morphological modifications (increasing surface area or porosity) and chemical transformations (nitrogen doping and co-doping with other elements, surface complexation and sensitization by inorganic complexes or organic dyes), aiming at tailoring the band gap of TiO_2.[8–11] The ability of plasmonic nanoparticles (PNPs) to harvest visible and NIR light can be used to extend the spectral range usable by a nearby semiconductor, increasing its photocatalytic activity of the hybrid under sunlight or other broad-spectrum illumination. In this framework, departing from traditional thermal catalysis, the plasmonic activation of TiO_2 can be explained through two different mechanisms: hot electron injection (HEI) and near-field effects allowing plasmonic energy transfer (PET). Each of them has its own advantages and drawbacks, but a detailed knowledge of how to balance and exploit them optimally is still arising.[12–16] Photoheating can in principle also contribute to the reaction,[17,18] but does not in our experimental conditions: we clamped the temperature of the sample to a homogeneously low value with a thermal bath and magnetic stirring,[19] and we worked with light intensities that can only lead to a minuscule local temperature rise.[20–22] Of course, exploiting the HEI and

PET mechanisms offered by plasmonic nanostructures is of use beyond photosensitizing semiconductors, e.g. driving photocatalysis directly,[23,24] controlling photogrowth of NPs with special shapes,[25–27] allowing chiral plasmonic photochemistry,[28,29] or SERS applications.[30,31]

In the case of HEI, after the absorption of light, the localized surface plasmon resonance (LSPR) created on a metal NP produces a population of excited electrons that oscillate in resonance with the incoming field. A small population of these electrons have higher kinetic energies and can be characterized as "hot electrons". That high energy allows them to leave the metal and be transferred to a nearby semiconductor.[32] The overall capability of a PNP to induce HEI depends on several factors, including the size, shape, and composition of the metal NP, as well as the type of interface connecting metal and semiconductor.[11,33,34] However, even in scenarios conducing to an efficient HEI across the interface, this effect is partially balanced by the back-transfer of injected carriers to the metal, where their kinetic energies are rapidly shared with the other electrons in the Fermi sea. This deleterious effect is understood to be reduced when creating a Schottky barrier between metal and semiconductor, blocking electrons at the CB edge to return to the metal. Importantly, the balance between these two effects depends on the concentration of PNP and previous reports have shown that quantities exceeding a certain metal concentration threshold induce a decrease in the net photocatalytic efficiency.[11,14,35,36]

The PET mechanism can be understood as arising from a light concentration effect at the semiconductor through the enhanced electric near-field induced by the PNP, [37–39] or trough models such as plasmon-induced resonance energy transfer (PIRET), a non-radiative dipole-dipole energy transfer between the metal and the semiconductor.[12,13,40] In either case, PET only occurs when there is spectral overlap between the plasmonic modes of the PNP and the absorption band of the semiconductor. In contrast to hot electron injection, PET processes do not involve charge transfer between the metal and other elements, and can occur in geometries where the plasmonic sensitizer and the semiconductor are separated by an insulating material.[13,35]

Another approach capable of enhancing the photocatalytic properties of TiO_2 is the combination of TiO_2 with other semiconductors with narrower band gaps that enables absorption of lower-energy photons in the visible region.[41–44] Moreover, if the CB of the second semiconductor lies at higher energies than that of TiO_2, this is beneficial to enhance the charge separation. In this work we have used CdS quantum dots (CdS-QDs) to accrue these advantages. Besides being cheap and easy to synthesize, the absorption of CdS partially overlaps with the plasmonic resonance of small Au NPs, which makes it an interesting candidate for creating plasmonic-semiconductor hybrids,[39,45] both in colloidal suspension [37] and creating planar metamaterials [46]. While the photo-generated electrons in the CdS CB are transferred to the TiO_2, the photo-generated holes remain in the CdS VB. In this manner, the charge recombination probability is also reduced as a result of the separation effect, to the benefit of the energy conversion efficiency and overall photocatalytic activity.[47,48] The addition of PNP to the TiO_2/QDs assemblies can further enhance the overall photocatalytic performance of the composites by increasing the charge carriers transferred.[49–52] One can also consider the QDs as a "bridge" between the PNP and the TiO_2 NPs, both in terms of HEI and, perhaps more importantly, PET due to the more significant overlap between the PNP and QD spectra. This situation contrasts with that of a metallic catalyst in interaction with the PNP, in which PET is possible at broader wavelength ranges.[53–55]

Herein, we present a layer-by-layer (L-B-L) synthesis strategy for the hierarchical assembly of Au PNP or core-shell Au@SiO_2 PNP with CdS-QDs and TiO_2 NPs onto submicrometric silica beads (SiO_2). The SiO_2 shell over the PNP will block charge transfer events to and from the metal NPs. These hybrid photocatalysts will serve as a test bench for exploring the outcomes of making either HEI or PET the dominant energy transfer mechanism and evaluate what design decision lead to greater efficiencies. On this line, we will also explore the effect of the L-B-L deposition order over the final photocatalytic effects, supporting our description of the hybrid photocatalysts' operation and offering additional insights in the engineering of successful photocatalytic complexes.

2.2 Methodology

2.2.1 Synthesis of nanomaterials

2.2.1.1 Chemicals

Sodium sulfide 99% (NaS_2), cadmium nitrate 99% ($Cd(NO_3)_2$), l-cysteine 99%, sodium hydroxide 98% (NaOH), sodium borohydride ($NaBH_4$), cetyltrimethylammonium bromide 96% (CTAB), silver nitrate ($AgNO_3$), hydrochloric acid 37% (HCl), tetrachloroauric acid ($HAuCl_4 \cdot 3H_2O$), L-ascorbic acid 99% (AA), poly(allylamine hydrochloride) MW 17500 (PAH), tetraethylorthosilicate 98% (TEOS), ammonium hydroxide solution 28–30% (NH_4OH), sodium citrate ($Na_3C_6H_5O_7$), sodium chloride (NaCl), Rhodamine B (RB), formic acid 99% (FA) and poly(styrenesulfonate) MW 70000 (PSS), were purchased from Sigma-Aldrich. TiO_2 nanoparticles 5 nm (anatase ≥99%) were purchased from Nanoamor. Milli-Q water and absolute ethanol were used in all preparations.

2.2.1.2 Synthesis and PAH functionalization of silica beads

Monodisperse silica spheres with a diameter of 520 nm were synthesized using a modified Stöber method.[68] Typically, a solution of TEOS (1.7 mL, 1.2 M) was added to a solution containing ethanol (18.12 mL), ammonium hydroxide (1.96 mL), and water (3.21 mL). This mixture was stirred at room temperature for 2 h. The excess of reagents was removed by three centrifugation-redispersion cycles with ethanol (5000 rpm, 15 min). Subsequently, PAH was dissolved in a 0.5 M NaCl aqueous solution with a final polymer concentration of 1 mg/mL. Then, 30 mL of the positively charged PAH solution were added to 30 mg of silica nanoparticles and stirred at room temperature for 30 min. The excess of reagents was removed by three centrifugation-redispersion cycles with water (5000 rpm, 15 min).

2.2.1.3 Synthesis of Gold Nanospheres (AuNS)

50 ml of a stable dispersion of spherical negatively charged citrate-stabilized gold nanoparticles (AuNS) was prepared by the method described elsewhere.[69] The final diameter was fixed at 23 ± 2 nm after two growth steps.

2.2.1.4 Synthesis and PSS functionalization of Gold Nanorods (AuNR)

50 ml of AuNR with LSPR centered at 856 nm were synthesized by the seed-mediated growth method, as described elsewhere.[70] The dimensions obtained from the TEM images analysis were 54 ± 4 nm of length and 13 ± 1 nm of thickness. 25 ml of the final CTAB-stabilized AuNR solution were subsequently coated with a layer of a negatively charged polyelectrolyte (PSS) in order to facilitate the deposition onto the positively charged PAH functionalized silica beads.[71]

2.2.1.5 Silica coating of AuNS and AuNR

25 ml of the citrate-stabilized AuNS and 25 ml of the CTAB-stabilized AuNR were coated with a thin layer of silica by following a previously published procedure.[72] The silica thickness was 8 ± 1 nm for AuNS@SiO_2 and AuNR@SiO_2 (Figure 3.2).

2.2.1.6 Deposition of AuNS, AuNS@SiO_2, AuNR@PSS and AuNR@SiO_2 onto PAH-functionalized silica beads

0.5 ml of each solution of PNP (C_{Au} = 0.5 mM) was added to 5 ml of PAH-functionalized silica beads (1 mg/ml). The mixture was stirred at room temperature for 3 h and washed by three centrifugation-redispersion cycles (5000 rpm, 20 min). The product was redispersed in 5 mL of water and functionalized with another layer of PAH in order to deposit the cadmium sulfide quantum dots.

2.2.1.7 Synthesis of cadmium sulfide quantum dots (CdS-QDs) and deposition onto SiO_2-PNP assemblies

CdS-QDs were prepared using a modification of the protocol reported by Bae et al.[73] Under a N_2 atmosphere, 1 mmol of L-cysteine and 0.5 mmol of cadmium nitrate, were placed in a flask and dissolved in 100 ml of Milli-Q water with the pH value adjusted at 7.0 by using a prober buffer solution. The mixture was kept under stirring at 47 ^{o}C. Then, a sodium sulfide solution (0.51 mmol) was added dropwise under continuous stirring and let it to react for 2 h. The CdS-QDs formation was confirmed by UV-vis (Figure 3.1d) and the solution was kept in the dark.

1 ml of the synthesized CdS-QDs (0.72 mg/ml) was added to 5 mL of each solution of the PAH functionalized SiO_2-PNP assemblies and stirred at room temperature for 3 h. The excess of QDs was removed by three centrifugation−redispersion cycles (5000 rpm, 20 min) and the SiO_2-PNP-QDs assemblies were functionalized with another layer of PAH.

2.2.1.8 TiO_2 deposition

50 mg of TiO_2 (anatase, 5 nm nanoparticles) redispersed in 100 mL of a sodium citrate solution (2.5 mM) was sonicated for 1 h with an ultrasonic tip. The aggregates of TiO_2 NPs were removed by centrifugation (3500 rpm, 10 min). Then, 5 mL of each PAH functionalized SiO_2-PNP-QDs assemblies was added to 4 mL of the TiO_2 solution and stirred for 3 h. The excess of TiO_2 was removed by three centrifugations−redispersion cycles (5000 rpm, 20 min) and the final catalyst was protected from the light until the photocatalytic experiments. The final molar PNP/TiO_2/CdS ratios for all the samples were determined by inductively coupled plasma mass spectrometry (ICP-OES, Table 1).

2.2.2 Optical Characterization and chemical, Structural.

TEM images were obtained using a JEOL JEM 1010 transmission electron microscope operating at an acceleration voltage of 100 kV. UV-visible-NIR absorbance spectra were recorded on a

Cary 8454 UV-visible-NIR spectrophotometer fitted with a thermostated holder and collected from a 1-cm path length quartz cuvette. Quantitative element detection from liquid samples was obtained using a Perkin Elmer Optima 4300 ICP-OES spectrometer with the samples previously digested in hydrofluoric acid.

2.2.3 Photocatalytic Study

Rhodamine B photocatalytic degradation: The photocatalytic activity of the SiO_2@PNP@TiO_2 nanohybrids was assessed by measuring the degradation of Rhodamine B (RhB) in a magnetically stirred sample at 25 °C, under light irradiation from a LOT solar simulator (300 W Xe lamp, wavelength excitation from 350 to 2400 nm). The study is carried out in a 20 mL aqueous solution with a concentration of RhB of 0.01 mM and 4 mg of hybrid photocatalyst. The mixtures were stirred for 1 hour in the dark to blend well and allow the adsorption-desorption equilibrium to take place before irradiation. Aliquots of 2.5 mL were taken within 30 min intervals during the experiments in order to measure the variation in the absorbance of the dye. The photocatalytic activity of the hybrids is measured in terms of photodegradation of RhB over irradiation time. *Photocatalytic dehydrogenation of formic acid:* Photocatalytic hydrogen generation assisted by formic acid has been followed using the nanohybrids as photocatalysts. Typically, 5 mL of an aqueous dispersion of the catalyst (0.8 mg/ml) was mixed with 200 µL of formic acid in a 13 mL reactor. The gases were purged with Ar for 2 min before sealing the flask. The dispersion was magnetically stirred inside a water bath at 35°C under light irradiation with the solar simulator (λ = 350–2400 nm). After 1 h, the gases were analyzed with an Agilent 7820A gas chromatographer to measure the volume of H_2 generated.

2.3 Results and Discussion

As indicated in Figure 2.1a, the commercial TiO_2 NPs and the prepared CdS-QDs have band gaps of 3.3 eV and 2.6 eV, respectively, determined from experimental extinction spectra using

Tauc's plot. Thus, the incorporation of CdS into the hybrid catalyst with TiO_2 alone significantly enhances light absorption in the visible region.

We have synthesized four different types of Au NPs to integrate them onto the TiO_2/CdS-based hybrid nanostructures reported herein. These four systems are created in order to explore two different aspects of the PNP contribution: (i) choosing the wavelength of the main LSPR, and (ii) whether they can contribute through HEI. Firstly, and having their main LSPR in the visible spectrum, we created naked and silica-coated gold nanospheres (AuNS and AuNS@SiO_2) displaying a plasmonic signatures centered at 523 and 535 nm, respectively (red and orange spectra, Figure 2.1b) and with the original AuNS diameter fixed at 23 nm (Figure 2.1c). Secondly, and having their main LSPR in the near-IR, we created naked and silica-coated gold nanorods (AuNR and AuNR@SiO_2) with longitudinal plasmon bands centered at 856 and 871 nm, respectively (brown and purple spectra, Figure 2.1b) and with the aspect ratio of 4.15 (54 x 13 nm, Figure 2.2d). In the case of silica-coated nanoparticles the maximum absorption is shifted to higher wavelengths, with respect to the original AuNP, as a result of the refractive indices increases once that the AuNP are screened by the SiO_2 shell.[56] In both Au@SiO_2 NPs the SiO_2 shell was homogenous, and the thickness was 8 nm (Figure 2.2). In this manner, we will explore four distinct scenarios by combining two different well-differentiated plasmonic signatures with two different photosensitization mechanisms. Accordingly, the naked resonators will be in direct contact with the QDs/TiO_2 assemblies showing a dominant hot electron injection mechanism while the silica-coated resonators will show a pure plasmon energy transfer mechanism due to their isolated silica shell. Moreover, by utilizing both AuNS and AuNR, we can compare plasmonic excitation from different regions of the electromagnetic spectrum.

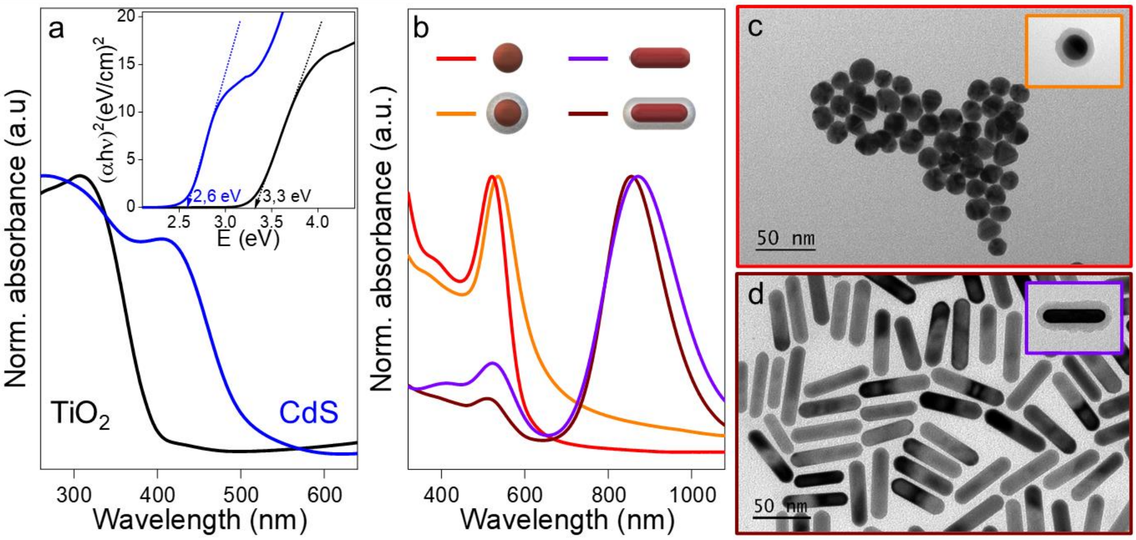

Fig. 2.1. (a) Absorbance spectra resulting from semiconductor absorption and band gap calculation (Tauc plot) of TiO_2 NP (black) and CdS-QDs (blue). (b) Normalized absorbance spectra of AuNS (red), AuNS@SiO_2 (orange), AuNR (brown) and AuNR@SiO_2 (purple). (c,d) TEM images of the AuNS and AuNR, respectively (inserted in in the upper right part, the silica-coated particles).

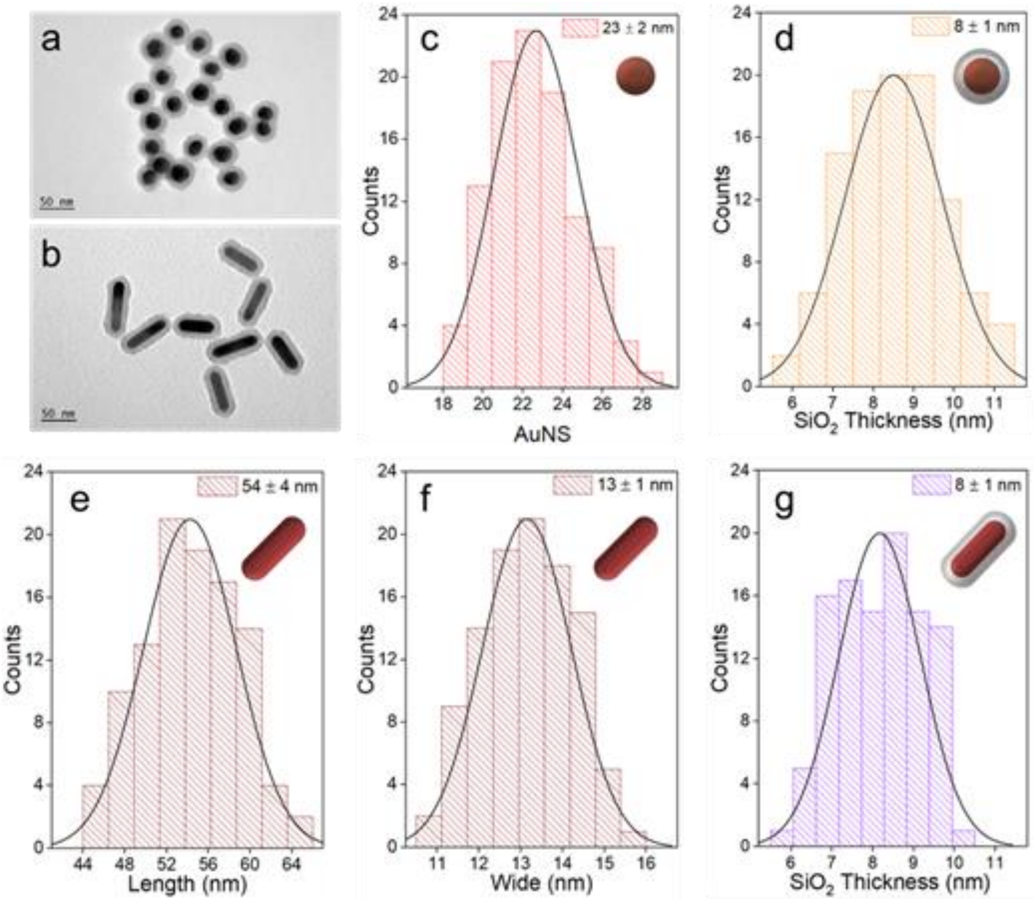

Fig. 2.2. (a,b) TEM images of the AuNS@SiO_2 and AuNR@SiO_2, respectively. (c,d) Size histograms of core and shell in the AuNS@SiO_2. (e-g) Size histograms of core and shell in the AuNR@SiO_2.

As mentioned above, the different Au nanoparticles are integrated into hybrid photocatalysts. For this purpose, silica beads with 525 nm of diameter exposed to a positively-charged solution of polyelectrolyte have been used as supports for the adsorption of the negatively charged PNP followed by the adsorption of the CdS-QDs, and, finally, another layer with 5 nm TiO_2 NPs (Figure 2.2a). This layer-by-layer protocol has been previously used for the assembly of PNP and semiconductors permitting a tight control in the composition and functionality of the final structure.[11,35,57] For comparison purpose, the PNP/CdS/TiO_2 hybrids formed present the same Au/Cd/Ti molar ratio (0.0711/0.121/1, determined by ICP-OES, **Table 2.1**).

Sample: (SiO_2 bead with)	**Ti (nmol/mg)**	**Au (nmol/mg)**	**Cd (nmol/mg)**
TiO_2	449,16	-	-
CdS/TiO_2	465,87	-	60,49
AuNS/TiO_2	460,19	30,85	-
AuNS@SiO_2/TiO_2	450,64	29,92	-
AuNR/TiO_2	451,25	33,00	-
AuNR@SiO_2/TiO_2	463,38	31,96	-
AuNS/CdS/TiO_2	457,56	35,77	51,35
AuNS@SiO_2/CdS/TiO_2	467,96	33,50	49,82
AuNR/CdS/TiO_2	453,34	33,00	59,60
AuNR@SiO_2/CdS/TiO_2	461,70	32,49	56,04

Table 2.1. Nanomoles of Ti, Au and Cd per milligram of catalyst for all the assemblies. These values were obtained by ICP-OES. The color code in the sample description follows that of the figures in the main text.

Moreover, the catalysts present high homogeneity and colloidal stability (Figures 2.3b-e). In what concerns to the optical properties (Figure 2.3f), the hybrids display a strong absorption under 500 nm as a consequence of QDs and TiO_2 absorption in the visible and UV region, respectively. Additionally, an important scattering contribution of the SiO_2 beads is perceived at lower wavelength, with a long tail covering the visible spectrum and part of the NIR. Over it, the LSPR signatures of the naked and silica-coated nanoparticles are discernible (Figure 2.3f) with a slight red shift with respect to the free particles in solution as a consequence of the larger effective refractive index created by the materials surrounding the PNP.[58,59]

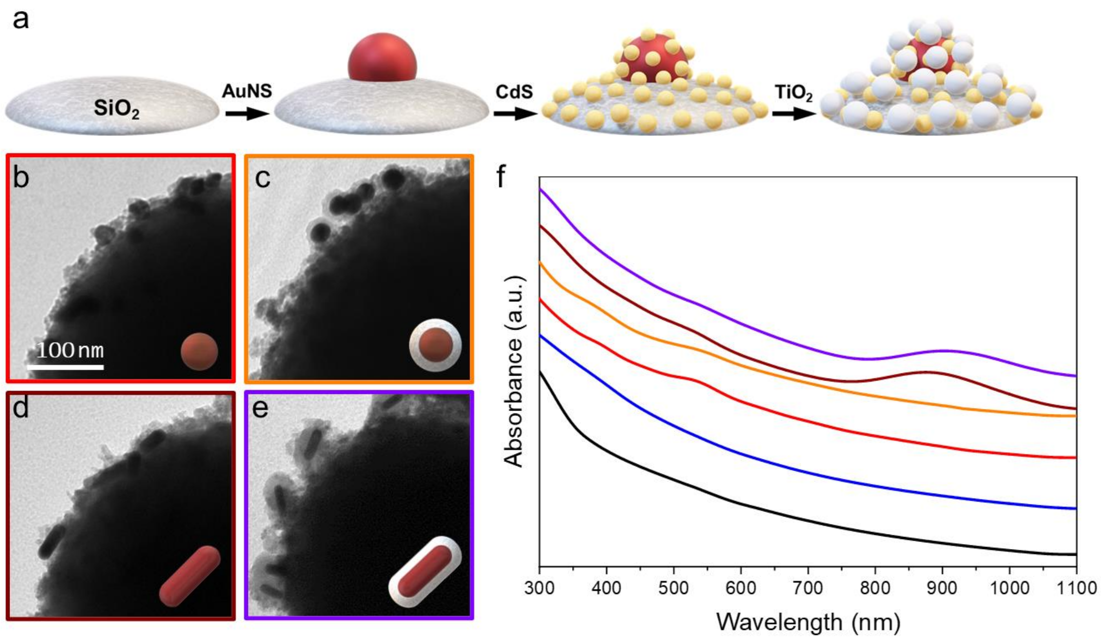

Fig. 2.3. (a) Scheme of the layer-by-layer assembly of the hybrid photocatalysts. In a first step, the chosen PNP are adsorbed onto the surface of SiO_2 beads and, subsequently, the layers of CdS-QDs and TiO_2 NP are added. (b-e) TEM images and (f) vertically-offset absorbance spectra of the hybrid photocatalysts formed with: (b) AuNS-CdS-TiO_2 (red line), (c) AuNS@SiO_2-CdS-TiO_2 (orange line), (d) AuNR-CdS-TiO_2 (brown line) and (e) AuNR@SiO_2-CdS-TiO_2 (purple line). Black and blue spectrum correspond to hybrid assemblies with TiO_2 and CdS-TiO_2, respectively.

The photocatalytic efficiency of the synthetized nanocomposites has been evaluated through the photodegradation of Rhodamine B (RhB) and formic acid dehydrogenation as model reactions. In this manner, the degradation of RhB in the presence of the hybrids was monitored by following the decrease in the absorption maximum of this dye (λ_{max} = 554 nm) as a function of time, using a solar simulator with emission ranging from 350 to 2400 nm. Firstly, the photocatalytic experiment was performed using the catalyst without the QDs layer (Figure 2.4a), providing us with a baseline of the TiO_2 photoactivity. After 3 h of reaction only a 13.90 % of degradation is observed using the SiO_2 beads functionalized with TiO_2 NPs alone (black line, Figure 2.4a) as a result of the direct photoexcitation of the semiconductor with the small fraction of UV photons. In the case where we add naked AuNS and AuNR the degradation of the dye is increased to 26.89 % and 31.91 % during the same period of time (red and brown lines, Figure 2.4a) as a result of the combined effect of HEI and PET mechanisms by the PNP. The increased efficiency for the HEI in AuNR with respect to AuNS for the same Au/Ti molar ratio is due to a more intense local fields around the tips of PNP for sharper anisotropies, as well as the presence of the main resonance at longer wavelengths (see Figure 2.5c).[11,60] Unsurprisingly, the addition of silica-coated gold nanoparticles does not induces a major influence in the final degradation with respect to the system without PNP (Orange and purple lines, Figure 2.4a), as only the PET mechanism can occur in these systems, and the spectral overlap between the plasmonic modes and the TiO_2 absorption is very small.

When the same experiment was performed using the catalysts with the QD layer and in the absence of AuNP the degradation of RhB increases from 13.90 % (black line, Figure 2.4a) to 28.8 % (blue line, Figure 2.4b). The enhanced photocatalytic activity can be attributed to a more effective response of the catalyst with QDs in the visible region.[41–44] As mentioned above, we expect this effect to increase when adding PNP as photosensitizers. With the addition of AuNS and AuNR onto the assemblies the degradation increases to a 39.48 % and 48.77 %, respectively (red and brown lines, Figure 2.4b). Interestingly, the use of catalysts with AuNS@SiO_2 and AuNR@SiO_2 leads to a 93.96 % and 56.97 % of degradation, respectively. We discuss these differences below, with the support of computational results.

We reproduced the same general trends with an additional model reaction, measuring the photocatalytic hydrogen generation assisted by the degradation of formic acid in the presence of the hybrid nanomaterials as photocatalysts (Figure 2.4c).[33,61] This experiments produces the same trend reported for the photodegradation of RhB. In this manner, the photogenerated hydrogen increases from 12.88 nmoles $g^{-1}h^{-1}$, in the case of use the assemblies without Au (Blue column, Figure 2.4c), to 17.72 nmoles $g^{-1}h^{-1}$ and 22.45 nmoles $g^{-1}h^{-1}$for naked AuNS and AuNR (Red and brown columns, Figure 2.4c), respectively. In the presence of the silica-coated AuNS@SiO_2 and AuNR@SiO_2 the photogenerated hydrogen increases to 49.86 nmoles $g^{-1}h^{-1}$ and 41.05 nmoles $g^{-1}h^{-1}$, respectively.

Finally, we investigated the influence of the assembly order on the layer-by-layer synthesis of these nanohybrids. To achieve this, we took the catalyst with the highest photocatalytic efficiency among the ones we studied, and modified the hierarchy in which the layers were assembled, to then perform the photocatalytic degradation of RhB under equal conditions. As we can see in Figure 2.3d, when we deposited the AuNS@SiO_2 nanoparticles in the middle layer between the CdS-QDs and the TiO_2 NPs the final degradation decreases form 93.96 % to 50.04 % (full and hollow orange circles, respectively). These results support the interpretation that the CdS-QDs serve as an energy pathway between PNP and TiO_2, a function that they fulfill when they are between, and in direct contact with, the PNP and the TiO_2 NPs. In other terms, depositing the QDs after the PNP greatly increases the number of CdS-QDs that are close to both PNP' surfaces and TiO_2 NPs. By first depositing the QDs, many of them will be either under the PNP and thus in no close contact with TiO_2 NPs, or near TiO_2 NPs but far from the PNP' enhanced near field.

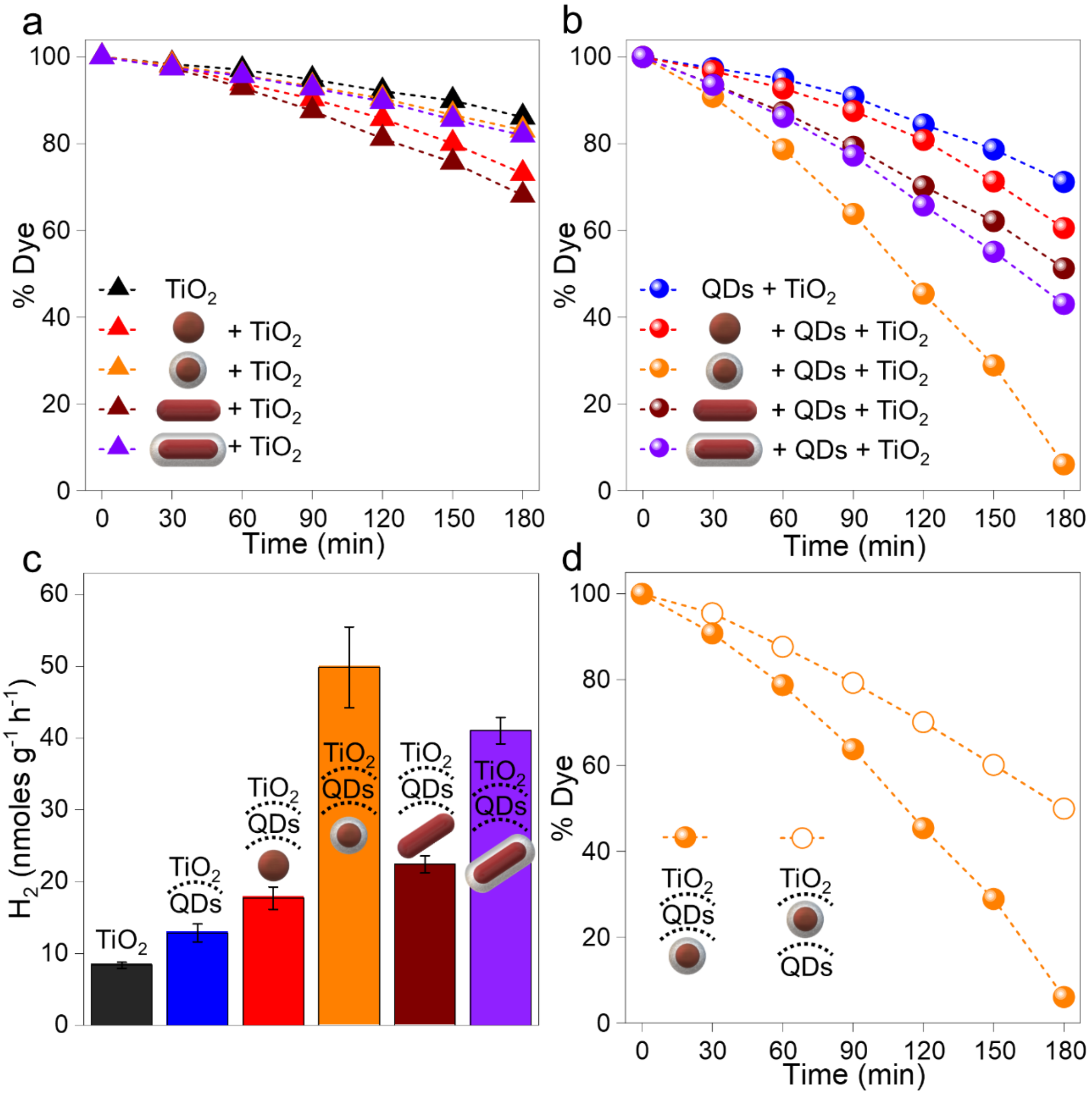

Fig. 2.4. Photocatalytic degradation of Rhb in the presence of the hybrids with TiO_2 (a) and with CDs and TiO_2 (b). (c) Photocatalytic hydrogen generation assisted by formic acid in the presence of different hybrid (nanomoles of H_2 per mg of catalyst in 1 h of reaction). (d) Photocatalytic degradation of Rhb in the presence of the catalyst composed by AuNS@SiO_2, CDs and TiO_2 by changing the order of the L-B-L assembly (AuNS@SiO_2/CDs/TiO_2, orange circles and CDs/AuNS@SiO_2/TiO_2, white circles). In all panels, the catalyst with TiO_2 alone was represented in black and catalyst with CDs and TiO_2 alone was represented in blue; catalyst with AuNS, AuNS@SiO_2, AuNR, AuNR@SiO_2 was represented in red, orange, brown and purple, respectively (triangles for control experiments without CDs and circles for hybrids with QDs and TiO_2). P = 1.0 atm, T = 25 °C and λ = 350-2400 nm.

Turning now our attention to the phenomena underlying the reaction in the different configurations, we can explain the increased photocatalytic activity of the PNP-loaded hybrids by taking in consideration the main photoactivation mechanism of each system. In the hybrids with naked AuNP (Figure 2.5a) the plasmonic excitation produces a population of “hot electrons” that can be injected from the conduction band of the Au NPs to the conduction band of CdS-QDs and, finally, transferred to the conduction band of the TiO_2 NPs. It is important to remember, however, that in this configuration the plasmonic nanoparticle also act as recombination center, reducing the overall electrons transferences.[14,35,36,62] In the case of silica-coated nanoparticles (Figure 2.5b) the electromagnetic field enhancement produced by the localized surface plasmon resonance increases the charge separation in the CdS-QDs near to the AuNS@SiO_2. This effect, which should contribute in the case of naked PNP, is now dominant because HEI, as well as charge back-transfer, is blocked by the SiO_2 layer. Now, electrons excited within the QDs can be transferred from the CB of the QDs to the CB of the TiO_2 NPs. Again, it is important to note that the silica layer prevents charge transfer from the semiconductors to the metal. To further support this interpretation of results in Figure 2.4b,c, we performed additional photocatalytic experiments using a bandpass filter that allows only light with wavelengths over 700 nm (see Figure 2.6). When using AuNRs@SiO_2 hybrid photocatalysts, the activity drops to virtually nothing, as we are not driving the transversal plasmonic mode susceptible of exciting the QDs through its enhanced near-field; whereas when using naked AuNRs we see a reduced but still significant degradation, as we lose the PET effect and the HEI of the transversal mode but retain the HEI of the main AuNR mode at longer wavelengths. Importantly, in this latter case electron back-transfer still hinders the photoreaction, limiting the otherwise large capability of the AuNRs of exciting hot electrons, as discussed below.

To extend our discussion on the role that the different photosensitization mechanism has in these hybrids, we complement the experimental results with computational simulations of AuNR and AuNS modeled using the shapes and sizes of the experimental samples. Firstly, comparing the computed extinction cross sections of the PNP (Figure 2.5c) with their experimental absorbance (Figure 2.1b), we see that the theoretical models reproduce well the optical properties of the samples. If we look at the potential contribution of the different energy transfer mechanisms (Figure 2.5a), we can distinguish different relevant aspects to discuss. In Figure 2.5d we can see the rates of excitation of intraband hot carriers at the surface of the PNPs. At this point, only the results for naked AuNS and AuNR are included because by coating the PNP with SiO_2 we avoid the transfer of hot electrons between the metal and the environment. In this plot it is apparent that the stronger longitudinal plasmonic mode of the AuNR dominates in exciting hot electrons, over both its transversal mode and the AuNS plasmon. It also underscores that allowing hot carrier injection as a photocatalytic mechanism allows the sensitization of the system to photons with lower energies, up to wavelengths in the near infrared with the AuNR studied herein. This comes at the cost, however, of allowing carrier recombination through electron back-transfer to the metal.[63] Qualitatively, this explains the modest improvement seen in figure 2.4a when using AuNR (brown triangles) over AuNS (red triangles). Although with the naked AuNP the excitation of CdS-QDs and TiO_2 through near field also occurs, to the extent that their absorption bands spectrally overlap with the plasmon resonances, it is when we consider the SiO_2-coated AuNP for isolate this contribution.

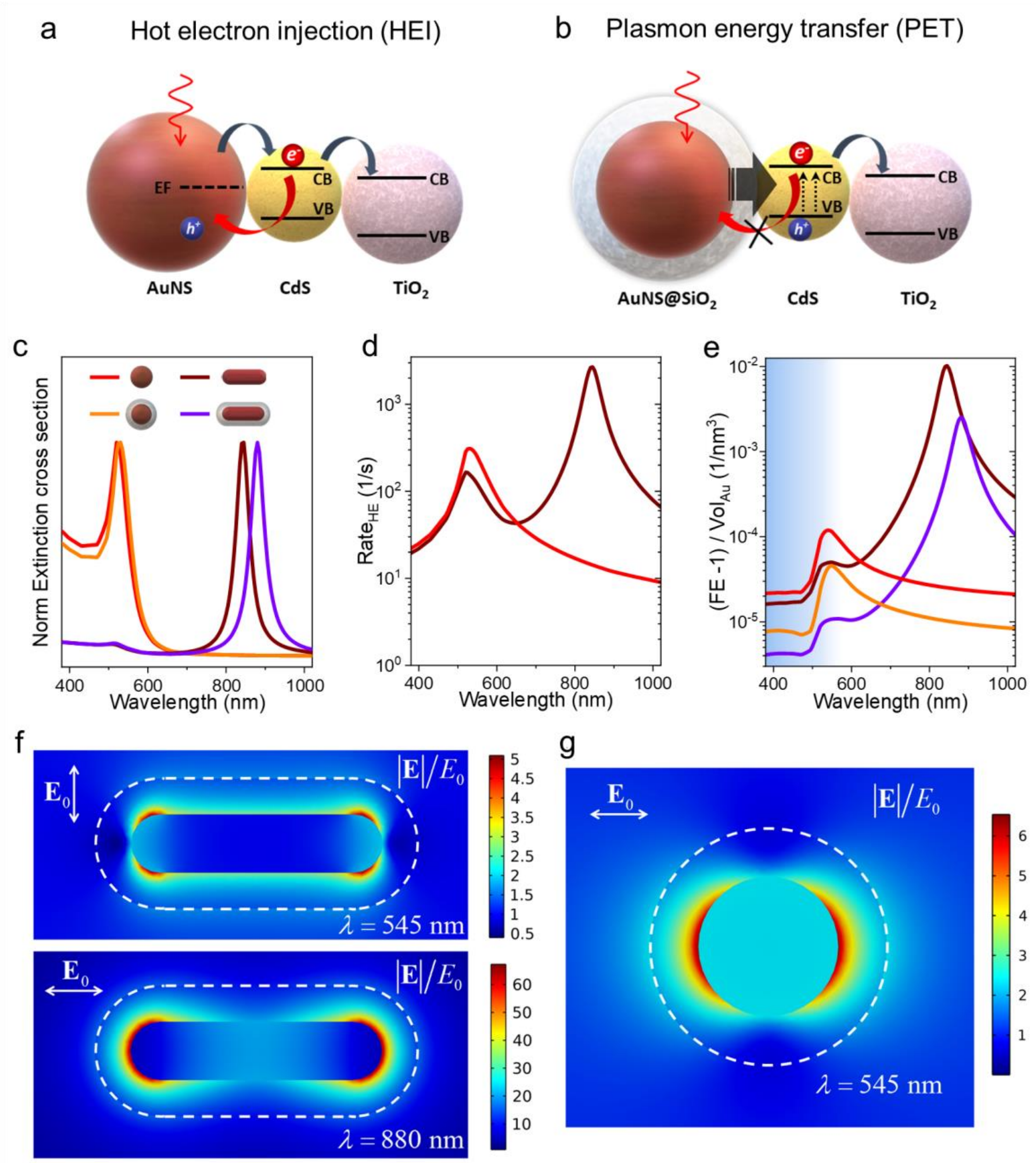

Fig. 2.5. (a) Representation of the HEI mechanism in the hybrid composed by AuNS/CdS-QDs/TiO_2 (upper panel) and PET in the hybrid composed by AuNS@SiO_2/CdS-QDs/TiO_2 (lower panel). (b) Theoretical extinction cross sections of AuNS, AuNS@SiO_2, AuNR and AuNR@SiO_2. (c) Rate of intraband hot carrier excitation for naked AuNS and AuNR. (d) Average field enhancement (eq. 1) and (e) average field enhancement, referenced to zero and normalized by the Au volume of each particle. The blue region in panels *d* and *e* indicates the spectral region with non-zero QD absorption. In all figures AuNS, AuNS@SiO_2, AuNR and AuNR@SiO_2 was represented in red, orange, brown and purple, respectively. (f,g) Electric field maps for the transversal and longitudinal modes of AuNR@SiO_2 (f) and for the plasmonic mode of AuNS@SiO_2 (g). The external boundary of the SiO_2 layer is highlighted with a dashed white line.

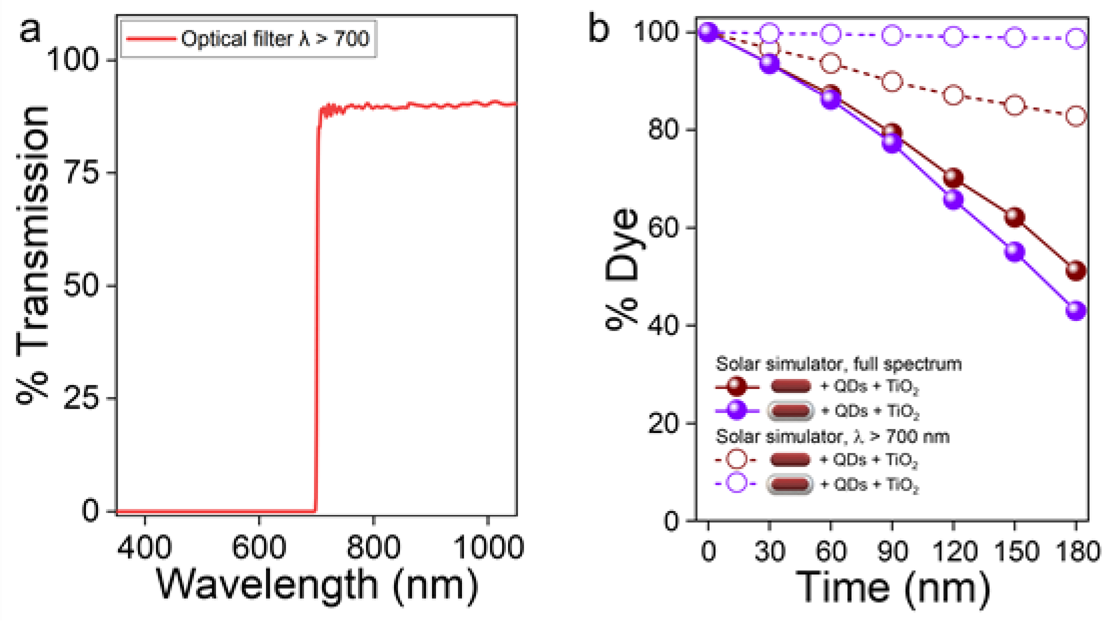

Fig. 2.6. Photocatalytic degradation of RhB using a long-wavelength-pass filter. (a) Transmission spectrum of the filter. Its profile is remarkably flat from 700 nm on, although one has to note that its transmission is only around 90%, a factor to account for in analyzing degradation results. (b) Photocatalytic degradation of RhB for hybrids containing AuNRs with and without SiO_2 layer, contrasting the evolution of the reaction under the full spectrum of the solar simulator without the visible and UV light. The results under full spectrum illumination are those from Figure 3b.

Then, considering energy transfer through near-field interaction between AuNP and environment, we present in Figure 2.5e the volume-averaged field enhancement (FE) in the space available around the AuNP or its SiO_2 coating. Here it is clear that the strongest contribution could come from the longitudinal resonances of the AuNR, but the hybrid photocatalyst cannot take the energy stored in the plasmonic near-field at these wavelengths because the semiconductors do not absorb in this part of the spectrum. In contrast, the near-field enhancement at higher energies by the AuNP can enhance the absorption rates of the QDs/TiO_2 assemblies. Therefore, when considering their effects driving the photodegradation of RhB, we should focus on the FE in wavelengths under 550 nm. At these wavelengths, our computational results predict that the contribution of AuNS@SiO_2 would be larger than that of AuNR@SiO_2 in a per-particle basis (see Figure 2.7). This is also the case when we consider the contribution to the local FE in a "per-atom" basis (see Figure 2.5e), which can be done by comparing the "excess" average field enhancement normalized by the AuNP volume. This conclusion provides an explanation for the experimental results in Figures 2.4b,c, where these are precisely the hybrids showing a faster photodegradation. This arises from the fact that we are considering colloidal NPs, so that the anisotropy of the AuNR implies that only a fraction of the ensemble will see its high-energy, transversal plasmonic mode excited at a given time, whereas the spherical symmetry of the AuNS guarantees a homogeneous performance in this regard.

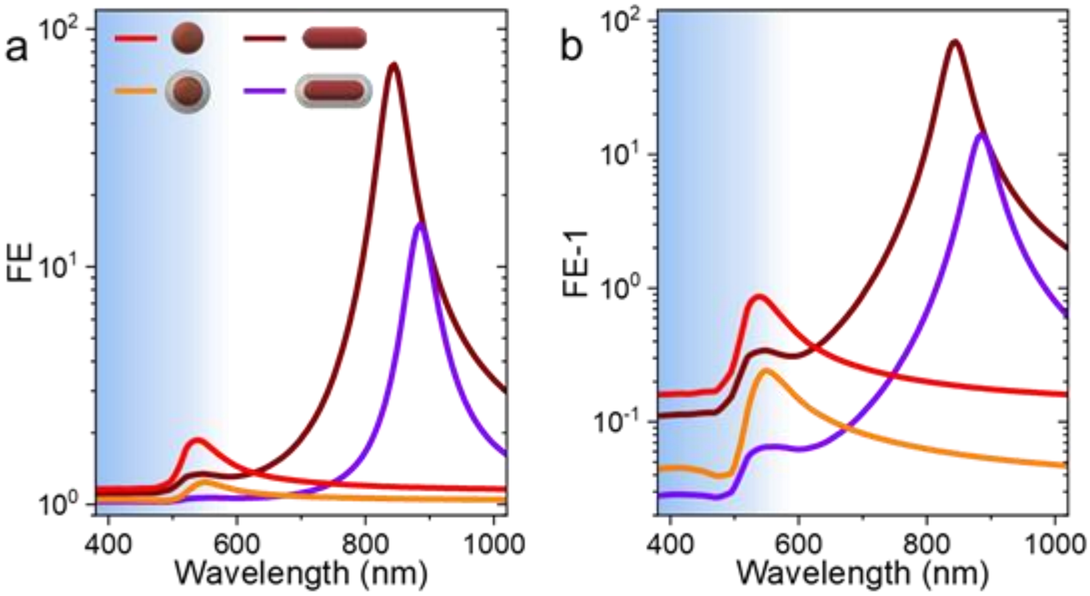

Fig. 2.7. Computational results for the different plasmonic nanoparticles used in this study. (a) Volume-averaged FE (see eq. 1 in the main text). (b) Increase on the average field enhancement, over a system without PNP. The blue-shaded area indicates the spectral region with non-zero QD absorption. Contrasting with the data in Figure 4e in the main text, these curves correspond to values per-PNP, instead of "per-atom".

Lastly, even though we have shown that the hybrid photocatalyists perform well when operating with the SiO_2 coating, we should consider that the shell separates the components from the surface of Au. This is, of course, by design, so as to impede charge transfer, but it also limits the possible advantage taken from the reaction's enhancement possible through the near-field of the AuNP. This can be clearly seen by contrasting the AuNS and AuNS@SiO_2 curves in Figure 2.5e, or by contrasting the electric field maps (Figure 2.5f,g). Consequently, one ought to consider the thickness of such insulating layers carefully, as design parameter with a large direct impact on the performance of the photocatalyst. Both theoretical[63] and experimental[37,64,65] work have suggested that insulating layers of around 10 nm over small PNPs can provide a good balance between reducing dissipation mechanisms and still allowing enhancement through near field interaction, with larger particles,[37] films[66] and structured metamaterials[67] having shown optima at larger thicknesses. Additionally, we present in Figure 2.8 a comparison of AuNRs coated with different SiO_2 thicknesses, showing how insulating layers above ~10 nm block the interaction between the PNPs and TiO_2 in RhB photodegradation experiments. On the other hand, SiO_2 layers under ~8 nm in thickness have often less regular shapes, introducing variability on the barrier thickness.

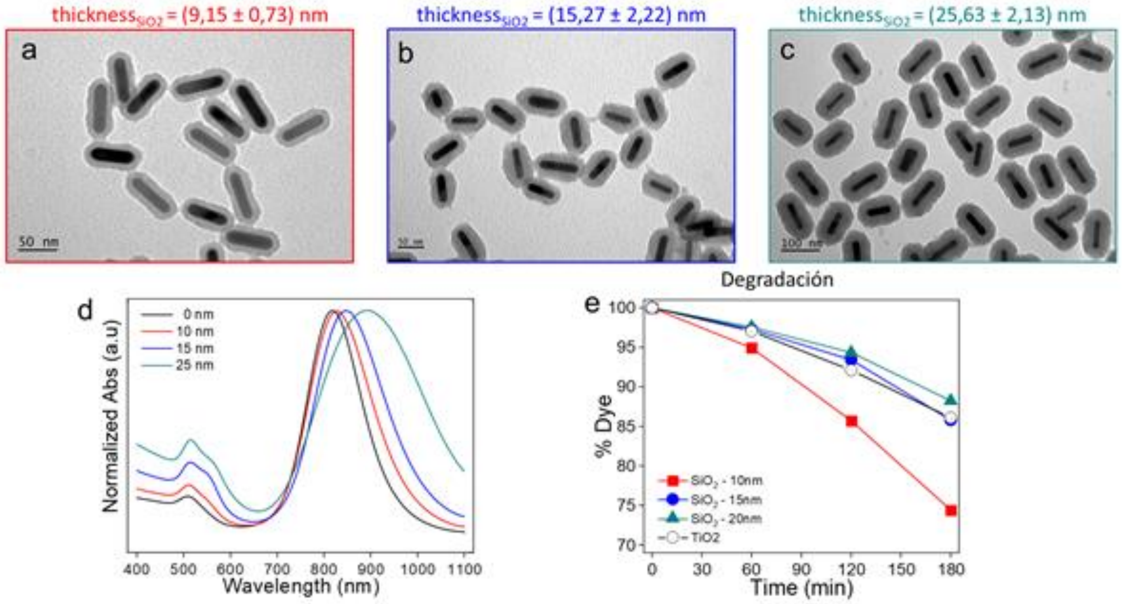

Fig. 2.8. Testing the impact of SiO_2 layer thickness. (a-c) TEM images of AuNRs with increasing SiO_2 thickness. (d) Normalized absorbance of the AuNRs@SiO_2 of the samples shown in the top panels. Increasing the thickness of the SiO_2 layer increases the redshift of the longitudinal plasmonic mode and introduces a secondary transversal mode. (d) RhB degradation results with hybrids composed by SiO_2 beads and loaded with AuNRs@SiO_2 and TiO_2 NPs. Rods covered with SiO_2 layers thicker than ~10 nm do not enhance the degradation obtained with TiO_2 alone.

2.4 Simulations

Theoretical modeling has been performed in order to allow a correct interpretation of the optical and photochemical data obtained experimentally. To do so, we have solved the classical electrodynamic response of the plasmonic particles using a solver that uses finite element methods (FEM), COMSOL Multiphysics, and from these results we have derived the relevant contribution of the different systems to hot carrier injection and near-field absorption enhancement. For the latter, we have computed the average field enhancement around the systems as

$$FE = \frac{\int_V \frac{|\boldsymbol{E}|^2}{E_0^2} dV}{\int_V dV} \qquad \text{eq.1}$$

where, **E** is the electric field, E_0 is the background field created by the incident planewave, and *V* is a volume surrounding the plasmonic material up to a distance of 20 nm of its surface. It is important to note that, in the case of SiO_2-coated AuNP, the boundary of this volume remains unchanged but the volume filled with SiO_2 is not included in *V*, as we are interested in the effect of the near field onto the absorption of TiO_2 or the QDs. The permittivity of the materials was taken from experimental values and were assumed to be immersed in a medium with dielectric constant *n* = 1.33. The permittivity of gold was broadened by a factor of two using the Drude model to account for crystal imperfections. The models for Au nanorods had 56 nm in length and 13 nm in diameter, and the Au spheres had 23 nm in diameter. In both cases the models with a SiO_2 layer had a thickness of 8 nm.

When it comes to computing the rate of excitation of intraband hot carriers at the surface of the plasmonic metal, we have used a formalism detailed in previous work.[74] In particular, we have used the expression

$$Rate_{\mathrm{HE}} \approx \frac{2}{\pi^2} \frac{e^2 E_F^2}{\hbar} \frac{\hbar\omega - \Delta E_b}{(\hbar\omega)^4} \int_{S_{\mathrm{NP}}} |E_{\mathrm{normal}}(\boldsymbol{r})|^2 \mathrm{ds}$$

to compute the rate of excitation of hot carriers with excess energy above $\Delta E = 1 \text{ eV}$. This expression is derived from a quantum formalism but uses the local results of the electric field inside of the Au metal from the classical simulations. In the above expression, E_{normal} (r) is the component of the field normal to the metal-environment interface, measured just inside the metal. The expression $\hbar\omega$ denotes the energy of the incoming photons, E_F is the Fermi energy of the metal, and S_{NP} is the surface of the metal particle. The intensity of the source of radiation was chosen as having a simple flat spectrum with an irradiance of $I_0 = 1.25 \text{ W/m}^2$ per wavelength, chosen as a representative value of a typical solar irradiance at sea level in the visible range.

2.5 Conclusion

We have refined a remarkable hierarchical layer-by-layer assembly protocol for the creation of advanced photocatalytic hybrid nanostructures. Through the strategic combination of PNP with CdS QDs, we have achieved an unprecedented enhancement of the photocatalytic activity displayed by TiO2 NPs. Within this catalyst family, the CdS QDs effectively utilize the near-field enhancement of the metal, underscoring the significance of spectral overlap between plasmon and semiconductor. In fact, in pursuing the optimization of these hybrid systems for photocatalysis, we have found that focusing on the near-field enhancement of the CdS QDs, bridging the energy transfer from SiO_2-coated PNPs to TiO_2 with an indirect charge transfer initiated in the QDs, yields the largest reaction rates. These rates surpass those arising from combining, using naked PNPs, hot electron injection and closer-range near-field enhancement due to the deleterious contribution of charge backtransfer to the naked metal. To conclude our exploration of hybrid composition engineering, we compared different sequences of photocatalyst element deposition and demonstrated the crucial importance of selecting an order that maximizes the coverage of PNP surface with CdS-QD@TiO2-NP groups. This is done to exploit the aforementioned indirect activation mechanism. Our study also explores systems in which near-field-initiated mechanisms coexist with hot carrier injection. The results obtained from hybrids containing uncoated PNPs demonstrate how selecting a PNP geometry that enhances hot carrier excitation rates - AuNRs in our study - becomes a superior overall photosensitizer. However, the competing effect of electron back-transfer renders this configuration suboptimal when using QDs as the intermediate photosensitizer. These results present a detailed picture of the interplay between the different energy transfer mechanisms involved in hybrid plasmonic photocatalytic systems and underscore the importance of further detailed nanoengineering studies. This serves as a path towards the synthesis of complexes that can optimize the different contributions of each component.

2.6 References

(1) Fujishima, A.; Zhang, X.; Tryk, D. A. TiO2 Photocatalysis and Related Surface Phenomena. *Surf. Sci. Rep.* **2008**, *63* (12), 515–582. https://doi.org/10.1016/j.surfrep.2008.10.001.

(2) Sousa-Castillo, A.; Couceiro, J. R.; Tomás-Gamasa, M.; Mariño-López, A.; López, F.; Baaziz, W.; Ersen, O.; Comesaña-Hermo, M.; Mascareñas, J. L.; Correa-Duarte, M. A. Remote Activation of Hollow Nanoreactors for Heterogeneous Photocatalysis in Biorelevant Media. *Nano Lett.* **2020**, *20* (10), 7068–7076. https://doi.org/10.1021/acs.nanolett.0c02180.

(3) Chen, J. J.; Wu, J. C. S.; Wu, P. C.; Tsai, D. P. Plasmonic Photocatalyst for H2 Evolution in Photocatalytic Water Splitting. *J. Phys. Chem. C* **2011**, *115* (1), 210–216. https://doi.org/10.1021/jp1074048.

(4) Malato, S.; Fernández-Ibáñez, P.; Maldonado, M. I.; Blanco, J.; Gernjak, W. Decontamination and Disinfection of Water by Solar Photocatalysis: Recent Overview and Trends. *Catal. Today* **2009**, *147* (1), 1–59. https://doi.org/10.1016/j.cattod.2009.06.018.

(5) Keane, D. A.; McGuigan, K. G.; Ibáñez, P. F.; Polo-López, M. I.; Byrne, J. A.; Dunlop, P. S. M.; O'Shea, K.; Dionysiou, D. D.; Pillai, S. C. Solar Photocatalysis for Water Disinfection: Materials and Reactor Design. *Catal. Sci. Technol.* **2014**, *4* (5), 1211–1226. https://doi.org/10.1039/c4cy00006d.

(6) Afzal, S.; Daoud, W. A.; Langford, S. J. Photostable Self-Cleaning Cotton by a Copper(II) Porphyrin/TiO2 Visible-Light Photocatalytic System. *ACS Appl. Mater. Interfaces* **2013**, *5* (11), 4753–4759. https://doi.org/10.1021/am400002k.

(7) Linic, S.; Christopher, P.; Ingram, D. B. Plasmonic-Metal Nanostructures for Efficient Conversion of Solar to Chemical Energy. *Nat. Mater.* **2011**, *10* (12), 911–921. https://doi.org/10.1038/nmat3151.

(8) Zhang, G.; Kim, G.; Choi, W. Visible Light Driven Photocatalysis Mediated via

Ligand-to-Metal Charge Transfer (LMCT): An Alternative Approach to Solar Activation of Titania. *Energy Environ. Sci.* **2014**, *7* (3), 954–966. https://doi.org/10.1039/c3ee43147a.

(9) Devi, L. G.; Kavitha, R. A Review on Non Metal Ion Doped Titania for the Photocatalytic Degradation of Organic Pollutants under UV/Solar Light: Role of Photogenerated Charge Carrier Dynamics in Enhancing the Activity. *Appl. Catal. B Environ.* **2013**, *140–141*, 559–587. https://doi.org/10.1016/j.apcatb.2013.04.035.

(10) Dozzi, M. V.; Selli, E. Doping TiO2 with P-Block Elements: Effects on Photocatalytic Activity. *J. Photochem. Photobiol. C Photochem. Rev.* **2013**, *14* (1), 13–28. https://doi.org/10.1016/j.jphotochemrev.2012.09.002.

(11) Sousa-Castillo, A.; Comesaña-Hermo, M.; Rodríguez-González, B.; Pérez-Lorenzo, M.; Wang, Z.; Kong, X. T.; Govorov, A. O.; Correa-Duarte, M. A. Boosting Hot Electron-Driven Photocatalysis through Anisotropic Plasmonic Nanoparticles with Hot Spots in Au-TiO2 Nanoarchitectures. *J. Phys. Chem. C* **2016**, *120* (21), 11690–11699. https://doi.org/10.1021/acs.jpcc.6b02370.

(12) Cushing, S. K.; Li, J.; Meng, F.; Senty, T. R.; Suri, S.; Zhi, M.; Li, M.; Bristow, A. D.; Wu, N. Photocatalytic Activity Enhanced by Plasmonic Resonant Energy Transfer from Metal to Semiconductor. *J. Am. Chem. Soc.* **2012**, *134* (36), 15033–15041. https://doi.org/10.1021/ja305603t.

(13) Cushing, S. K.; Li, J.; Bright, J.; Yost, B. T.; Zheng, P.; Bristow, A. D.; Wu, N. Controlling Plasmon-Induced Resonance Energy Transfer and Hot Electron Injection Processes in Metal@TiO2 Core-Shell Nanoparticles. *J. Phys. Chem. C* **2015**, *119* (28), 16239–16244. https://doi.org/10.1021/acs.jpcc.5b03955.

(14) Bumajdad, A.; Madkour, M. Understanding the Superior Photocatalytic Activity of Noble Metals Modified Titania under UV and Visible Light Irradiation. *Phys. Chem. Chem. Phys.* **2014**, *16* (16), 7146–7158. https://doi.org/10.1039/c3cp54411g.

(15) Ma, X. C.; Dai, Y.; Yu, L.; Huang, B. B. Energy Transfer in Plasmonic Photocatalytic Composites. *Light Sci. Appl.* **2016**, *5* (April 2015). https://doi.org/10.1038/lsa.2016.17.

(16) Vu, N. N.; Kaliaguine, S.; Do, T. O. Plasmonic Photocatalysts for Sunlight-Driven Reduction of CO2: Details, Developments, and Perspectives. *ChemSusChem* **2020**, *13* (16), 3967–3991. https://doi.org/10.1002/cssc.202000905.

(17) Mascaretti, L.; Naldoni, A. Hot Electron and Thermal Effects in Plasmonic Photocatalysis. *J. Appl. Phys.* **2020**, *128* (4). https://doi.org/10.1063/5.0013945.

(18) Baffou, G.; Bordacchini, I.; Baldi, A.; Quidant, R. Simple Experimental Procedures to Distinguish Photothermal from Hot-Carrier Processes in Plasmonics. *Light Sci. Appl.* **2020**, *9*, 108. https://doi.org/10.1038/s41377-020-00345-0.

(19) Negrín-Montecelo, Y.; Brissaud, C.; Piquemal, J. Y.; Govorov, A. O.; Correa-Duarte, M. A.; Besteiro, L. V.; Comesaña-Hermo, M. Plasmonic Photocatalysis in Aqueous Solution: Assessing the Contribution of Thermal Effects and

Evaluating the Role of Photogenerated ROS. *Nanoscale* **2022**, *14* (32), 11612–11618. https://doi.org/10.1039/d2nr02431d.

(20) Rej, S.; Santiago, E. Y.; Baturina, O.; Zhang, Y.; Burger, S.; Kment, S.; Govorov, A. O.; Naldoni, A. Colloidal Titanium Nitride Nanobars for Broadband Inexpensive Plasmonics and Photochemistry from Visible to Mid-IR Wavelengths. *Nano Energy* **2022**, *104* (October). https://doi.org/10.1016/j.nanoen.2022.107989.

(21) Rej, S.; Mascaretti, L.; Santiago, E. Y.; Tomanec, O.; Kment, Š.; Wang, Z.; Zbořil, R.; Fornasiero, P.; Govorov, A. O.; Naldoni, A. Determining Plasmonic Hot Electrons and Photothermal Effects during H2 Evolution with TiN-Pt Nanohybrids. *ACS Catal.* **2020**, *10* (9), 5261–5271. https://doi.org/10.1021/acscatal.0c00343.

(22) Richardson, H. H.; Carlson, M. T.; Tandler, P. J.; Hernandez, P.; Govorov, A. O. Experimental and Theoretical Studies of Light-to-Heat Conversion and Collective Heating Effects in Metal Nanoparticle Solutions. *Nano Lett.* **2009**, *9* (3), 1139–1146. https://doi.org/10.1021/nl8036905.

(23) Besteiro, L. V; Alabastri, A.; Baldi, A.; Tagliabue, G. Challenges in Plasmonic Catalysis. *ACS Nano.* **2020**, *14* (12), 16202–16219. https://doi.org/10.1021/acsnano.0c08773.

(24) Kale, M. J.; Avanesian, T.; Christopher, P. Direct Photocatalysis by Plasmonic Nanostructures. *ACS Catal.* **2014**, *4* (1), 116–128. https://doi.org/10.1021/cs400993w.

(25) Jin, R.; Cao, Y. C.; Hao, E.; Métraux, G. S.; Schatz, G. C.; Mirkin, C. A. Le Growth through Plasmon ExcitatioControlling Anisotropic Nanoparticn. *Nature* **2003**, *425* (6957), 487–490. https://doi.org/10.1038/nature02020.

(26) Bhanushali, S.; Mahasivam, S.; Ramanathan, R.; Singh, M.; Harrop Mayes, E. L.; Murdoch, B. J.; Bansal, V.; Sastry, M. Photomodulated Spatially Confined Chemical Reactivity in a Single Silver Nanoprism. *ACS Nano* **2020**, *14* (9), 11100–11109. https://doi.org/10.1021/acsnano.0c00966.

(27) Movsesyan, A.; Muravitskaya, A.; Besteiro, L. V.; Santiago, E. Y.; Ávalos-Ovando, O.; Correa-Duarte, M. A.; Wang, Z.; Markovich, G.; Govorov, A. O. Creating Chiral Plasmonic Nanostructures Using Chiral Light in a Solution and on a Substrate: The Near-Field and Hot-Electron Routes. *Adv. Opt. Mater.* **2023**, *2300013*, 1–18. https://doi.org/10.1002/adom.202300013.

(28) Negrin-Montecelo, Y.; Movsesyan, A.; Gao, J.; Burger, S.; Wang, Z. M.; Nlate, S.; Pouget, E.; Oda, R.; Comesana-Hermo, M.; Govorov, A. O.; Correa-Duarte, M. A. Chiral Generation of Hot Carriers for Polarization-Sensitive Plasmonic Photocatalysis. *J. Am. Chem. Soc.* **2022**, *144* (4), 1663–1671. https://doi.org/10.1021/jacs.1c10526.

(29) Ávalos-Ovando, O.; Santiago, E. Y.; Movsesyan, A.; Kong, X. T.; Yu, P.; Besteiro, L. V.; Khorashad, L. K.; Okamoto, H.; Slocik, J. M.; Correa-Duarte, M. A.; Comesaña-Hermo, M.; Liedl, T.; Wang, Z.; Markovich, G.; Burger, S.; Govorov, A. O. Chiral Bioinspired Plasmonics: A Paradigm Shift for Optical Activity and Photochemistry. *ACS Photonics* **2022**, *9* (7), 2219–2236.

https://doi.org/10.1021/acsphotonics.2c00445.

(30) Wang, J.; Koo, K. M.; Wang, Y.; Trau, M. Engineering State-of-the-Art Plasmonic Nanomaterials for SERS-Based Clinical Liquid Biopsy Applications. *Adv. Sci.* **2019**, *6* (23). https://doi.org/10.1002/advs.201900730.

(31) Phan-Quang, G. C.; Han, X.; Koh, C. S. L.; Sim, H. Y. F.; Lay, C. L.; Leong, S. X.; Lee, Y. H.; Pazos-Perez, N.; Alvarez-Puebla, R. A.; Ling, X. Y. Three-Dimensional Surface-Enhanced Raman Scattering Platforms: Large-Scale Plasmonic Hotspots for New Applications in Sensing, Microreaction, and Data Storage. *Acc. Chem. Res.* **2019**, *52* (7), 1844–1854. https://doi.org/10.1021/acs.accounts.9b00163.

(32) Brongersma, M. L.; Halas, N. J.; Nordlander, P. Plasmon-Induced Hot Carrier Science and Technology. *Nat. Nanotechnol.* **2015**, *10* (1), 25–34. https://doi.org/10.1038/nnano.2014.311.

(33) Negrín-Montecelo, Y.; Comesaña-Hermo, M.; Khorashad, L. K.; Sousa-Castillo, A.; Wang, Z.; Pérez-Lorenzo, M.; Liedl, T.; Govorov, A. O.; Correa-Duarte, M. A. Photophysical Effects behind the Efficiency of Hot Electron Injection in Plasmon-Assisted Catalysis: The Joint Role of Morphology and Composition. *ACS Energy Lett.* **2020**, 395–402. https://doi.org/10.1021/acsenergylett.9b02478.

(34) Negrín-Montecelo, Y.; Comesaña-Hermo, M.; Kong, X. T.; Rodríguez-González, B.; Wang, Z.; Pérez-Lorenzo, M.; Govorov, A. O.; Correa-Duarte, M. A. Traveling Hot Spots in Plasmonic Photocatalysis: Manipulating Interparticle Spacing for Real-Time Control of Electron Injection. *ChemCatChem* **2018**, *10* (7), 1561–1565. https://doi.org/10.1002/cctc.201702053.

(35) Negrín-Montecelo, Y.; Kong, X. T.; Besteiro, L. V.; Carbó-Argibay, E.; Wang, Z. M.; Pérez-Lorenzo, M.; Govorov, A. O.; Comesaña-Hermo, M.; Correa-Duarte, M. A. Synergistic Combination of Charge Carriers and Energy-Transfer Processes in Plasmonic Photocatalysis. *ACS Appl. Mater. Interfaces* **2022**, *14* (31), 35734–35744. https://doi.org/10.1021/acsami.2c08685.

(36) Sakthivel, S.; Shankar, M. V.; Palanichamy, M.; Arabindoo, B.; Bahnemann, D. W.; Murugesan, V. Enhancement of Photocatalytic Activity by Metal Deposition: Characterisation and Photonic Efficiency of Pt, Au and Pd Deposited on TiO 2 Catalyst. *Water Res.* **2004**, *38* (13), 3001–3008. https://doi.org/10.1016/j.watres.2004.04.046.

(37) Torimoto, T.; Horibe, H.; Kameyama, T.; Okazaki, K. I.; Ikeda, S.; Matsumura, M.; Ishikawa, A.; Ishihara, H. Plasmon-Enhanced Photocatalytic Activity of Cadmium Sulfide Nanoparticle Immobilized on Silica-Coated Gold Particles. *J. Phys. Chem. Lett.* **2011**, *2* (16), 2057–2062. https://doi.org/10.1021/jz2009049.

(38) Hayashido, Y.; Naya, S. I.; Tada, H. Local Electric Field-Enhanced Plasmonic Photocatalyst: Formation of Ag Cluster-Incorporated AgBr Nanoparticles on TiO2. *J. Phys. Chem. C* **2016**, *120* (35), 19663–19669. https://doi.org/10.1021/acs.jpcc.6b04894.

(39) Li, K.; Hogan, N. J.; Kale, M. J.; Halas, N. J.; Nordlander, P.; Christopher, P. Balancing Near-Field Enhancement, Absorption, and Scattering for Effective Antenna-Reactor Plasmonic Photocatalysis. *Nano Lett.* **2017**, *17* (6), 3710–3717.

https://doi.org/10.1021/acs.nanolett.7b00992.

(40) Li, J.; Cushing, S. K.; Meng, F.; Senty, T. R.; Bristow, A. D.; Wu, N. Plasmon-Induced Resonance Energy Transfer for Solar Energy Conversion. *Nat. Photonics* **2015**, *9* (9), 601–607. https://doi.org/10.1038/nphoton.2015.142.

(41) Gao, X. F.; Sun, W. T.; Hu, Z. D.; Ai, G.; Zhang, Y. L.; Feng, S.; Li, F.; Peng, L. M. An Efficient Method to Form Heterojunction CdS/TiO2 Photoelectrodes Using Highly Ordered TiO2 Nanotube Array Films. *J. Phys. Chem. C* **2009**, *113* (47), 20481–20485. https://doi.org/10.1021/jp904320d.

(42) Peter, L. M.; Riley, D. J.; Tull, E. J.; Wijayantha, K. G. U. Photosensitization of Nanocrystalline TiO2 by Self-Assembled Layers of CdS Quantum Dots. *Chem. Commun.* **2002**, *10*, 1030–1031. https://doi.org/10.1039/b201661c.

(43) Bjelajac, A.; Petrović, R.; Nedeljković, J. M.; Djokić, V.; Radetić, T.; Ćirković, J.; Janaćković, D. Ex-Situ Sensitization of Ordered TiO2 Nanotubes with CdS Quantum Dots. *Ceram. Int.* **2015**, *41* (5), 7048–7053. https://doi.org/10.1016/j.ceramint.2015.02.010.

(44) Maiti, S.; Dana, J.; Ghosh, H. N. Correlating Charge-Carrier Dynamics with Efficiency in Quantum-Dot Solar Cells: Can Excitonics Lead to Highly Efficient Devices? *Chem. - A Eur. J.* **2019**, *25* (3), 692–702. https://doi.org/10.1002/chem.201801853.

(45) Nasir, J. A.; Rehman, Z. U.; Shah, S. N. A.; Khan, A.; Butler, I. S.; Catlow, C. R. A. Recent Developments and Perspectives in CdS-Based Photocatalysts for Water Splitting. *J. Mater. Chem. A* **2020**, *8* (40), 20752–20780. https://doi.org/10.1039/d0ta05834c.

(46) Yalavarthi, R.; Mascaretti, L.; Kudyshev, Z. A.; Dutta, A.; Kalytchuk, S.; Zbořil, R.; Schmuki, P.; Shalaev, V. M.; Kment, Š.; Boltasseva, A.; Naldoni, A. Enhancing Photoelectrochemical Energy Storage by Large-Area CdS-Coated Nickel Nanoantenna Arrays. *ACS Appl. Energy Mater.* **2021**, *4* (10), 11367–11376. https://doi.org/10.1021/acsaem.1c02183.

(47) Zheng, L.; Teng, F.; Ye, X.; Zheng, H.; Fang, X. Photo/Electrochemical Applications of Metal Sulfide/TiO2 Heterostructures. *Adv. Energy Mater.* **2020**, *10* (1), 1–32. https://doi.org/10.1002/aenm.201902355.

(48) Zhao, D.; Yang, C. F. Recent Advances in the TiO2/CdS Nanocomposite Used for Photocatalytic Hydrogen Production and Quantum-Dot-Sensitized Solar Cells. *Renew. Sustain. Energy Rev.* **2016**, *54*, 1048–1059. https://doi.org/10.1016/j.rser.2015.10.100.

(49) Li, J.; Cushing, S. K.; Zheng, P.; Senty, T.; Meng, F.; Bristow, A. D.; Manivannan, A.; Wu, N. Solar Hydrogen Generation by a CdS-Au-TiO2 Sandwich Nanorod Array Enhanced with Au Nanoparticle as Electron Relay and Plasmonic Photosensitizer. *J. Am. Chem. Soc.* **2014**, *136* (23), 8438–8449. https://doi.org/10.1021/ja503508g.

(50) Kandi, D.; Behera, A.; Martha, S.; Naik, B.; Parida, K. M. Quantum Confinement Chemistry of CdS QDs plus Hot Electron of Au over TiO2 Nanowire Protruding to Be Encouraging Photocatalyst towards Nitrophenol Conversion and Ciprofloxacin Degradation. *J. Environ. Chem. Eng.* **2019**, *7* (1), 102821.

https://doi.org/10.1016/j.jece.2018.102821.

(51) Zhao, H.; Huang, F.; Hou, J.; Liu, Z.; Wu, Q.; Cao, H.; Jing, Q.; Peng, S.; Cao, G. Efficiency Enhancement of Quantum Dot Sensitized TiO2/ZnO Nanorod Arrays Solar Cells by Plasmonic Ag Nanoparticles. *ACS Appl. Mater. Interfaces* **2016**, *8* (40), 26675–26682. https://doi.org/10.1021/acsami.6b06386.

(52) Zhao, W.; Liu, J.; Deng, Z.; Zhang, J.; Ding, Z.; Fang, Y. Facile Preparation of Z-Scheme CdS–Ag–TiO2 Composite for the Improved Photocatalytic Hydrogen Generation Activity. *Int. J. Hydrogen Energy* **2018**, *43* (39), 18232–18241. https://doi.org/10.1016/j.ijhydene.2018.08.026.

(53) Swearer, D. F.; Zhao, H.; Zhou, L.; Zhang, C.; Robatjazi, H.; Martirez, J. M. P.; Krauter, C. M.; Yazdi, S.; McClain, M. J.; Ringe, E.; Carter, E. A.; Nordlander, P.; Halas, N. J. Heterometallic Antenna-Reactor Complexes for Photocatalysis. *Proc. Natl. Acad. Sci. U. S. A.* **2016**, *113* (32), 8916–8920. https://doi.org/10.1073/pnas.1609769113.

(54) Yalavarthi, R.; Yesilyurt, O.; Henrotte, O.; Kment, Š.; Shalaev, V. M.; Boltasseva, A.; Naldoni, A. Multimetallic Metasurfaces for Enhanced Electrocatalytic Oxidations in Direct Alcohol Fuel Cells. *Laser Photonics Rev.* **2022**, *16* (7), 1–10. https://doi.org/10.1002/lpor.202200137.

(55) Yalavarthi, R.; Henrotte, O.; Kment, Š.; Naldoni, A. Determining the Role of Pd Catalyst Morphology and Deposition Criteria over Large Area Plasmonic Metasurfaces during Light-Enhanced Electrochemical Oxidation of Formic Acid. *J. Chem. Phys.* **2022**, *157* (11). https://doi.org/10.1063/5.0102012.

(56) Liz-Marzán, L. M.; Giersig, M.; Mulvaney, P. Synthesis of Nanosized Gold-Silica Core-Shell Particles. *Langmuir* **1996**, *12* (18), 4329–4335. https://doi.org/10.1021/la9601871.

(57) Caruso, F.; Caruso, R. A.; Möhwald, H. Nanoengineering of Inorganic and Hybrid Hollow Spheres by Colloidal Templating. *Science (80-.).* **1998**, *282* (5391), 1111–1114. https://doi.org/10.1126/science.282.5391.1111.

(58) Funston, A. M.; Novo, C.; Davis, T. J.; Mulvaney, P. Plasmon Coupling of Gold Nanorods at Short Distances and in Different Geometries. *Nano Lett.* **2009**, *9* (4), 1651–1658. https://doi.org/10.1021/nl900034v.

(59) Su, K. H.; Wei, Q. H.; Zhang, X.; Mock, J. J.; Smith, D. R.; Schultz, S. Interparticle Coupling Effects on Plasmon Resonances of Nanogold Particles. *Nano Lett.* **2003**, *3* (8), 1087–1090. https://doi.org/10.1021/nl034197f.

(60) Santiago, E. Y.; Besteiro, L. V.; Kong, X.-T.; Correa-Duarte, M. A.; Wang, Z.; Govorov, A. O. Efficiency of Hot-Electron Generation in Plasmonic Nanocrystals with Complex Shapes: Surface-Induced Scattering, Hot Spots, and Interband Transitions. *ACS Photonics* **2020**, *7* (10), 2807–2824. https://doi.org/10.1021/acsphotonics.0c01065.

(61) Enthaler, S.; Von Langermann, J.; Schmidt, T. Carbon Dioxide and Formic Acid - The Couple for Environmental-Friendly Hydrogen Storage? *Energy Environ. Sci.* **2010**, *3* (9), 1207–1217. https://doi.org/10.1039/b907569k.

(62) Selopal, G. S.; Mohammadnezhad, M.; Besteiro, L. V.; Cavuslar, O.; Liu, J.;

Zhang, H.; Navarro-Pardo, F.; Liu, G.; Wang, M.; Durmusoglu, E. G.; Acar, H. Y.; Sun, S.; Zhao, H.; Wang, Z. M.; Rosei, F. Synergistic Effect of Plasmonic Gold Nanoparticles Decorated Carbon Nanotubes in Quantum Dots/TiO2 for Optoelectronic Devices. *Adv. Sci.* **2020**, *7* (20), 1–15. https://doi.org/10.1002/advs.202001864.

(63) Anger, P.; Bharadwaj, P.; Novotny, L. Enhancement and Quenching of Single-Molecule Fluorescence. *Phys. Rev. Lett.* **2006**, *96* (11). https://doi.org/10.1103/PhysRevLett.96.113002.

(64) Wang, Z.; Gao, W.; Wang, R.; Shao, J.; Han, Q.; Wang, C.; Zhang, J.; Zhang, T.; Dong, J.; Zheng, H. Influence of SiO2 Layer on the Plasmon Quenched Upconversion Luminescence Emission of Core-Shell NaYF4:Yb,Er@SiO2@Ag Nanocomposites. *Mater. Res. Bull.* **2016**, *83*, 515–521. https://doi.org/10.1016/j.materresbull.2016.06.035.

(65) Rohani, S.; Quintanilla, M.; Tuccio, S.; De Angelis, F.; Cantelar, E.; Govorov, A. O.; Razzari, L.; Vetrone, F. Enhanced Luminescence, Collective Heating, and Nanothermometry in an Ensemble System Composed of Lanthanide-Doped Upconverting Nanoparticles and Gold Nanorods. *Adv. Opt. Mater.* **2015**, *3* (11), 1606–1613. https://doi.org/10.1002/adom.201500380.

(66) Su, Q.; Jiang, C.; Gou, D.; Long, Y. Surface Plasmon-Assisted Fluorescence Enhancing and Quenching: From Theory to Application. *ACS Appl. Bio Mater.* **2021**, *4* (6), 4684–4705. https://doi.org/10.1021/acsabm.1c00320.

(67) Damm, S.; Fedele, S.; Murphy, A.; Holsgrove, K.; Arredondo, M.; Pollard, R.; Barry, J. N.; Dowling, D. P.; Rice, J. H. Plasmon Enhanced Fluorescence Studies from Aligned Gold Nanorod Arrays Modified with SiO2 Spacer Layers. *Appl. Phys. Lett.* **2015**, *106* (18). https://doi.org/10.1063/1.4919968.

(68) Stöber, W.; Fink, A.; Bohn, E. Controlled Growth of Monodisperse Silica Spheres in the Micron Size Range. *J. Colloid Interface Sci.* **1968**, *26* (1), 62–69. https://doi.org/10.1016/0021-9797(68)90272-5.

(69) Bastús, N. G.; Comenge, J.; Puntes, V. Kinetically Controlled Seeded Growth Synthesis of Citrate-Stabilized Gold Nanoparticles of up to 200 Nm: Size Focusing versus Ostwald Ripening. *Langmuir* **2011**, *27* (17), 11098–11105. https://doi.org/10.1021/la201938u.

(70) Scarabelli, L.; Sánchez-Iglesias, A.; Pérez-Juste, J.; Liz-Marzán, L. M. A “Tips and Tricks” Practical Guide to the Synthesis of Gold Nanorods. *J. Phys. Chem. Lett.* **2015**, *6* (21), 4270–4279. https://doi.org/10.1021/acs.jpclett.5b02123.

(71) Pastoriza-Santos, I.; Pérez-Juste, J.; Liz-Marzán, L. M. Silica-Coating and Hydrophobation of CTAB-Stabilized Gold Nanorods. *Chem. Mater.* **2006**, *18,* 2465–2467.

(72) Fernández-López, C.; Mateo-Mateo, C.; Álvarez-Puebla, R. A.; Pérez-Juste, J.; Pastoriza-Santos, I.; Liz-Marzán, L. M. Highly Controlled Silica Coating of PEG-Capped Metal Nanoparticles and Preparation of SERS-Encoded Particles. *Langmuir* **2009**, *25* (24), 13894–13899. https://doi.org/10.1021/la9016454.

(73) Bae, W.; Abdullah, R.; Mehera, R. Cysteine-Mediated Synthesis of CdS Bionanocrystallites. *Chemosphere* **1998**, *37* (2), 363–385.

(74) Besteiro, L. V.; Kong, X. T.; Wang, Z.; Hartland, G.; Govorov, A. O. Understanding Hot-Electron Generation and Plasmon Relaxation in Metal Nanocrystals: Quantum and Classical Mechanisms. *ACS Photonics* **2017**, *4* (11), 2759–2781. https://doi.org/10.1021/acsphotonics.7b00751.

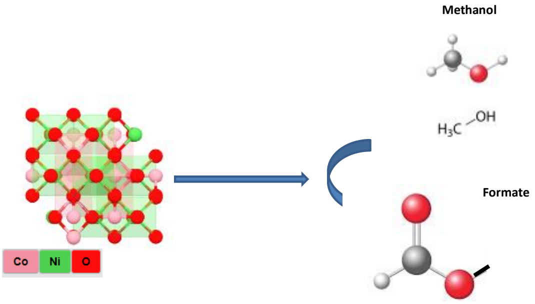

CHAPTER 3

Selective electrocatalytic conversion of methanol to formate over cobalt-nickel mixed oxide nanosheets

Methanol oxidation to formate has gathered greater attention due to its higher economic value than the fuel cell itself and is considered to be an essential chemical in many sectors, such as the textile, pharmaceutical, and printing industries. Currently, formic acid is industrially produced by the reaction of methanol with CO at elevated pressure and temperature which makes its production cost-prohibitive. In this study, by varying the reaction temperature, surfactant type, and Ni: Co stoichiometric ratio (Co: Ni = 1:1, 2:1 and 3:1), pure nickel cobaltite phase and mixed phases of nickel cobaltite nanosheets with nickel oxide were prepared by hydrothermal synthesis. The synthesized nanoparticles exhibit nearly 100 % electrochemical conversion of methanol to formate under normal conditions of pressure and temperature. When CONi (2:1) used as an anode for methanol electrocatalytic oxidation, achieves the highest current density value up till now (290 mA/cm^2 at 1.65 V (vs. RHE)) in 1 M KOH and 2 M methanol. Additionally, the best-performing material retains 100 % of the initial anodic current density for 33 h, surpassing state-of-the-art catalysts for this reaction. A battery of characterization techniques including XRD, EDS, SEM, HRTEM, XPS, and CO voltammetry enabled us to rationalize the reasons behind this behavior, which mostly relates to the higher amount of active sites. This work provides a straightforward and efficient way for the conversion of methanol to more valuable materials organic materials and the first evidence of a selective formate reaction pathway opening new opportunities for the design of novel materials for the production of commodities.

3.1 Introduction

The depletion of fossil resources and increased concerns about global warming prompt the development of sustainable and carbon-neutral energy sources[1]. Among different bio-based platform molecules, methanol is particularly attractive as it serves as a starting material for the manufacture of a multitude of chemicals and could be applied as an energy carrier in the future [2]. It allows an easy storage and transportation and could be distributed using the already available infrastructure. As an alternative to the fossil fuel-based process, methanol can be obtained from CO_2 and different forms of biomass, including municipal, agricultural, and forest waste [3]. All this provides direct methanol fuel cells (DMFCs) with enormous potential to power electric cars and mobile applications in a sustainable manner in the near future [4]. However, their practical implementation is currently hampered by the lack of efficient catalysts, particularly for the methanol oxidation reaction (MOR) [5]. The latter was originally reported over Ru-, Pd-, and Pt-based electrodes in both acid and alkaline electrolytes to give way to Earth-abundant nickel-based materials, including oxides/hydroxides, metal alloys, phosphides, chalcogenides, nitrides, and carbides [5]. In the case of the noble metals, the reaction mostly proceeds through a dual path mechanism, one leading to CO and the other to CO_2 evolution *via* formate intermediates [6, 7] that, in spite of offering high initial current densities, they suffer from rapid deactivation due to CO poisoning of the active sites. Moreover, as in the case of the nickel-based materials, the reaction leads to the formation of CO_2 greenhouse gas as the complete oxidation product of methanol [8-10]. Alternatively, the selective transformation of methanol to formic acid or formate intermediates, that weakly bond to the catalyst surface and easily dissolve in alkaline media, is gaining recent attention. Currently, close to one million tons of formic acid are produced yearly from the combination of methanol with CO at 40 atm and 80°C and the hydrolysis of the resulting methyl formate [11]. Owing to the energy intensification of this process, the price per metric ton of formate is a fourfold higher than that of methanol [12]. Thus, the availability of an industrially viable renewable process is regarded as crucial considering that the global market of formic acid is expected to increase by approximately 4% during the period 2022-2027 owing to its broadening application in different industrial sectors [13] and, especially, to its emerging role as an efficient and safe hydrogen carrier in fuel cell technologies and, potentially, in biomass upgrading [14].

NiO and Co_3O_4 are the most widely investigated non-platinum catalysts because of their relative low cost and high activity. However, their low electronic conductivity hampers their practical implementation. In an attempt to increase the electronic conductivity and electrocatalytic activity of these materials, nickel-based catalysts (*e.g.*, branched Ni_3C [5], FeCoNi disulfide nanosheets [15], $Ni(OH)_2$/NF [16], NiCoPO [17], and Pt-NP/NiO-NS [18]) and Co-based catalysts (*e.g.*, $Co(OH)_2$@HOS [18], Pt–Co_3O_4 [18], and Cu_2Se/Co_3Se_4 [19]) have been reported for the selective transformation of methanol to formates. On a different note, the incorporation of Ni^{2+} ions into octahedral sites in Co_3O_4 spinel structure results in the formation of $NiCo_2O_4$ nanostructures with much better electronic conductivity than the individual components, *i.e.*, at least two orders of magnitude higher than nickel oxide and cobalt oxide [20]. Indeed, the successful demonstration of $NiCo_2O_4$ triggered further investigations that focused on the effect of intermixing NiO and Co_3O_4 on the final morphology and electronic conductivity of $NiCo_2O_4$ nanostructures. So far, the synthesis of 1D nanowires, nanorods, nanotubes, 2D nanosheets, nanoflakes, and 3D hierarchical structures such as urchin-like structures, nanoflowers, and arrays composed of nanowires, nanorods, nanoflakes, and nanosheets have been comprehensively investigated with a variety of applications in Li-ion batteries, capacitors, electrocatalysts, and optoelectronic and magnetic devices [21].

Herein, we have studied the effect of the composition of cobalt-nickel mixed oxide nanosheets for the methanol oxidation reaction to formates. The materials were prepared by hydrothermal synthesis and characterized by bulk and surface techniques to determine structural and chemical features. The activity and stability of the catalysts were evaluated in the methanol oxidation reaction at different methanol concentrations. Our results underscore the necessity to optimize the Ni:Co ratio in order to obtain a stable, selective, and active catalytic system for methanol oxidation.

3.2 Experimental

3.2.1. Materials synthesis

3.2.1.1 Chemicals

Cobalt(II) nitrate hexahydrate (98%), nickel(II) nitrate hexahydrate (94.5%), urea (99%), potassium hydroxide pellets (85%), sodium borohydride (97%), ethylenile glycol (99%), methanol (99.8%), 5 wt.% Nafion^{TM} perfluorinated resin solution were purchased from Sigma-Aldrich and were used as received. Isopropanol (99.8%) was acquired from Scharlau and used as received.

3.2.1.2 Synthesis of Cobalt-nickel mixed oxides CoNi 1:1, CoNi 2:1, and CoNi 3:1

Cobalt-nickel mixed oxides (CoNi) samples with different Co:Ni molar ratios (Co:Ni = 1:1, 2:1, 3:1) coded CoNi 1:1, CoNi 2:1, and CoNi 3:1 were prepared according to the following protocol. 0.872 g of nickel nitrate and the corresponding amount of cobalt(II) nitrate hexahydrate were mixed with 2.16 g of urea and dissolved in 60 mL of distilled water and 5 mL of ethylene glycol. The resulting solution was sonicated for 20 min and placed in a stainless steel autoclave, which was heated at 150°C at a heating rate of 4ºC min^{-1} for 16 h. The precipitate was separated by centrifugation and the excess of reagents was removed by three centrifugation-redispersion cycles with distilled water (5000 g, 30 min), and then dried at 60°C for 24 h. The resulting samples were calcined under static air at 375°C for 3 h (3ºC min^{-1}).

3.2.2 Characterization

X-ray diffraction (XRD) patterns were collected using a PANalytical X'Pert Pro diffractometer with Cu-filtered Kα radiation (λ = 0.154 nm). The data was collected in the 10–80° 2θ range.

with an angular step size of 0.026° and a counting time of 4 s per step. Ni and Co contents in the materials were determined *via* inductively coupled plasma-optical emission spectrometry (ICP-OES), using a Perkin Elmer Optima 4300 ICP-OES spectrometer. Scanning electron microscopy (SEM) images were performed on a field emission JEOL JEM 6700F working at 20 kV and equipped with INCA x-sight detector from Oxford Instruments for EDS analysis. Transmission electron microscopy (TEM) and high resolution (HRTEM) images of the nanoparticles were carried out on a field emission JEOL JEM2010F TEM microscope operating at 200 kV and equipped with a INCA x-sight detector from Oxford Instruments for EDS analysis. Samples for SEM, TEM and HRTEM analysis were prepared by dropping a diluted suspension of the powdered material onto holey carbon-coated copper grids. Samples of the used electrocatalysts were obtained by scratching the catalyst off the carbon paper with a utility knife. X-ray photoelectron (XPS) surface analysis was performed using a Thermo Scientific K-Alpha ESCA instrument equipped with Al-Kα monochromatized radiation at 1486.6 eV X-ray source. The samples were fixed on a double-side copper adhesive, which was mounted onto a sample plate and introduced intro the spectrometer. The XPS spectra were recorded in a Constant Analyser Energy mode with a 100 eV or 20 eV pass energy for survey spectra and high resolution spectra, respectively. The analysis was conducted at 5×10^{-7} Pa, with an electron take off angle of 90º. Due to the non-conductive nature of the samples, neutralization of the surface charge was performed by using both a low energy flood gun (electrons in the range 0 to 14 eV) and a low-energy Ar ion gun. All spectra were charge-referenced to the aliphatic C 1*s* component occurred at 284.8 eV. The atomic concentrations were determined from the XPS peak areas using the Shirley background subtraction technique and the Scofield sensitivity factors.

3.2.3 Electrodes Preparation

Two types of substrates were used to prepare the electrodes in this study: one was glassy carbon and the other was carbon paper. The glassy carbon electrode was prepared by adding

2 mg of the prepared catalysts to a mixture of 1 ml of isopropanol and 1 ml of distilled water and 15 µl of Nafion solution (5 wt%). The obtained suspension was sonicated for 30 min and then 15 µl of the well-suspended solution was drop-casted on the glassy carbon electrode (diameter = 3 mm). The electrode was dried at 80ºC for 25 min. For the preparation of the carbon paper electrodes, a catalyst ink was prepared by the ultrasonic dispersion of the catalyst (50 mg) in a mixture of water (5 cm^3), isopropanol (5 cm^3), and 50 µL Nafion solution (5 wt%) for 45 min. This dispersion was then painted by using an airbrush (Redoxme) onto the microporous layer of a gas diffusion layer (Sigracet 35BB, 8 cm^2 cross-sectional area), which had been mounted on a hot plate at 90°C. The final electrodes were produced by cutting the carbon paper electrode to four pieces of 2 cm^2 (effective electrode cross-sectional area = 1 cm^2) and attaching them to a tungsten wire using Kapton tape to secure the electrical connection.

3.2.4 Electrochemical tests

Electrochemical tests were performed by using an AUTO LAB PGSTAT 204 potentiostat at room temperature. The electrochemical cell was filled with 25 mL of a 1 M KOH solution prepared with Milli-Q water. A Pt wire spiral and an Ag/AgCl (3.0 M KCl) were used as the counter and reference electrode, respectively. Either the glassy carbon or the carbon paper electrodes were using as working electrode. Cyclic voltammetry and chronoamperometry were applied to study the activity and stability of the electrocatalysts. All potentials reported in this work are referenced to the RHE. The liquid product from the methanol electrochemical oxidation was characterized by ionic chromatography. To test a sample using ion chromatography (IC), begin with sample preparation by filtering it through a 0.2 or 0.45 µm filter to remove particulate matter. To analyze a sample using ion chromatography with the Chromeleon 7.2 Dionex software, was achieved by preparing the samples through filtration and dilution as mentioned, ensuring it is free from particulates and within the detectable concentration range. Then the system was calibrated by preparing standard solutions of the ions of interest and running these standards to generate a calibration curve. Set up the ion chromatography system by selecting the appropriate ion exchange column and preparing the eluent, typically an aqueous solution of a weak acid, base, or salt. Prime the system with the eluent, ensuring all air bubbles are removed. Using Chromeleon 7.2, configure the sequence by inputting the details of the standards and sample injections. As the sample passes through the column, ions are separated based on their interaction with the stationary phase and detected, usually by a conductivity or UV/VIS detector. Chromeleon 7.2 will generate a chromatogram, displaying the ion concentrations over time identifying the existed ions in the samples by comparing them with the retention times of the chromatogram peaks with those of the standards. Quantify the ions using the calibration curve to correlate peak areas or heights with concentrations.

Gas products were analyzed using an Agilent 7820A gas chromatograph equipped with both Flame Ionization Detector (FID) and Thermal Conductivity Detector (TCD), utilizing HP-PLOT Q and HP-MOLSIEVE columns, with argon (Ar) as the carrier gas. The HP-PLOT Q column is ideal for separating volatile organic compounds and permanent gases, while the HP-MOLSIEVE column is specialized for separating permanent gases and light hydrocarbons. During the analysis, the sample gas is injected into the chromatograph where it is carried by argon through the columns. Each component of the sample is separated based on its interaction with the stationary phase within the columns. The separated components are then detected sequentially by the FID and TCD detectors. The FID is highly sensitive to hydrocarbons, allowing for the precise quantification of organic compounds, whereas the TCD is a universal detector suitable for detecting all components of the gas mixture, particularly permanent gases. The combined use of these detectors, along with the specific column choices, enables comprehensive analysis of complex gas mixtures, providing detailed compositional data crucial for various applications in chemical analysis and quality control.

3.3 Results and discussion

ICP-OES results demonstrate that the actual molar ratio of the samples, *i.e.*, 1.1, 2, and 3.2 for the CoNi 1:1, CoNi 2:1, and CoNi 3:1, respectively, agreed with the nominal values. **Figure 3.1,** illustrates the X-ray diffraction patterns of the synthesized, CoNi 1:1, CoNi 2:1, and CoNi 3:1. CoNi 3:1 exhibits the characteristic diffraction peaks of the $NiCo_2O_4$ crystalline phase (JCPDS 20-0781) [22]. These peaks are slightly shifted to lower angles for the CoNi 1:1 and CoNi 2:1 samples, which indicates that both $NiCo_2O_4$ and NiO (JCPDS 47-1049) phases exist together. Theoretically, CoNi 2:1 should form 100 wt.% $NiCo_2O_4$ although the presence of NiO is confirmed from the XRD analysis. The amount of NiO increases for the CoNi 1:1 sample based on the increased shift towards lower angles. However, in the case of the $NiCo_2O_4$ phase, it is quite difficult to differentiate from the Co_3O_4 phase as both have the same spinel structure with minor differences in the lattice parameter [23]. Thus, in depth investigation of the lattice parameter of these samples is important to confirm the presence of $NiCo_2O_4$ phase. The crystalline size calculated from the Scherrer equation varies from 11.6 nm for the CoNi 1:1 sample to 17 and 10.9 nm for the CoNi 3:1 and CoNi 2:1 samples, respectively.

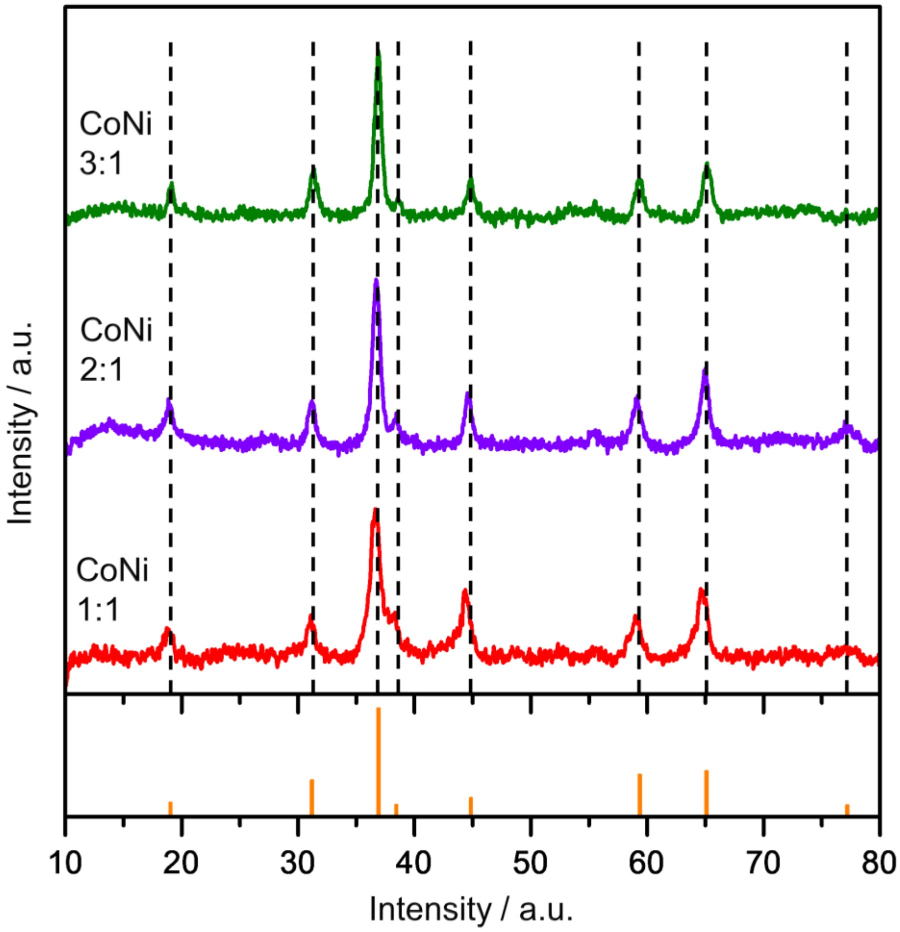

Fig.3.1 XRD of CoNi 1:1, CoNi 2:1 and CoNi 3:1

The morphology of the samples was observed using field emission scanning electron microscope analysis. Figure 3.2(a-c) shows FE-SEM images of CoNi 1:1, CoNi 3:1, and CoNi 2:1. It is clearly seen that the cobalt-nickel mixed oxide has sheet like structure in all the cases, which are greatly useful for electrochemical devices as sheet-like structure reduce the mass transport resistance faced in other microporous/mesoporous materials and permit flexible access of the electrolyte to the active surface sites [24]. The 3D mechanism formation in cobalt-nickel mixed oxides happens as a result of the thermally driven contraction process during the precursor thermal decomposition with the emission of carbon dioxide and water [25]. The EDX spectrum exhibit signals corresponding to Ni, Co, and O. All the synthesized materials were slightly oxygen-enriched. The carbon signal is attributed to the carbon matrix used to prepare the catalyst before measurement

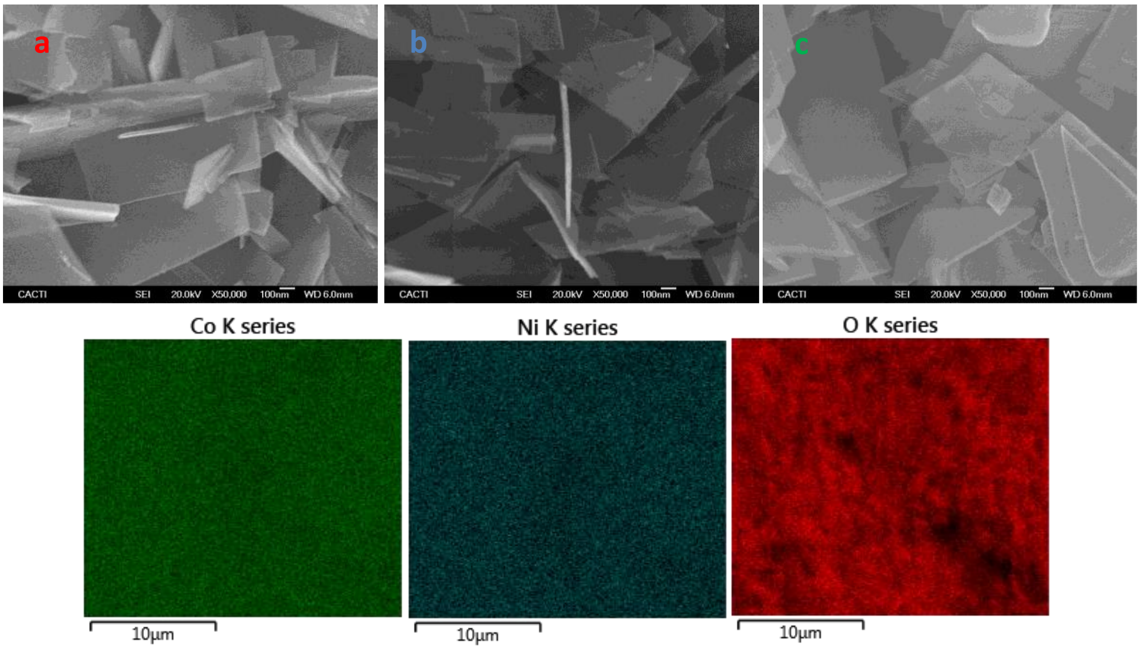

Fig.3.2 FE-SEM images of a- CoNi 1:1 b- CoNi 2:1 and c- CoNi 3:1, with , Element-mapping images of CoNi 2:1 nanosheets Co, Ni, and O.

TEM images for CoNi 1:1, CoNi 3:1, and CoNi 2:1 nanoparticles are illustrated in Fig. 3.3. Cobalt-nickel mixed oxide nanoparticles synthesized under controlled pressure and temperature conditions exhibit a spherical structure. These morphologies are consistent with those reported in the literature and are corroborated by images obtained from Field Emission Scanning Electron Microscopy (FE-SEM) [31]. The particle-size distribution histogram of the prepared powders (size range for the width of particles for a count of over 100 particles), has been obtained and shown in figure 3.3. The estimated average particle diameters were found to be 9.35, 9.4, and 9.31 nm for CoNi (1:1, 3:1, and 2:1), respectively.

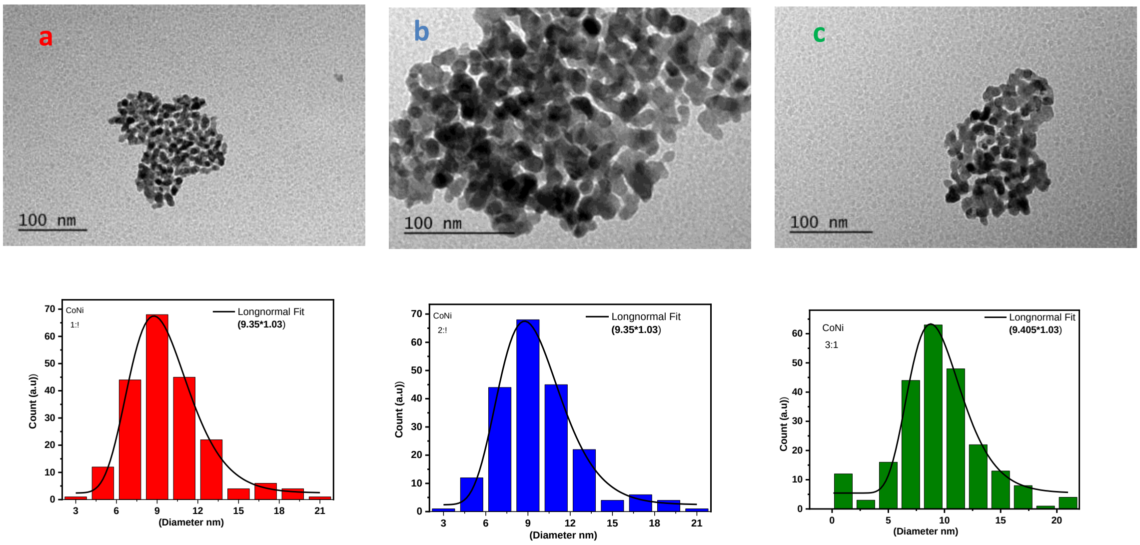

Fig.3.3 TEM images of a- CoNi 1:1 b- CoNi 2:1 and c- CoNi 3:1, with its respective particle size distribution histogram deposited

HR-TEM images of the CoNi 2:1 sample are compiled in Figure 3.4. The micrographs reveal the occurrence of quasi-spherical cobalt-nickel mixed oxide nanoparticles. The lattice spacing is 0.47 nm and 0.25 nm, which is in good agreement with the d-spacing associated with the (111) and (311) planes of the cubic $NiCo_2O_4$. However, The lattice spacing is 0.47 nm was used to express the presence of the cubic $NiCo_2O_4$ nanoparticles but also Nickel Oxide (NiO) could has the same value under certain condones of temperature and other experimental factors. NiO is typically crystallizes in a face-centered cubic (fcc) structure, specifically adopting the rock salt (NaCl) configuration. The lattice constant (a), representing the distance between two adjacent atoms in the crystal lattice, has been extensively documented in the literature. According to various sources, the lattice constant of NiO is approximately 0.47 nm [26].

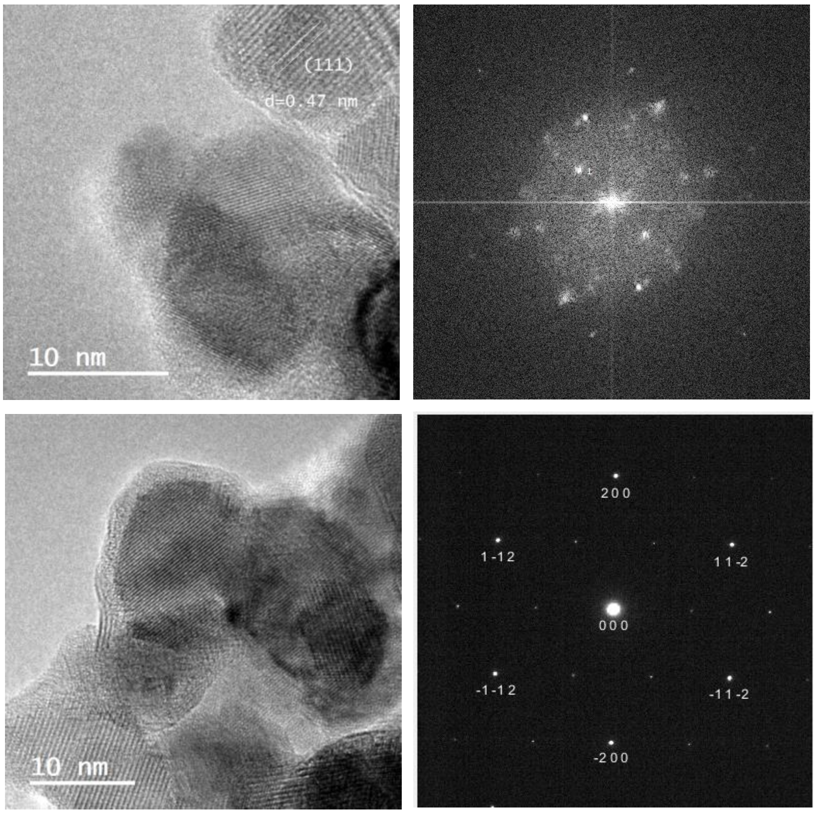

Fig.3.4 HR-TEM images of of CoNi 2:1

For a better understanding of the reduction-oxidation mechanism and the performance rate, cyclic voltammetry (CV) analysis was followed up. Figure 3.5a shows the electrochemical activity of CoNi 1:1, CoNi 3:1, and CoNi 2:1 nanoparticles over a glassy carbon (GC) modified electrode. All the prepared materials were tested in 1.0 M KOH solution at a scan rate of 50 mV/s and room temperature in the potential range between 0.9 and 1.7 V (vs. RHE). The glassy carbon electrode (GC) was tested alone before each experiment at different scan rate range from10 to100 mV/s to be sure there are no interfering peaks. All the recorded CV shows an ideal rectangular shape at all the recorded scan rates which ensure the pseudo-capacitive characteristics of Faradaic reactions. As a result of $Ni^{+2/}Ni^{+3}$ and Co^{+2}/Co^{+3} ions combination, During the forward scan, a first current density peak was observed at around 1.373, 1.370, 1.458, and 1.460 V for NiSe2 and Ni1−xFexSe2(x=

0.25, 0.5, 0.75) electrodes, respectively. This peak is commonly observed in Ni-based electrocatalyst in alkaline solution and it is attributed to the oxidation of surface $Ni(OH)_2$ to NiOOH. The controlled synthesis of cobalt-nickel mixed oxide nanoparticles under specific pressure and temperature conditions results in materials with spherical structures. These morphologies align with those reported in the literature and are verified by FE-SEM images. The electrochemical testing in 1.0 M KOH reveals characteristic pseudo-capacitive behavior and identifiable oxidation peaks, confirming the presence and activity of $Ni(OH)_2$ in the electrodes [27]. Also, The transformation from NiO to $Ni(OH)_2$ typically occurs through electrochemical oxidation in the presence of an electrolyte such as KOH. When NiO nanoparticles are subjected to an electrochemical environment, such as during the electrochemical testing in 1.0 M KOH that mentioned, they undergo a redox reaction. In this case, during the electrochemical testing, the NiO nanoparticles can react with the hydroxide ions (OH^-) from the KOH electrolyte to form $Ni(OH)_2$. This process involves the reduction of NiO to $Ni(OH)_2$, which is a characteristic reaction in alkaline solutions [28]. By increasing the potential up to 1.55 V usually is associated with a dramatic current rise due to O_2 production. The reduction peak appears around 1.31 V happens during the backward scan attributed to $Ni^{3+} \rightarrow Ni^{2+}$ reduction. Cobalt likely undergoes similar redox reactions to nickel but may exhibit distinct electrochemical behavior In mixed oxide nanoparticles containing cobalt and nickel, cobalt may contribute to the overall electrochemical activity, potentially forming $Co(OH)_2$ through similar redox reactions. The specific electrochemical behavior of cobalt would depend on factors such as its oxidation state, surface area, and interactions with the electrolyte. With changing the Ni to Co ratio, the current density of the redox peaks decreased owing to the reduction of the amount of Ni undergoing the redox reaction. No redox peaks were obtained with the CoNi 3:1 nanoparticles electrode in the potential range studied. The absence of redox peaks in the CoNi 3:1 (cobalt-nickel oxide) electrode can be attributed to several key factors. Firstly, at this specific cobalt-to-nickel ratio, the electrochemical activity may fall below the threshold necessary for observable redox peaks due to a reduced concentration of nickel, which typically drives redox activity in mixed oxide systems. Secondly, variations in electrode composition, with higher cobalt content in the CoNi 3:1 ratio, might enhance stability but diminish redox activity, leading to the absence of well-defined peaks. Additionally, nuances in electrodeposition dynamics could result in a unique microstructure affecting electrochemical behavior. Lastly, the predominance of cobalt species on the electrode surface at the CoNi 3:1 ratio might mask redox peaks associated with nickel. Further systematic investigation into CoNi electrodes across varying compositions is necessary to unravel these complexities and design them for diverse electrochemical applications [29]. CoNi shows a highly strong broadened characteristic oxidation and reduction peaks which are clearly seen in all tested materials [36]. The continuous flow contribution coming from both $Ni^{+2/}Ni^{+3}$ and Co^{+2}/Co^{+3} ions reduction-oxidation reactions produce electron-rich reactions with two electro-active centres which enabled them to be widely applied in many fields [47,48].These result is in a good agreement with that data obtained from the redox reactions in alkaline solution of CoNi modified electrodes which are illustrated by many researchers [49]. It is observed that by changing the stoichiometry ratio between Ni and Co, a slight positive and negative shift happened in the anodic and cathodic peaks due to the individual electronic differences in the transition of $Ni^{+2/}Ni^{+3}$ and Co^{+2}/Co^{+3} ions or the combined effect of transition states which are greatly affected by the particles crystallinity [54,55]. As well as there are no characteristic oxidation-reduction peaks in the case of CoNi 3:1 modified glassy carbon electrodes (GC) which can be attributed to the lack of electrocatalytic reduction of oxygen by the NCO sheet catalysts as mentioned above [29, 30]. The higher electro-catalytic activity of CoNi 2:1 over the other electrodes may be attributed to the higher tendency to form porous structures once they are immersed in the alkaline solution due to the dual-action coming from Ni and Co which has a huge influence on the electrochemical activity [53]. All the materials were tested in 1.0 M KOH solution at a scan rate range of 10 to 100 mV/s at room temperature in the potential range between 0.9 and 1.7 V (vs. RHE).

Figure 3.5b indicates the electro-catalytic activity of the prepared CoNi 1:1, CoNi 3:1, and CoNi 2:1, modified glassy carbon electrodes towards methanol electro-oxidation using the CV way in a potential range of (0.9 and 1.7) V/ vs RHE after subtracting the current density delivered in 1 m KOH. The characteristic redox peaks of $Ni^{+2/}Ni^{+3}$ and Co^{+2}/Co^{+3} ions are disappeared and only one broad peak related to methanol oxidation started to appear around 1.1 V (vs.RHE). It is seen that CoNi 2:1 has a higher current density value over the other electrodes with a negative shift reveals its higher electrocatalytic activity for MOH electro-oxidation. Catalytic current density value is a measure of the electro-catalytic efficiency, at which CoNi 2:1 record the highest current density value recorded up till now (290 mA/cm^2) at 50 mV/s and 2 M of MOH [5, 31-33]. And these results are in a line with the others obtained in the case of the experiments done in the absence of MOH. This result indicates that the3D macroporous structure is responsible for its high reactivity. All the catalysts contain Ni, and the methanol reaction mechanism is considered to be governed by a direct chemical reaction with NiOOH, which acts as a reagent. Fleischmann et al, indicates the electrochemical reactions occurs through surface $Ni(OH)_2$ oxidation to NiOOH, methanol adsorption, the hydrogen abstraction reaction, and the subsequent oxidation of the adsorbed intermediate [34-36]. All The shift of the peak potential is attributed to an electrochemical polarization and the limited reaction kinetics that control the formation of NiOOH species [37].

Figure 3.5c clarifies the methanol concentration effect on the electro-catalytic current intensity, which increased with the methanol concentration, until 3 M. It is well known that the anodic current oxidation peak of MOH is directly proportional to the square root of the scan rate (r^2 = 0.9962) [56]. It can be observed that the current response of CoNi 1:1, CoNi 3:1, and CoNi 2:1, modified glassy carbon electrodes for the addition of methanol is small compared with CoNi 2:1. This inability is indicative of the poor electro-catalytic activity of these modified electrodes toward methanol. Also, this may be reviled to the low efficiency of the electrodeposited, crystallinity difference.

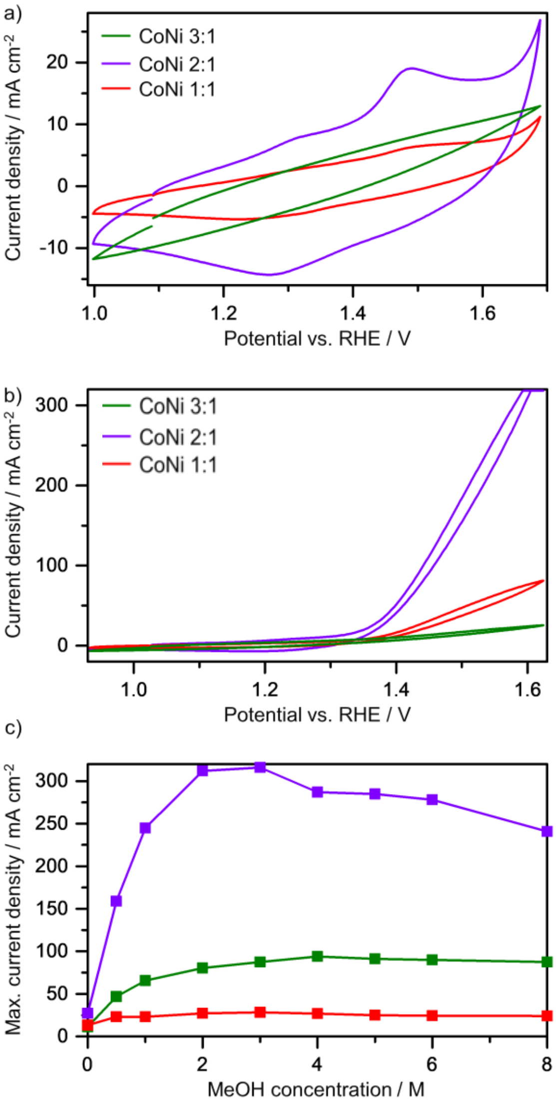

Fig.3.5 Cyclic voltammograms of CoNi 1:1, CoNi 2:1 and CoNi 3:1.

The synthesized electrodes stability was studied in 2 M of methanol, 1 M of KOH, and at a relatively stable potential, in the range 1.45–1.47 V, in order to maintain a stable current during the measurements as indicated in figure 3.6a. The result showed that the methanol oxidation current demonstrates higher stability for up to 33 h, ensuring the higher stability of the prepared electrodes which makes them industrially favorable. With increasing the reaction time up to 45 h, the current density decay slowly which is related to the appearance of new phases examined by XRD, XPS as will be discussed later. For other provident 1000 cyclic voltammetry which considered being the main drop method for many catalysts, were conducted and used to confirm the higher stability of the prepared electrodes as shown in figure 3.6b. The current density at 1.65 V retained 100 %, of the initial value after 200, 400, 600, 800, and 1000 cycles, respectively, which confirm the highest activity and stability of CoNi 2:1 recorded up till now. This electrode demonstrates the role to efficiently produce value-added formate from methanol with high selectivity in an eco-friendly way. This electrode illustrates the role of an efficient way to produce highly valuable formate from methanol with high selectivity in an environmentally friendly manner as discussed in the next section. The production of formate from methanol using a cobalt (Co) catalyst in an electrochemical process can achieve high selectivity and efficiency when optimized. However, increasing the amount of Co beyond an optimal level decreases efficiency as in case of CoNi 3:1 due to several factors such as electronic effects: overloading Co alters the catalyst's electronic properties, negatively affecting reaction pathways and selectivity. Also, for stability Issues: excess Co can cause structural instability and changes in oxidation states, degrading the catalyst's performance [38, 39].

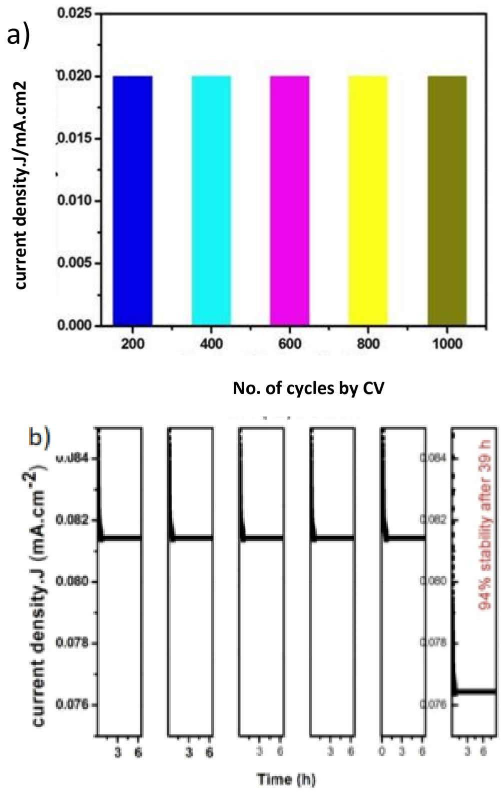

Fig.3.6 CoNi 2:1 sprayed over carbon paper in 2 M of MOH, 1 M of KOH and a fixed potential of 1.65 used to express the stability by using a) CV for 1000 cycle and b) Chronoamperograms for a period of 40h.

As displayed in the inset in Figure 3.7, at which clearly seen that the formate concentration increased in all cases with the CP time, i.e., with the total amount of charge flown. Also, the formate concentration is higher in the case of CoNi 2:1 than the other prepared catalysts which clarify its highest catalytic activity as discussed before see table 1. The reaction pathway and the active species that control the rate methanol oxidation process have been followed up. Methanol oxidation reaction happens through a dual-pathway that involves either CO or formate intermediates. It is well known that formate weak bonds to the catalyst surface and are easily dissolved in alkaline media. Many researchers claimed that CO is that which blocks the active sites and causes catalysis toxicity.

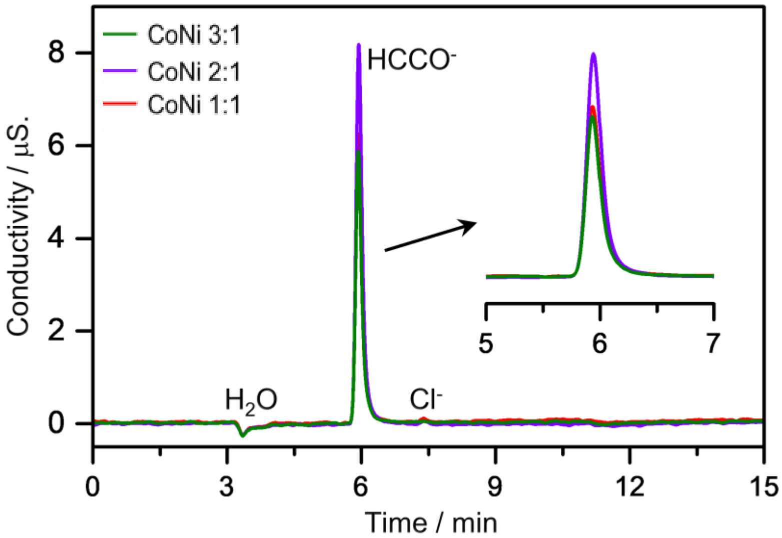

Fig.3.7 IC profile in 1 M KOH containing 2 M methanol during 10 000 s CP testing obtained at 2000 s intervals of CoNi 1:1, CoNi 2:1 and CoNi 3:1.

Samples CoNi	Formate Conc g/L	µg/h.mg cat	µ.mol/h.mg cat
1:1	1.33	900	21.28
2:1	1.75	1260	28
3:1	1.25	957.6	20

Table.1. Formate yield obtained from IC measurements in 1 M KOH containing 2 M methanol during 10 000 s CP testing obtained at 2000 s intervals.

Figure 3.8, shows the cyclic voltammetry (CV) of CoNi 2:1, before and after exposure to the catalytic process tested at the same experimental conditions in 1 M KOH and 50 V scan rate. It is clearly seen that the ideal rectangular shape characteristics of CoNi 2:1and the peaks related to $Ni^{+2/}Ni^{+3}$ and Co^{+2}/Co^{+3} ions combination have been reduced greatly after 40 h from the reaction which may be because of that new phases formed at the surface of the catalyst. For this purpose, the CoNi 2:1 catalyst has been tested using the XRD technique. The phase composition and structure of the CoNi before and after catalytic exposure were examined by powder X-ray diffraction (XRD). As shown in Figure 3.9, it is clearly seen that for the CoNi 2:1 obtained directly from the hydrothermal process, all diffraction peaks can be assigned to which indicates that both $NiCo_2O_4$ and NiO phases exist together as mentioned previously. After 40 h catalytic reaction, the Ni-Co precursor interacted with the reaction solution. Li et al. record that the peak at 25° occurs due to the anodic materials stacked carbon, derived from the incomplete decomposition of organic ingredients [40-42]. While the peak around 35º can be related to the presence of $Ni_{1-x}Co_x(OH)_2$ [43].

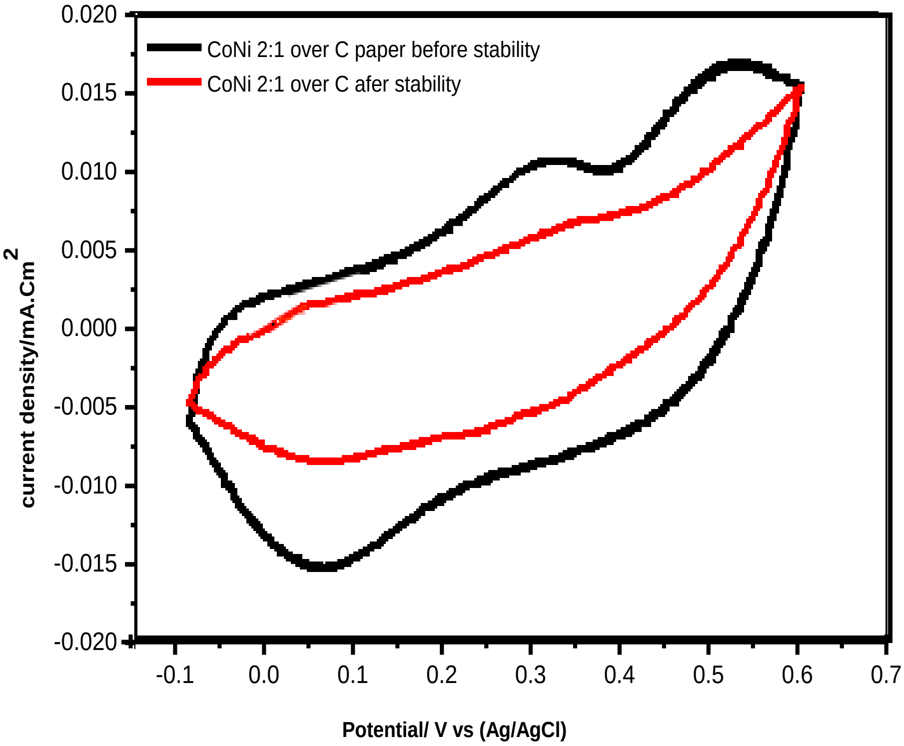

Fig.3.8 CV of fresh sample of CoNi 2:1, in 1.0 M KOH solution at scan rate of 50 mV/s, and after 40 h of Chronoamperograms stabilitytest.

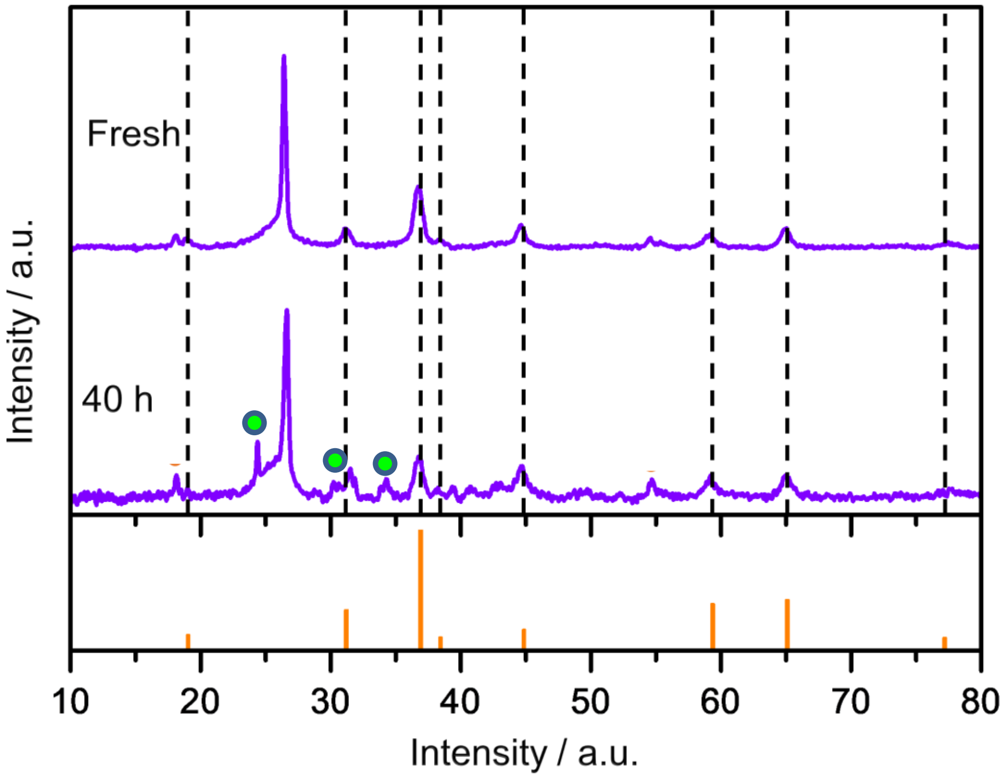

Fig.3.9 XRD patteren of CoNi 2:1 fresh sample and after 40 h of Chronoamperograms stability test.

STEM images with the energy dispersive X-ray spectroscopy (EDX) was conducted. Co, Ni, K, and O elements were detected for that sample exposed to 40 h of Chronoamperograms stabilitytest as indicated in Figure 3.10, and the contents of K were determined which also confirm the perovskite phase. The morphologies of the prepared CoNi 2:1 sample were examined by HR-TEM. A clearly seen sheets-like structure with lattice spacing is 0.47 nm and 0.25 nm, which is in good agreement with the d-spacing associated with the (111) and (311) planes of the cubic $NiCo_2O_4$. However, the lattice spacing is 0.47 nm was used to express the presence of quasi-spherical cobalt-nickel mixed oxide before and after catalytic exposure figure 3.11.

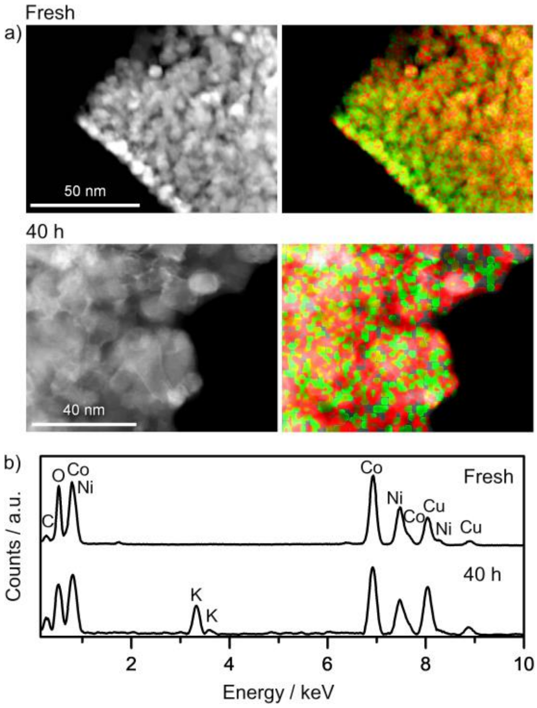

Fig.3.10 STEM images of CoNi 2:1 fresh sample and after 40 h of Chronoamperograms stability test.

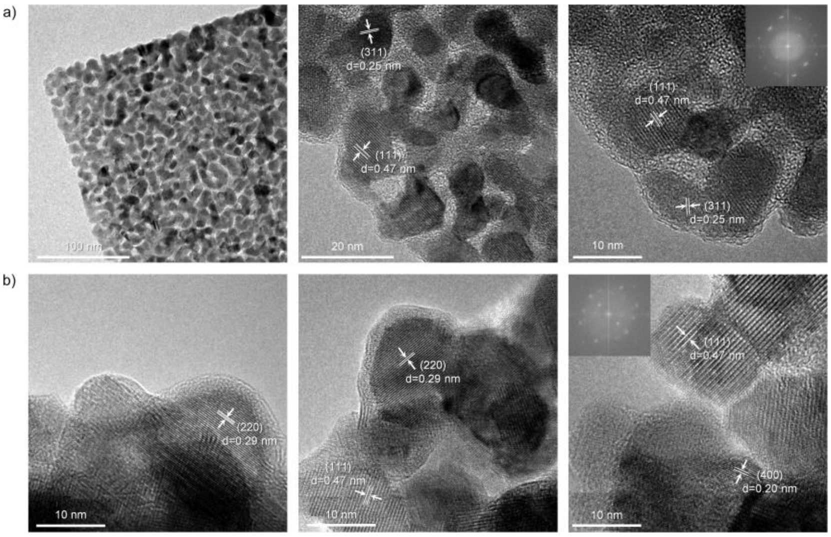

Fig.3.11 HR.TEM images of CoNi 2:1 fresh sample and after 40 h of Chronoamperograms stability test.

The surface chemistry of CoNi 2:1 powder, sprayed over carbon paper after 40 h catalytic reaction was checked by using X-ray photoelectron spectroscopy (XPS) measurements. Figure 3.12 shows the Co $2p_{3/2}$ and Ni $2p_{3/2}$ XPS spectra recorded, indicating that Ni^{3+}, 'and Ni^{2}, $Co^{3+}$and Co^{2+}, were found in the $NiCo_2O_4$ samples [44, 45]. Moreover, based on the calculating results, the ratio of $Co^{3+}$to $Co^{2+}$of CoNi 2:1 powder and deposited over carbon paper was found to be only 1.4 on its surface, which is close enough to its stoichiometric ratio of 2:1. While that of the films after undergoing 40 h catalytic reaction the ratio decreased till 0.94 which may be attributed to the instability of Co^{3+} on the surface. It is well known that trivalent species in the spinel metal oxides are considered to be the active sites for catalytic reactions and Ni substitution improves the stability of Co^{3+} on the surface [46]. Therefore, the excellent electrocatalytic activity of 3D macroporous CoNi 2:1 sheets attributed to the much greater number of active sites on their surface, and these active sites after 33 h started to be blocked by the new phases formed as discussed previously in the XRD portion. Also, it is clearly seen the potassium peaks which is increasing with reaction time confirming the formation of the perovskite phase. It is clearly seen that the spectra of the prepared catalysts were matched with the following cases. First, the line located at binding energy (BE) 854.483 eV and FWHM equal to 4.47 eV, confirm the presence of Ni^{+2} which is centered in the octahedral position of the spinel structure. Second, the line at BE equal to 856.6 eV, confirms Ni^{+3} presences [47-49]. Moreover, at BE of 862 eV (FWHM"6.0 eV) related to Ni^{+2} and Ni^{+3} which clearly seen as a broad peak. For Co2p spectra obtained was found that the peaks were matched with the peaks of Co_3O_4 with different components due to the presence of Co^{+2} and Co^{+3} [49, 50]. The O 1s spectra recorded contain related to different types of O_2 which are fingered out as O (1-4). Firstly, the O1 peak located at 529.2 eV, refers to the M-O bonds (where M refers to metal). In conclusion [51]

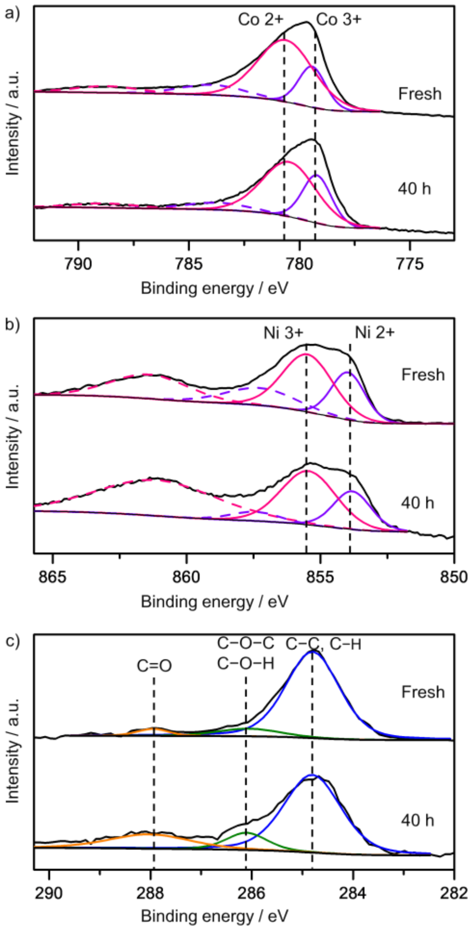

Fig.3.12 XPS patteren of CoNi 2:1 fresh sample and after 40 h of Chronoamperograms stability test.

To clarify the catalytic gap between CoNi 2:1 and other catalysts used to produce formate, CO stripping voltammetry has been used [52]. In this technique, CO is first adsorbed on the material surface at a favorable potential (1.65 V vs RHE) by allowing the CO gas to be bubbled inside the reaction chamber. Therefore, the oxidation of adsorbed CO is followed up during a linear sweep voltammetry figure 3.13. The reacting surface area and the strength of CO–metal interaction strength can be detected depending upon the magnitude and position of the CO oxidation peak. Peak measurement around 0.56 V vs RHE ascribes the oxidation of CO ($CO \rightarrow CO_2$) [53]. It is well known that catalysts with the largest active sites adsorb a higher amount of Co and show a higher oxidation peak as in the case of CoNi 2:1.

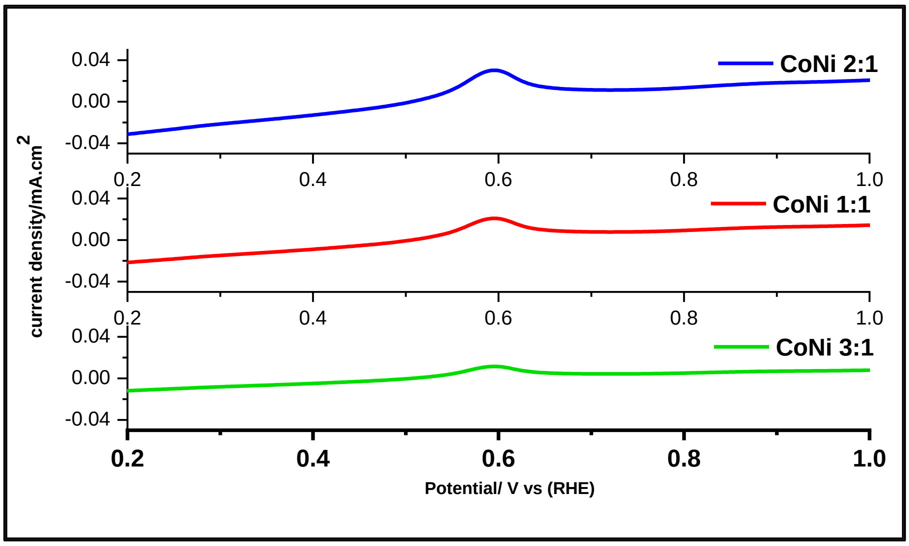

Fig.3.13 CO stripping voltammetry at applied potential of 1.65 V RHE.

3.4 Conclusion

In this study, the hydrothermal synthesis of nickel cobaltite ($NiCo_2O_4$) nanosheets was systematically explored by varying reaction temperatures, surfactant types, and Ni stoichiometric ratios (1:1, 2:1, and 3:1). This approach successfully yielded both pure nickel cobaltite phases and mixed phases with nickel oxide. The synthesized nanoparticles exhibited nearly 100% electrochemical conversion of methanol to formate under standard conditions, demonstrating their high efficiency. The CoNi (2:1) composition, when used as an anode for methanol electrocatalytic oxidation, achieved the highest current density reported to date 290 mA/cm^2 at 1.65 V (vs. RHE) in a solution of 1 M KOH and 2 M methanol. This material also demonstrated exceptional stability, maintaining 100% of its initial anodic current density for 33 hours, thereby surpassing the performance of current state-of-the-art catalysts for this reaction. Electrochemical studies using cyclic voltammetry (CV) confirmed the superior performance of CoNi (2:1) nanoparticles over other ratios (1:1 and 3:1) when applied to a modified glassy carbon (GC) electrode. The CV profiles showed an ideal rectangular shape, indicating pseudo-capacitive characteristics associated with Faradaic reactions. Among the tested materials, CoNi (2:1) exhibited the highest current density and a significant negative shift, highlighting its enhanced electrocatalytic activity for methanol oxidation. Additional cyclic voltammetry tests, involving up to 1000 cycles, confirmed the superior stability of the prepared electrodes, positioning them as reliable candidates for long-term applications. X-ray diffraction (XRD) analysis post-reaction revealed interactions between the Ni-Co precursor and the reaction solution, with peaks around 25° and 35° indicating the presence of stacked carbon from incomplete decomposition and $Ni_{1-x}Co_x(OH)_2$ phases, respectively. CO stripping voltammetry corroborated these findings, demonstrating that catalysts with larger active sites, such as CoNi (2:1), adsorb more Co and exhibit higher oxidation peaks. Overall, this study highlights the significant potential of CoNi (2:1) nanosheets as efficient and stable electrocatalysts for methanol oxidation, paving the way for advancements in energy conversion technologies.

3.5 References

1. Omer, A.M., *Energy, environment and sustainable development.* Renewable and sustainable energy reviews, 2008. **12**(9): p. 2265-2300.
2. Adschiri, T., et al., *Hydrothermal synthesis of metal oxide nanoparticles at supercritical conditions.* Journal of Nanoparticle Research, 2001. **3**(2): p. 227-235.
3. Kakati, N., et al., *Anode catalysts for direct methanol fuel cells in acidic media: do we have any alternative for Pt or Pt–Ru?* Chemical reviews, 2014. **114**(24): p. 12397-12429.
4. Badwal, S., et al., *Direct ethanol fuel cells for transport and stationary applications–A comprehensive review.* Applied Energy, 2015. **145**: p. 80-103.
5. Li, J., et al., *Selective methanol-to-formate electrocatalytic conversion on branched nickel carbide.* Angewandte Chemie, 2020. **132**(47): p. 21012-21016.
6. Herrero, E., W. Chrzanowski, and A. Wieckowski, *Dual path mechanism in methanol electrooxidation on a platinum electrode.* The Journal of Physical Chemistry, 1995. **99**(25): p. 10423-10424.
7. Palacio, I., J.M. Rojo, and O. Rodriguez de la Fuente, *Surface defects activating new reaction paths: formation of formate during methanol oxidation on Ru (0001).* ChemPhysChem, 2012. **13**(9): p. 2354-2360.

8. Pieta, I.S., et al., *Electrocatalytic methanol oxidation over Cu, Ni and bimetallic Cu-Ni nanoparticles supported on graphitic carbon nitride.* Applied Catalysis B: Environmental, 2019. **244**: p. 272-283.
9. Hao, J., et al., *In situ facile fabrication of Ni (OH) 2 nanosheet arrays for electrocatalytic co-production of formate and hydrogen from methanol in alkaline solution.* Applied Catalysis B: Environmental, 2021. **281**: p. 119510.
10. Dong, B., et al., *Fabrication of hierarchical hollow Mn doped Ni (OH) 2 nanostructures with enhanced catalytic activity towards electrochemical oxidation of methanol.* Nano Energy, 2019. **55**: p. 37-41.
11. Liu, Q., et al., *Towards a sustainable synthesis of formate salts: Combined catalytic methanol dehydrogenation and bicarbonate hydrogenation.* Angewandte Chemie International Edition, 2014. **53**(27): p. 7085-7088.
12. Eppinger, J. and K.-W. Huang, *Formic acid as a hydrogen energy carrier.* ACS Energy Letters, 2017. **2**(1): p. 188-195.
13. Li, J., et al., *Nickel iron diselenide for highly efficient and selective electrocatalytic conversion of methanol to formate.* Small, 2021. **17**(6): p. 2006623.
14. Müller, K., K. Brooks, and T. Autrey, *Hydrogen storage in formic acid: a comparison of process options.* Energy & Fuels, 2017. **31**(11): p. 12603-12611.
15. Yi, Y., J. Li, and C. Cui, *Trimetallic FeCoNi disulfide nanosheets for CO2-emission-free methanol conversion.* Chinese Chemical Letters, 2022. **33**(2): p. 1006-1010.
16. Liu, B., et al., *Hierarchical trace copper incorporation activated cobalt layered double hydroxide as a highly selective methanol conversion electrocatalyst to realize energy-matched photovoltaic-electrocatalytic formate and hydrogen co-production.* Journal of Materials Chemistry A, 2022. **10**(37): p. 19649-19661.
17. Cheng, H., et al., *Concurrent H2 generation and formate production assisted by CO2 absorption in one electrolyzer.* Small Methods, 2021. **5**(11): p. 2100871.
18. Ma, G., et al., *Hydrogen production from methanol reforming electrolysis at NiO nanosheets supported Pt nanoparticles.* Chemical Engineering Journal, 2021. **411**: p. 128292.
19. Zhao, B., et al., *Interfacial engineering of Cu2Se/Co3Se4 multivalent hetero-nanocrystals for energy-efficient electrocatalytic co-generation of value-added chemicals and hydrogen.* Applied Catalysis B: Environmental, 2021. **285**: p. 119800.
20. Li, Y., P. Hasin, and Y. Wu, *Ni x Co 3− x O 4 nanowire arrays for electrocatalytic oxygen evolution.* Advanced materials, 2010. **17**(22): p. 1926-1929.
21. Liu, S., et al., *Nickel cobaltite nanostructures for photoelectric and catalytic applications.* Small, 2015. **11**(34): p. 4267-4283.
22. Ding, R., et al., *Hydrothermal and soft-templating synthesis of mesoporous NiCo 2 O 4 nanomaterials for high-performance electrochemical capacitors.* Journal of Applied Electrochemistry, 2013. **43**: p. 903-910.
23. Lim, T.H., et al., *Effect of Co/Ni ratios in cobalt nickel mixed oxide catalysts on methane combustion.* Applied Catalysis A: General, 2015. **505**: p. 62-69.
24. Chang, H., S.H. Joo, and C. Pak, *Synthesis and characterization of mesoporous carbon for fuel cell applications.* Journal of Materials Chemistry, 2007. **17**(30): p. 3078-3088.
25. Wen, Z., J. Liu, and J. Li, *Core/shell Pt/C nanoparticles embedded in mesoporous carbon as a methanol-tolerant cathode catalyst in direct methanol fuel cells.* Advanced materials, 2008. **20**(4): p. 743-747.
26. Bernal-Salamanca, M., et al., *Formation of Nickel Oxide Nanocuboids in Ferromagnetic La2Ni1− xMn1+ xO6.* Nanomaterials, 2021. **11**(3): p. 804.
27. MacArthur, D., *The hydrated nickel hydroxide electrode potential sweep experiments.* Journal of The Electrochemical Society, 1970. **117**(4): p. 422.

28. Mozaffari, S.A., S.H.M. Najafi, and Z. Norouzi, *Hierarchical NiO@ Ni (OH) 2 nanoarrays as high-performance supercapacitor electrode material.* Electrochimica Acta, 2021. **368**: p. 137633.
29. Zhang, Q., et al., *Bimetallic nickel-cobalt oxides: A comprehensive insight into Ni/Co ratio, intrinsic structure and electrochemical behaviors.* Vacuum, 2022. **196**: p. 110764.
30. Xiao, Y., et al., *Three-Dimensional Macroporous NiCo2O4 Sheets as a Non-Noble Catalyst for Efficient Oxygen Reduction Reactions.* Chemistry–A European Journal, 2013. **19**(42): p. 14271-14278.
31. Wang, W.-H., et al., *Design and synthesis of phenylphosphine oxide-based polymer photocatalysts for highly efficient visible-light-driven hydrogen evolution.* Sustainable Energy & Fuels, 2020. **4**(10): p. 5264-5270.
32. Li, J., et al., *Unraveling the role of iron on Ni-Fe alloy nanoparticles during the electrocatalytic ethanol-to-acetate process.* Nano Research, 2024. **17**(4): p. 2328-2336.
33. Xie, S., et al., *CNT–Ni/SiC hierarchical nanostructures: preparation and their application in electrocatalytic oxidation of methanol.* Journal of materials chemistry A, 2013. **1**(6): p. 2104-2109.
34. Takahashi, Y. and T. Tatsuma, *Oxidative Energy Storage Ability of a TiO2− Ni (OH) 2 Bilayer Photocatalyst.* Langmuir, 2005. **21**(26): p. 12357-12361.
35. Fleischmann, M., K. Korinek, and D. Pletcher, *The oxidation of organic compounds at a nickel anode in alkaline solution.* Journal of Electroanalytical Chemistry and Interfacial Electrochemistry, 1971. **31**(1): p. 39-49.
36. Park, K.-W., et al., *Chemical and electronic effects of Ni in Pt/Ni and Pt/Ru/Ni alloy nanoparticles in methanol electrooxidation.* The Journal of Physical Chemistry B, 2002. **106**(8): p. 1869-1877.
37. Chen, D. and S.D. Minteer, *Mechanistic study of nickel based catalysts for oxygen evolution and methanol oxidation in alkaline medium.* Journal of Power Sources, 2015. **284**: p. 27-37.
38. Spöri, C., et al., *The stability challenges of oxygen evolving catalysts: towards a common fundamental understanding and mitigation of catalyst degradation.* Angewandte Chemie International Edition, 2017. **56**(22): p. 5994-6021.
39. Li, M., et al., *Value-Added Formate Production from Selective Methanol Oxidation as Anodic Reaction to Enhance Electrochemical Hydrogen Cogeneration.* ChemSusChem, 2020. **13**(5): p. 914-921.
40. Li, J., et al., *Nonstoichiometric Cu0. 6Ni0. 4Co2O4 Nanowires as an Anode Material for High Performance Lithium Storage.* Nanomaterials, 2020. **10**(2): p. 191.
41. Chen, Y., et al., *Graphene improving lithium-ion battery performance by construction of NiCo2O4/graphene hybrid nanosheet arrays.* Nano Energy, 2014. **3**: p. 88-94.
42. Jurkiewicz, K., M. Pawlyta, and A. Burian, *Structure of carbon materials explored by local transmission electron microscopy and global powder diffraction probes.* C—Journal of Carbon Research, 2018. **4**(4): p. 68.
43. Li, Y. and X. Peng, *Shape-Controlled Synthesis of NiCo2O4 and Its Supercapacitive Performance.* ChemistrySelect, 2017. **2**(28): p. 8959-8964.
44. Lu, X., et al., *Controllable synthesis of porous nickel–cobalt oxide nanosheets for supercapacitors.* Journal of Materials Chemistry, 2012. **22**(26): p. 13357-13364.
45. Thissen, A., et al., *Photoelectron spectroscopic study of the reaction of Li and Na with NiCo2O4.* Chemistry of materials, 2005. **17**(20): p. 5202-5208.
46. Chen, H., et al., *Entropy-stabilized metal oxide solid solutions as CO oxidation catalysts with high-temperature stability.* Journal of Materials Chemistry A, 2018. **6**(24): p. 11129-11133.
47. Lenglet, M., et al., *Analysis of x-ray Ni Kβ emission, xanes, xps, Ni 2p, and optical spectra of nickel (II) spinels and structure inference.* Chemical physics letters, 1987. **136**(5): p. 478-482.

48. Lenglet, M., et al., *XANES, X-ray photo-electron and optical spectra of divalent nickel at the crystallographic transition in NiCr2O4 and the Ni1-xCuxCr2O4 system: correlation with the Jahn-Teller effect.* Journal of Physics C: Solid State Physics, 1986. **19**(17): p. L363.
49. McIntyre, N. and M. Cook, *X-ray photoelectron studies on some oxides and hydroxides of cobalt, nickel, and copper.* Analytical chemistry, 1975. **47**(13): p. 2208-2213.
50. Rios, E., et al., *Characterization of bulk and surface composition of polycrystalline Co3O4 synthesized at 400° C for electrocatalysis.* Boletin de la Sociedad Chilena de Quimica, 1998. **43**(4): p. 447-459.
51. Choudhury, T., et al., *Reduction of oxides of iron, cobalt, titanium and niobium by low-energy ion bombardment.* Journal of Physics D: Applied Physics, 1989. **22**(8): p. 1185.
52. Gisbert, R., G. García, and M.T. Koper, *Oxidation of carbon monoxide on poly-oriented and single-crystalline platinum electrodes over a wide range of pH.* Electrochimica acta, 2011. **56**(5): p. 2443-2449.
53. Hall, D.S., C. Bock, and B.R. MacDougall, *The electrochemistry of metallic nickel: oxides, hydroxides, hydrides and alkaline hydrogen evolution.* Journal of The Electrochemical Society, 2013. **160**(3): p. F235.

General conclusions

Although specific conclusions were provided at the end of each chapter, the most pertinent findings of the research detailed in this Doctoral Thesis are summarized as follows:

A sophisticated hierarchical layer-by-layer assembly protocol has been developed for creating advanced photocatalytic hybrid nanostructures as a result we could.

1- **Enhanced Photocatalytic Activity**: Strategic combination of PNP with CdS QDs has led to a significant enhancement in the photocatalytic activity of TiO2 NPs.

2- **The Importance of Near-Field Enhancement**: CdS QDs effectively utilize near-field enhancement, highlighting the crucial role of spectral overlap between plasmon and semiconductor for optimizing photocatalysis.

3- **Optimized Energy Transfer Mechanisms**: Focusing on near-field enhancement and bridging energy transfer from SiO_2-coated PNPs to TiO2 via indirect charge transfer initiated in the QDs results in the highest reaction rates.

4- **Challenges with PNPs**: Using PNPs for hot electron injection and near-field enhancement is less effective due to the negative impact of charge backtransfer to the metal.

5- **Optimal Deposition Sequences**: The sequence of photocatalyst element deposition is critical. Maximizing PNP surface coverage with CdS-QD@TiO_2-NP groups is essential to fully exploit the indirect activation mechanism.

6- **Exploration of Hybrid Mechanisms**: The study explored systems where near-field-initiated mechanisms coexist with hot carrier injection. It was found that while certain PNP geometries like AuNRs enhance hot carrier excitation rates, they are suboptimal due to electron back-transfer when using QDs as the photosensitizer.

7- **Interplay of Energy Transfer Mechanisms**: The research provides a detailed understanding of the interactions between different energy transfer mechanisms in hybrid plasmonic photocatalytic systems.

8- **Future Nanoengineering Studies**: The findings highlight the need for further detailed nanoengineering studies to optimize the contributions of each component in these hybrid systems.

9- **Path to Optimized Complexes**: These insights serve as a guide for synthesizing complexes that can effectively harness various energy transfer mechanisms, leading to improved photocatalytic performance.

The systematically of the hydrothermal synthesis of nickel cobaltite ($NiCo_2O_4$) nanoparticles by varying reaction temperatures, surfactant types, and Ni stoichiometric ratios (1:1, 2:1, and 3:1) led to the following facts.

1- **Pure and Mixed Phases**: This approach yielded both pure nickel cobaltite phases and mixed phases with nickel oxide.

2- **High Efficiency in Methanol Conversion**: The synthesized nanoparticles demonstrated nearly 100% electrochemical conversion of methanol to formate under standard conditions.

3- **Superior Electrocatalytic Performance**: The CoNi (2:1) composition achieved the highest current density reported to date for methanol electrocatalytic oxidation—290 mA/cm^2 at 0.65 V (vs. RHE) in a solution of 1 M KOH and 2 M methanol.

4- **Exceptional Stability**: The CoNi (2:1) anode maintained 100% of its initial anodic current density for 33 hours, surpassing the performance of current state-of-the-art catalysts.

5- **Cyclic Voltammetry Confirmation**: Electrochemical studies using cyclic voltammetry (CV) confirmed the superior performance of CoNi (2:1) nanoparticles over other ratios when applied to a modified glassy carbon (GC) electrode.

6- **Pseudo-Capacitive Characteristics**: CV profiles showed an ideal rectangular shape, indicating pseudo-capacitive characteristics associated with Faradaic reactions.

7- **Highest Current Density and Negative Shift**: Among the tested materials, CoNi (2:1) exhibited the highest current density and a significant negative shift, highlighting its enhanced electrocatalytic activity for methanol oxidation.

8- **High Stability Over Multiple Cycles**: Additional cyclic voltammetry tests up to 1000 cycles confirmed the high stability of the prepared electrodes, positioning them as reliable candidates for long-term applications.

9- **X-ray Diffraction Analysis**: XRD analysis post-reaction revealed interactions between the Ni-Co precursor and the reaction solution, indicating the presence of stacked carbon from incomplete decomposition and $Ni_{1-x}Co_x(OH)_2$ phases.

10- **CO Stripping Voltammetry**: CO stripping voltammetry demonstrated that catalysts with larger active sites, such as CoNi (2:1), adsorb more Co and exhibit higher oxidation peaks.

11- **Potential for Energy Conversion**: The study highlights the significant potential of CoNi (2:1) nanosheets as efficient and stable electrocatalysts for methanol oxidation, paving the way for advancements in energy conversion technologies

Resumen

Diseño de Nanomateriales Basados en Óxidos de Metales de Transición para Aplicaciones Ambientales

Esta tesis doctoral aborda la fabricación de nanopartículas (NPs) basadas en óxidos de metales de transición (TMO) y su utilización en aplicaciones ambientales relevantes, incluida la producción de energía renovable y el tratamiento del agua. Las partículas sintetizadas se clasifican en dos clases principales: nanoláminas de cobaltita de níquel (NiCo2O4) y nanopartículas de óxido mixto de cobalto-níquel con diferentes relaciones molares Ni
preparadas mediante síntesis hidrotérmica para la producción de formiato en pilas de combustible directo de metanol (DMFCs), y nanohíbridos de puntos cuánticos plasmónicos compuestos por puntos cuánticos de sulfuro de cadmio (CdS, QDs), dióxido de titanio (TiO2) y NPs de Au como bloques de construcción. La eficiencia de los materiales desarrollados para absorber más luz del espectro electromagnético (banda visible) se evaluó mediante actividad catalítica. Estos híbridos se implementaron para la degradación y eliminación de Rodamina B (RB); ofrecieron una actividad fotocatalítica superior en las regiones visibles e infrarrojas cercanas. Estos híbridos pueden encontrar amplias aplicaciones ambientales, especialmente en el tratamiento de aguas residuales.

Esquema de la Tesis

Este trabajo ha sido llevado a cabo en la Universidade de Vigo. Parte de los resultados incluidos aquí han sido obtenidos en colaboración con grupos externos que han contribuido con aportaciones complementarias que van desde modelización teórica hasta caracterización avanzada de los materiales sintetizados.

Esta disertación se ha estructurado en cuatro capítulos principales. El Capítulo 1 aborda un breve resumen sobre las características a escala nanométrica en ciencia de materiales, incluyendo una breve descripción de los métodos químicos que se han utilizado para sintetizar los nanomateriales reportados, y los protocolos de ensamblaje aplicados para fabricar los nanohíbridos. Se discuten diferentes protocolos sintéticos que incluyen enfoques coloidales, hidrotérmicos y capa por capa.

El Capítulo 2 presenta el desarrollo de un nanohíbrido de Au@CdS@TiO_2 mediante una técnica capa por capa con una alta capacidad para la captación de luz en el espectro electromagnético visible que puede suprimir la recombinación de carga, así como suministrar sitios reactivos para la fotocatálisis. El catalizador sintetizado se prueba en la degradación de Rodamina B como reacción modelo de tratamiento de aguas residuales. Es importante mencionar que este proceso de fabricación procedió con un estudio teórico para hipotetizar la estructura cristalográfica más adecuada para el nuevo sistema de catálisis, así como una predicción de las energías de interacción superficial entre el catalizador y el colorante RB que puede encontrarse en el flujo de aguas residuales.

El Capítulo 3 informa sobre nanoplacas de cobalto níquelato y nanopartículas de óxido mixto de cobalto-níquel como catalizadores para la oxidación de metanol a formato. El NiCo2O4 sintetizado muestra una conversión electroquímica de metanol a formato de casi el 100%, lo cual se racionalizó mediante un conjunto de técnicas de caracterización que incluyen XRD, SEM-EDS, HRTEM y ICP-OES.

El Capítulo 4 resume las conclusiones clave y las implicaciones de este trabajo en un contexto más amplio, e identifica los desafíos futuros y las direcciones de investigación.

1. Introducción general

La superpoblación mundial impone una presión significativa sobre los recursos energéticos ambientalmente sostenibles. Más recientemente, se ha prestado mucha atención a los recursos energéticos renovables, así como al tratamiento de la contaminación del agua. La ingeniería cuidadosa de materiales nanométricos avanzados ofrece características novedosas para enfrentar la futura demanda energética, incluido el diseño de células solares, supercondensadores o fotocatalizadores para producir combustibles sostenibles o reducir la contaminación del agua mediante la fotodegradación. La energía no renovable presenta grandes problemas representados en la limitación de la producción de energía y las contaminaciones adicionales como los gases fatales: COX, SOx y NOX; estos gases pueden causar problemas peligrosos para humanos, animales y todos los entornos.

Nanotecnología y Nanomateriales

La nanotecnología consiste en la manipulación de la materia a escala nanométrica, en dimensiones entre 1 y 100 nm, para producir nuevas estructuras, materiales y dispositivos. Feynman destacó en su clásica conferencia científica titulada "Hay mucho espacio en el fondo" las principales diferencias en las propiedades de los materiales a escala macroscópica y nanoscópica. Mientras que los materiales a granel presentan propiedades físicas constantes independientemente de su tamaño, las leyes de la física cuántica, en lugar de la física clásica, comienzan a controlar el rendimiento del material y su comportamiento a escala nanométrica. Por ejemplo, compuestos metálicos como el cobre, que son opacos a escala macroscópica, se vuelven transparentes a escala nanométrica; el platino a granel, que es inerte, exhibe propiedades catalíticas cuando está en forma de nanopartículas; el silicio, que es un aislante a escala macroscópica, se comporta como un conductor a escala nanométrica, etc.

Síntesis de nanomateriales

La síntesis de nanopartículas con tamaño uniforme, estructura cristalina y estequiometría controlada es un gran objetivo para científicos e investigadores. Con este fin, se han desarrollado muchos métodos para sintetizar materiales nanoestructurados, que pueden clasificarse en dos categorías principales: enfoques de arriba hacia abajo y de abajo hacia arriba (Figura 1). Los procedimientos sintéticos de arriba hacia abajo comienzan con el material a granel cuyo tamaño se reduce al tamaño nanométrico mediante molienda mecánica, litografía y otras formas de energía, siendo la molienda de bolas la más utilizada. Por el contrario, en los protocolos sintéticos de abajo hacia arriba, se utilizan moléculas o componentes atómicos como unidades de construcción para el desarrollo de estructuras complejas. Este enfoque permite la síntesis de nanomateriales a través de la condensación/deposición de vapor o reacciones químicas utilizando molécula por molécula, átomo por átomo, capa por capa o agrupación por agrupación, como la dispersión coloidal y la síntesis hidrotérmica.

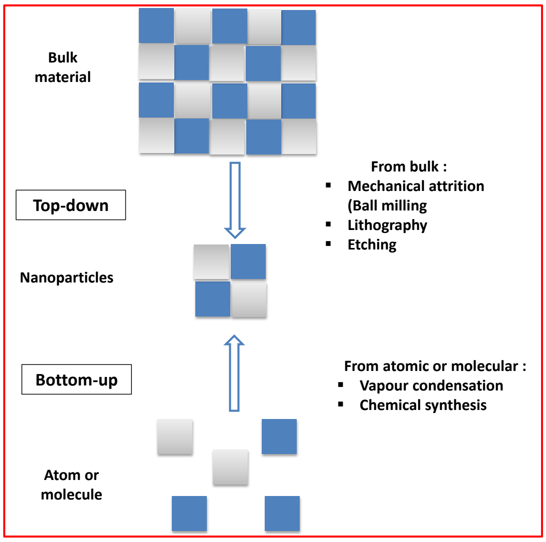

Fig. 1 Enfoques de síntesis y ensamblaje de nanomateriales

Síntesis hidrotérmica

La síntesis hidrotérmica se refiere a cualquier reacción homogénea o heterogénea en un solvente acuoso bajo condiciones controladas de temperatura y presión mediante el calentamiento de los reactivos hasta su punto crítico. La selección adecuada de temperatura, pH y concentraciones de reactivos permite un control preciso de la morfología, una distribución de tamaño de partícula estrecha y una estequiometría controlada con consecuencias posteriores en la actividad catalítica. Permite la reproducibilidad de la síntesis, la escalabilidad y un control superior de la nanoestructura. Generalmente se lleva a cabo bajo condiciones de lote utilizando autoclaves, aunque ha habido muchos intentos de establecer técnicas continuas de síntesis hidrotérmica. La frontera entre las fases vapor/líquido disminuye cerca del punto crítico; a medida que el gas se vuelve más denso y el líquido menos denso. Por encima del punto crítico, la frontera de fase desaparece y existe una fase supercrítica homogénea (Figura 2).

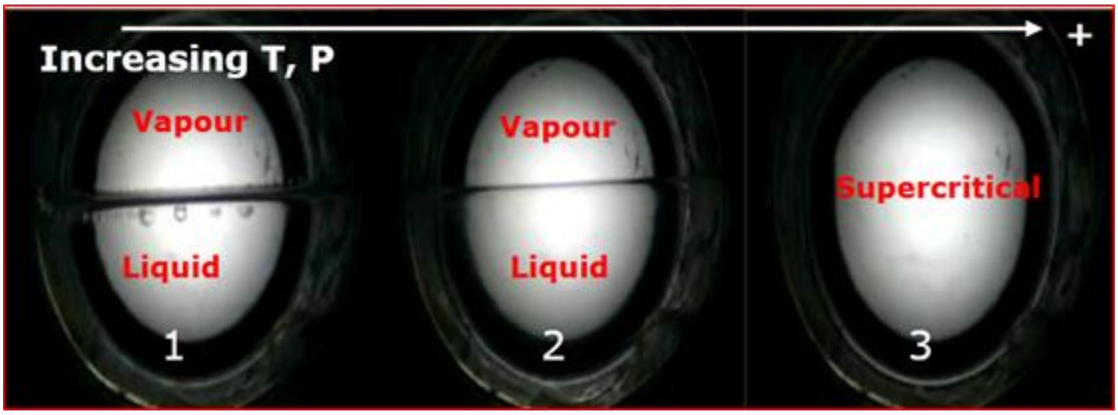

Fig. 2 Frontera de fase del fluido con temperatura y presión adaptada

Síntesis coloidal de nanopartículas plasmónicas

La aplicación de nanopartículas plasmónicas con composición, tamaño, forma y química de superficie controladas con precisión en la catálisis está atrayendo cada vez más atención. Los protocolos comunes de síntesis incluyen litografía de haz de electrones (EBL), litografía de nanoesferas (NSL) y síntesis coloidal. Esta última es una técnica de fabricación fácil con una alta capacidad para desarrollar estructuras complejas. Permite la síntesis de nanopartículas plasmónicas con diferentes formas, composiciones, tamaños y química de superficie mediante la selección adecuada de diferentes agentes capaces, agentes reductores, sistemas de disolventes y condiciones de reacción. Los metales nobles NP como el oro (Au), el platino (Pt) y la plata (Ag) se encuentran entre los materiales plasmónicos más importantes. Las NP de Ag y Au coloidales pueden experimentar una fuerte absorción en el rango espectral UV/visible debido al fenómeno de Resonancia Plasmónica Superficial Localizada (LSPR, por sus siglas en inglés). Esto resulta en bandas de absorción de plasmones superficiales intensas y un aumento del campo electromagnético local, que amplían la señal para varias aplicaciones ópticas como la dispersión superficial Raman mejorada.

Estructura híbrida utilizando el método capa por capa (LBL)

Entre estos métodos racionalistas que se han desarrollado recientemente, el método de construcción capa por capa (LBL), que se utiliza para sintetizar híbridos con nuevas funcionalidades, gracias a su flexibilidad y simplicidad, como se muestra en la Figura 3. La interacción electrostática se basa en interacciones covalentes, enlaces de hidrógeno e interacciones hidrofóbicas que pueden asegurar construcciones multicapa con propiedades fotocatalíticas novedosas. La técnica LBL permite la incorporación de una amplia gama de funcionalidades de óxidos, lo que permite la síntesis de materiales nobles para aplicaciones potenciales como materiales fotocatalíticos en la división del agua, células solares y optoelectrónicas. Recientemente, la técnica LBL ha atraído la atención de muchos investigadores debido a su estructura y función precisas. Sin embargo, existen muchos problemas asociados, como la preparación separada de nanopartículas inorgánicas antes de la adsorción electrostática, la adopción de un solvente orgánico fuerte para disolver los precursores alcoxidos reactivos y la problemática optimización de las condiciones de preparación de la solución que deben mejorarse.

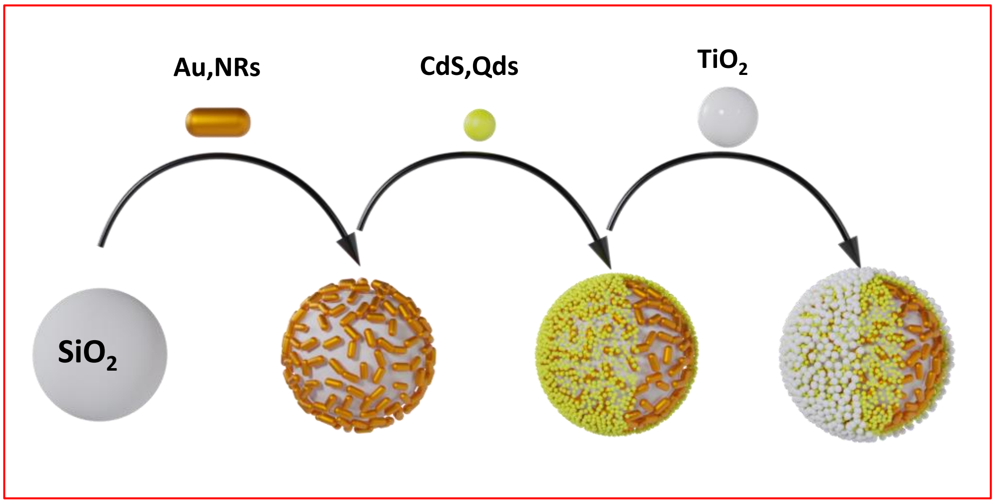

Fig.3 Ilustración esquemática de la técnica de ensamblaje LBL utilizando polielectrolitos PAH/PSS.

Nanopartículas de cobaltito de níquel.

El cobaltito de níquel (NiCo2O4) se considera uno de los materiales más prometedores en la familia de los cobaltitos con una estructura de espinela AB2O4 (A=Ni y B=Co). La química redox más alta del sistema binario sobre los óxidos metálicos individuales proviene del efecto sinérgico de los dos metales que surge de la coexistencia de las especies de Ni y Co, como se ilustra en la Figura 4. Otras ventajas incluyen su mayor conductividad, comportamiento catalítico, bajo costo, estabilidad, baja resistencia eléctrica y naturaleza respetuosa con el medio ambiente. Estas características les han permitido ser ampliamente aplicados como electrocatalizadores, materiales magnéticos, limitadores ópticos, sensores químicos y baterías de ion litio. Por lo tanto, la fabricación de NiCo2O4 nanoestructurado ha atraído recientemente mucha atención. Se han sintetizado materiales mesoporosos mediante el método asistido por microondas, mostrando promesas para futuras aplicaciones. El $NiCo_2O_4$ puede ser sintetizado en diversas morfologías mediante diferentes métodos, tales como pirólisis por pulverización, ruta de descomposición de hidróxidos coprecipitados, láser pulsado, combustión y ruta micelar inversa

(Figura 5). Entre todos estos métodos, los métodos químicos tradicionales y fáciles han sido ampliamente utilizados para sintetizar materiales en nanoescala con morfología controlada. En particular, la tecnología de tratamiento hidrotérmico es una técnica fácil, sin necesidad de utilizar ningún molde. Hasta ahora, se han sintetizado ampliamente diversas nanoestructuras de NiCo2O4 con propiedades notablemente mejoradas. Recientemente, materiales nanoestructurados de NiCo2O4 basados en morfologías huecas, mesoporosas, de nanocables y de nano-flores han demostrado propiedades electroquímicas mejoradas.

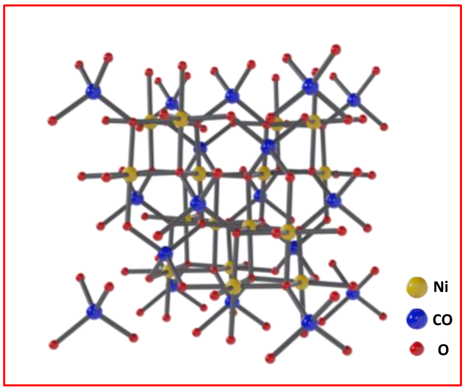

Fig. 4 Estructuras cristalinas de la celda unidad de $NiCo_2O_4$.

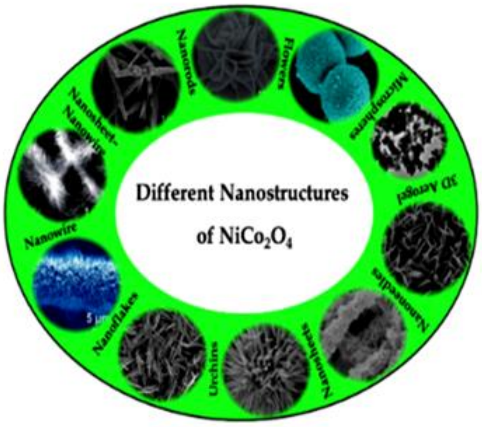

Fig. 4 Diferentes nanoestructuras de $NiCo_2O_4$.para fabricar catalizadores de alto rendimiento.

Óxidos metálicos

Las nanopartículas de óxidos metálicos han atraído una atención creciente como catalizadores, especialmente a nivel nanométrico, en una serie de aplicaciones, incluidas las aplicaciones fotocatalíticas. Los óxidos a granel son estables y tienen estructuras cristalográficas bien conocidas. Al cambiar el tamaño de las partículas, se producen cambios en las características estructurales, lo que afecta los parámetros de la red y de la celda. Además, se pueden crear subcoordinaciones de átomos (en esquinas o bordes) o vacantes de oxígeno en una nanopartícula de óxido. Por lo tanto, las nanopartículas de óxido pueden diferir considerablemente del material a granel en sus disposiciones atómicas.

Propiedades electroquímicas de los óxidos metálicos

Los óxidos de metales de transición y los polímeros conductores pueden almacenar cargas a través de una reacción redox rápida. Los principales desafíos que enfrentan los investigadores están relacionados con los óxidos de metales de transición, los polímeros conductores, la densidad de potencia, la estabilidad del ciclo y la rentabilidad. Los óxidos metálicos binarios, como el cobaltito de níquel, han atraído ampliamente a los investigadores debido a sus propiedades únicas, como su menor brecha de banda, bajo costo, no toxicidad, estabilidad térmica y química. Estas características les han permitido ser ampliamente aplicados en muchos campos.

Aplicaciones de nanopartículas de óxidos metálicos

Las nanopartículas basadas en óxidos metálicos encuentran amplias aplicaciones en sensores, fabricación de circuitos microelectrónicos, celdas de combustible, recubrimientos y catálisis, entre otros, como se ilustra en la Figura 5. Por ejemplo, los catalizadores basados en óxidos metálicos se aplican para controlar las emisiones gaseosas que provienen de la combustión de combustibles fósiles como el CO, NOx o

SOx, o en la industria de semiconductores como componente de los chips de computadora, por ejemplo. La oxidación electrocatalítica de alcoholes juega un papel interesante en las reacciones de las celdas de combustible. Los combustibles de metanol directo (DMFCs) han atraído mucha atención debido a su impacto amigable en equipos electrónicos y portátiles. Los DMFCs se pueden clasificar en alcalinos o ácidos según el tipo de electrolito. Los DMFCs alcalinos tienen más prioridad y se utilizan ampliamente debido a su bajo costo económico con su acción alcalina menos corrosiva, lo que hace que los electrodos duren más (Figura 6).

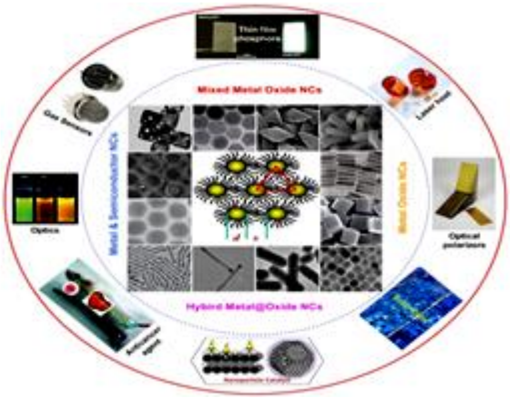

Fig. 5 Diagrama esquemático que ilustra algunas aplicaciones de los óxidos metálico.

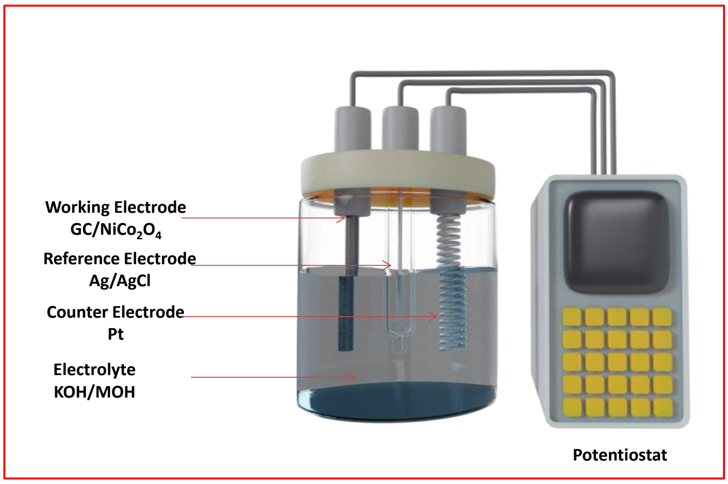

Fig. 6: Diagrama esquemático de celdas de combustible de metanol directo de tres electrodos.

Nanopartículas de dióxido de titanio

El dióxido de titanio (TiO2) fue descubierto por primera vez en ilmenita en 1791. También se conoce como titania. El TiO2 es un semiconductor de tipo n que se encuentra en la naturaleza como anatasa, brookita y rutilo, con brechas de banda de 3,2 eV, 3,2 eV y 3,0 eV, respectivamente, y fue fabricado comercialmente por primera vez en 1916 como un pigmento blanco. Las nanopartículas de TiO2 pueden sintetizarse utilizando diferentes técnicas para obtener diferentes dimensiones que van desde 0D hasta 3D. Las nanopartículas de TiO2 han atraído mucha atención en comparación con los materiales a granel, ya que proporcionan una relación volumen superficial más alta y un área superficial mayor. El uso del plasmónico es una manera efectiva de mejorar el rendimiento de las células solares y los fotocatalizadores. La irradiación de luz visible de metales nobles nanoacoplados con semiconductores muestra una oscilación colectiva de los electrones de conducción del plasmón sobre los semiconductores, lo que afecta significativamente la distribución de energía electromagnética, lo que cambia significativamente la actividad fotocatalítica y la respuesta del semiconductor en la región visible.

Sulfuros metálicos

Recientemente, los sulfuros metálicos han ganado mucho interés debido a sus propiedades y estructuras únicas. Tienen un papel importante en las baterías secundarias, lubricantes, catálisis y semiconductores.

CdS, QDs, y su papel en mejorar la actividad fotocatalítica

Un objetivo clave en la investigación de nanomateriales es la incorporación de múltiples funcionalidades de diferentes materiales a escala nanométrica dentro de una estructura controlando e integrando la organización espacial. Los puntos cuánticos semiconductores en la tabla periódica son aquellos que tienen átomos de los grupos II-VI o III-V, con dimensiones físicas menores de 20 nm. Los puntos cuánticos de CdS han atraído mucha atención en las últimas décadas debido a sus excelentes características, como altos coeficientes de absorción, grandes momentos dipolares intrínsecos, mejor fotostabilidad en comparación con las etiquetas fluorescentes tradicionales y espectros de emisión más estrechos y simétricos.

2- **Equilibrio entre la mejora del campo cercano y la inyección de portadores calientes: Fotocatálisis plasmónica en ensamblajes de transferencia de energía en cascada**.

La fotocatálisis se presenta como una alternativa muy prometedora a la fotovoltaica para aprovechar la energía solar, almacenándola en productos químicos a través de un proceso de un solo paso. Un obstáculo central para su amplia implementación es su baja eficiencia de conversión, lo que motiva la investigación en diferentes campos para lograr un avance en esta tecnología. El uso de materiales plasmónicos para fotosensibilizar fotocatalizadores semiconductores tradicionales es una estrategia popular cuyo potencial completo aún no se ha explotado por completo. En este trabajo, utilizamos puntos cuánticos de CdS como un sistema puente, cosechando energía de nanoestructuras de Au y entregándola a nanopartículas de TiO_2 que sirven como centros catalíticos. Los puntos cuánticos pueden hacerlo al convertirse en un paso intermedio en una cascada de transferencia de carga iniciada en el sistema plasmónico, o al crear pares electrón-hueco a una tasa mejorada debido a su interacción con el campo cercano mejorado creado por las nanopartículas plasmónicas. Nuestros resultados muestran una aceleración significativa en la reacción al combinar estos elementos en fotocatalizadores coloidales híbridos que promueven el efecto de mejora del campo cercano, y mostramos cómo diseñar complejos que explotan este enfoque. Al hacerlo, también exploramos la compleja interacción entre los diferentes mecanismos involucrados en el proceso fotocatalítico, destacando la importancia de la morfología de las nanopartículas de Au en sus capacidades fotosensibilizadoras.

Resultados y discusión

Como se ilustra en la Figura 7a, las NPs de TiO2 comerciales y los QDs de CdS preparados tienen brechas de energía de 3,3 eV y 2,6 eV, respectivamente. Hemos sintetizado cuatro tipos diferentes de NPs de Au para integrarlos en las nanoestructuras híbridas basadas en TiO2/CdS reportadas aquí. Estos cuatro sistemas se crearon para explorar dos aspectos diferentes de la contribución de los PNP: (i) eligiendo la longitud de onda del principal LSPR, y (ii) si pueden contribuir a través de HEI. En primer lugar, y teniendo su principal LSPR en el espectro visible, creamos nanoesferas de oro desnudas y recubiertas de sílice (AuNS y AuNS@SiO2) con firmas plasmónicas centradas en 523 y 535 nm, respectivamente (espectros rojo y naranja, Figura 7b) y con un diámetro original de AuNS fijo en 23 nm (Figura 7c). En segundo lugar, y teniendo su principal LSPR en el NIR, creamos nanorodillos de oro desnudos y recubiertos de sílice (AuNR y AuNR@SiO2) con bandas plasmónicas longitudinales centradas en 856 y 871 nm, respectivamente (espectros marrón y morado, Figura 7b) y con una relación de aspecto de 4,15 (54 x 13 nm, Figura 7d).

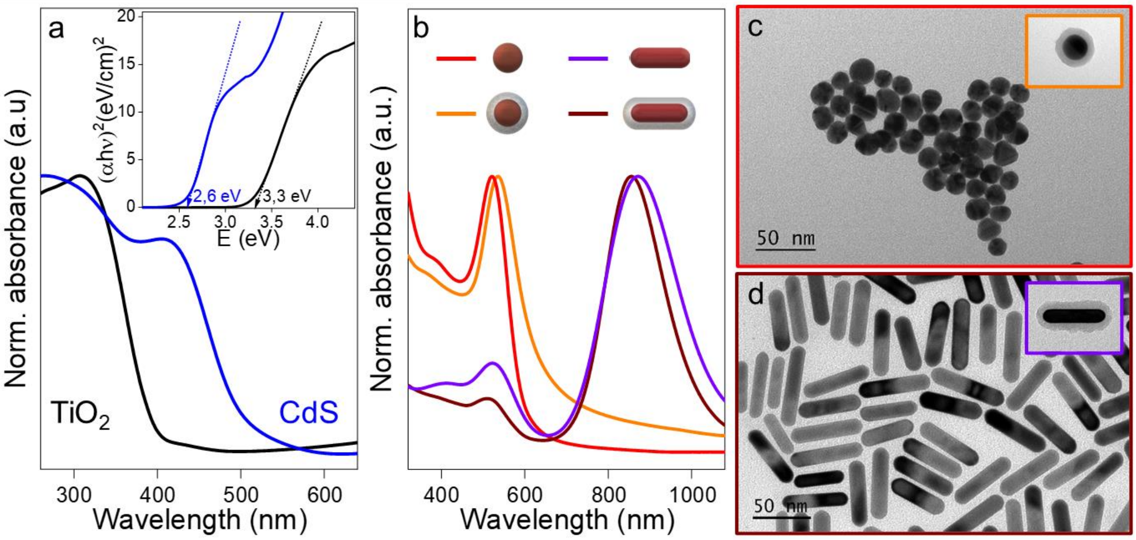

Fig. 7 (a) Espectros de absorbancia resultantes de la absorción de semiconductor y cálculo del intervalo de banda (gráfico de Tauc) de NP de TiO_2 (negro) y QDs de CdS (azul). (b) Espectros de absorbancia normalizados de AuNS (rojo), AuNS@SiO_2 (naranja), AuNR (marrón) y AuNR@SiO_2 (púrpura). (c,d) Imágenes TEM de los AuNS y AuNR, respectivamente (insertadas en la parte superior derecha, las partículas recubiertas de sílice)

En el caso de las nanopartículas recubiertas de sílice, la absorción máxima se desplaza a longitudes de onda más altas, con respecto a las NPs de Au originales, como resultado del aumento de los índices de refracción una vez que las NPs de Au están recubiertas por la cáscara de SiO_2. En ambas NPs de Au@SiO_2, la cáscara de SiO2 fue homogénea, y el grosor fue de 8 nm (Figura 8). En consecuencia, los resonadores desnudos estarán en contacto directo con los ensamblajes de QDs/TiO2 mostrando un mecanismo dominante de inyección de electrones calientes mientras que los resonadores recubiertos de sílice mostrarán un mecanismo puro de transferencia de energía plasmónica debido a su cáscara de sílice aislada. Además, al utilizar tanto AuNS como AuNR, podemos comparar la excitación plasmónica desde diferentes regiones del espectro electromagnético.

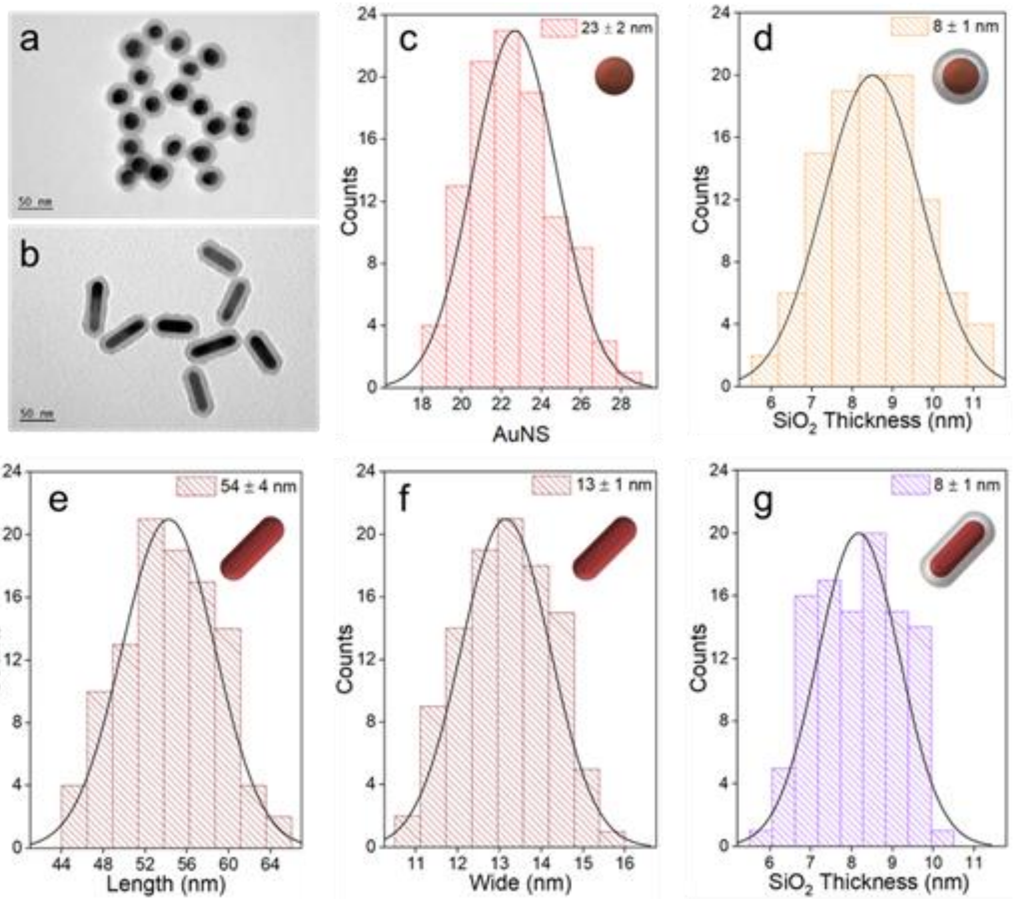

Fig. 8 (a,b) Imágenes TEM de AuNS@SiO_2 y AuNR@SiO_2, respectivamente. (c,d) Histogramas de tamaño del núcleo y la cáscara en AuNS@SiO_2. (e-g) Histogramas de tamaño del núcleo y la cáscara en AuNR@SiO_2

La eficiencia fotocatalítica de los nanocompuestos sintetizados se ha evaluado mediante la fotodegradación de Rodamina B (RhB) y la deshidrogenación del ácido fórmico como reacciones modelo Figura 9. De esta manera, la degradación de RhB en presencia de los híbridos se monitoreó siguiendo la disminución del máximo de absorción de este colorante (λmax = 554 nm) en función del tiempo. Con la adición de AuNS y AuNR en los ensamblajes, la degradación aumenta a un 39,48 % y 48,77 %, respectivamente (líneas roja y marrón, Figura 10b). Interesantemente, el uso de catalizadores con AuNS@SiO2 y AuNR@SiO2 conduce a una degradación del 93,96 % y 56,97 %, respectivamente. Cuando depositamos las nanopartículas de AuNS@SiO2 en la capa intermedia entre los QDs de CdS y las NP de TiO2, la degradación final disminuye del 93,96 % al 50,04 % (círculos naranjas llenos y huecos, respectivamente). Estos resultados respaldan la interpretación de que los QDs de CdS sirven como una vía de energía entre los PNP y el TiO2.

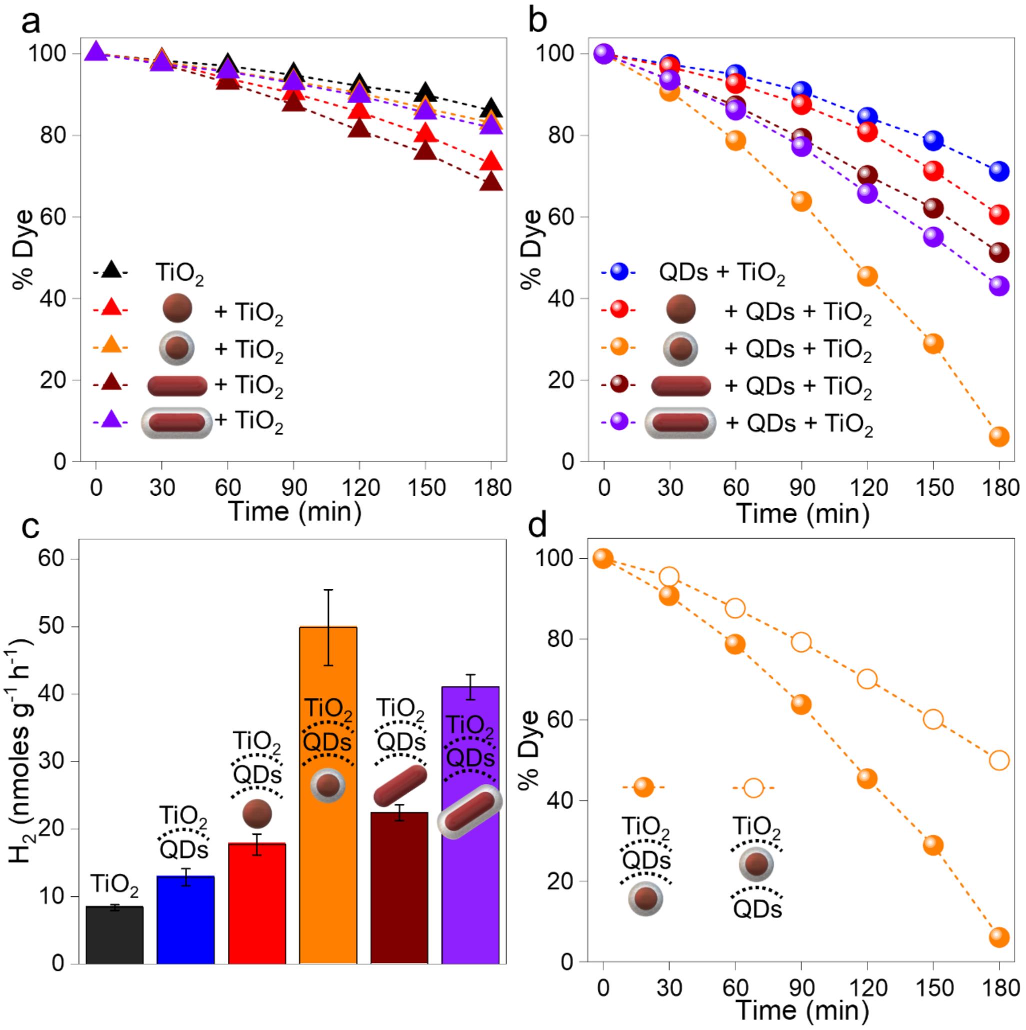

Fig. 9 Degradación fotocatalítica de RhB en presencia de los híbridos con TiO_2 (a) y con CdS y TiO2 (b). (c) Generación fotocatalítica de hidrógeno asistida por ácido fórmico en presencia de diferentes híbridos (nanomoles de H_2 por mg de catalizador en 1 hora de reacción). (d) Degradación fotocatalítica de RhB en presencia del catalizador compuesto por AuNS@SiO_2, CdS y TiO_2 cambiando el orden del ensamblaje L-B-L (AuNS@SiO2/CdS/TiO_2, círculos naranjas y CdS/AuNS@SiO2/TiO_2, círculos blancos). En todos los paneles, el catalizador con TiO2 solo se representó en negro y el catalizador con CdS y TiO_2 solo se representó en azul; el catalizador con AuNS, AuNS@SiO_2, AuNR, AuNR@SiO_2 se representó en rojo, naranja, marrón y púrpura, respectivamente (triángulos para experimentos de control sin CdS y círculos para híbridos con CdS y TiO_2). P = 1.0 atm, T = 25 °C y λ = 350-2400 nm.

Centrando ahora nuestra atención en los fenómenos que subyacen a la reacción en las diferentes configuraciones, podemos explicar la mayor actividad fotocatalítica de los híbridos cargados con PNP teniendo en cuenta el mecanismo principal de fotoactivación de cada sistema. En los híbridos con NPs de Au desnudas (Figura 10), La excitación plasmónica produce una población de "electrones calientes" que pueden ser inyectados desde la banda de conducción de las NPs de Au hacia la banda de conducción de los QDs de CdS y, finalmente, transferidos a la banda de conducción de las NPs de TiO2. Para ampliar nuestra discusión sobre el papel que tiene el mecanismo de fotosensibilización en estos híbridos, complementamos los resultados experimentales con simulaciones computacionales de AuNR y AuNS modelados utilizando las formas y tamaños de las muestras experimentales. En resumen, hemos desarrollado un protocolo de ensamblaje jerárquico capa por capa altamente efectivo para la creación de nanoestructuras híbridas fotocatalíticas avanzadas. La combinación estratégica de PNP con QDs de CdS ha resultado en un aumento significativo de la actividad fotocatalítica observada en las NPs de TiO2. Hemos demostrado que los QDs de CdS utilizan eficazmente el aumento del campo cercano del metal, resaltando la importancia de la superposición espectral entre el plasmón y el semiconductor. Nuestros resultados indican que enfocarse en el aumento del campo cercano de los QDs de CdS, facilitando la transferencia de energía de los PNP recubiertos de SiO2 a TiO2 mediante una transferencia de carga indirecta iniciada en los QDs, produce las tasas de reacción más altas. Además, hemos comparado diferentes secuencias de deposición de elementos de fotocatalizador y hemos destacado la importancia de maximizar la cobertura de la superficie de PNP con grupos de CdS-QD@TiO2-NP para aprovechar al máximo este mecanismo de activación indirecta. Nuestro estudio también revela cómo la geometría de los PNP puede afectar la eficiencia fotocatalítica, siendo los AuNRs una opción superior en ciertos casos. Sin embargo, la retrotransferencia de electrones puede afectar negativamente la eficacia en ciertas configuraciones. En conjunto, estos hallazgos ofrecen una visión detallada de los diferentes mecanismos de transferencia de energía en los sistemas fotocatalíticos plasmónicos híbridos y subrayan la necesidad de futuros estudios de nanoingeniería para optimizar las contribuciones de cada componente.

En conclusión, hemos desarrollado un protocolo efectivo para la creación de nanoestructuras híbridas fotocatalíticas avanzadas, combinando PNP con QDs de CdS para aumentar significativamente la actividad fotocatalítica de las NPs de TiO2. Nuestros hallazgos resaltan la importancia del campo cercano del metal y la superposición espectral entre el plasmón y el semiconductor en estos sistemas. Además, identificamos la transferencia de energía de los QDs de CdS como un mecanismo crucial para mejorar las tasas de reacción. La optimización de la cobertura de superficie de PNP con grupos de CdS-QD@TiO2-NP resultó ser esencial para maximizar esta transferencia de energía. Nuestro estudio también revela la influencia de la geometría de los PNP en la eficiencia fotocatalítica, destacando la superioridad de los AuNRs en ciertos casos. Estos hallazgos proporcionan una comprensión detallada de los mecanismos de transferencia de energía en los sistemas fotocatalíticos plasmónicos híbridos y señalan la importancia de futuros estudios de nanoingeniería para optimizar estas estructuras.

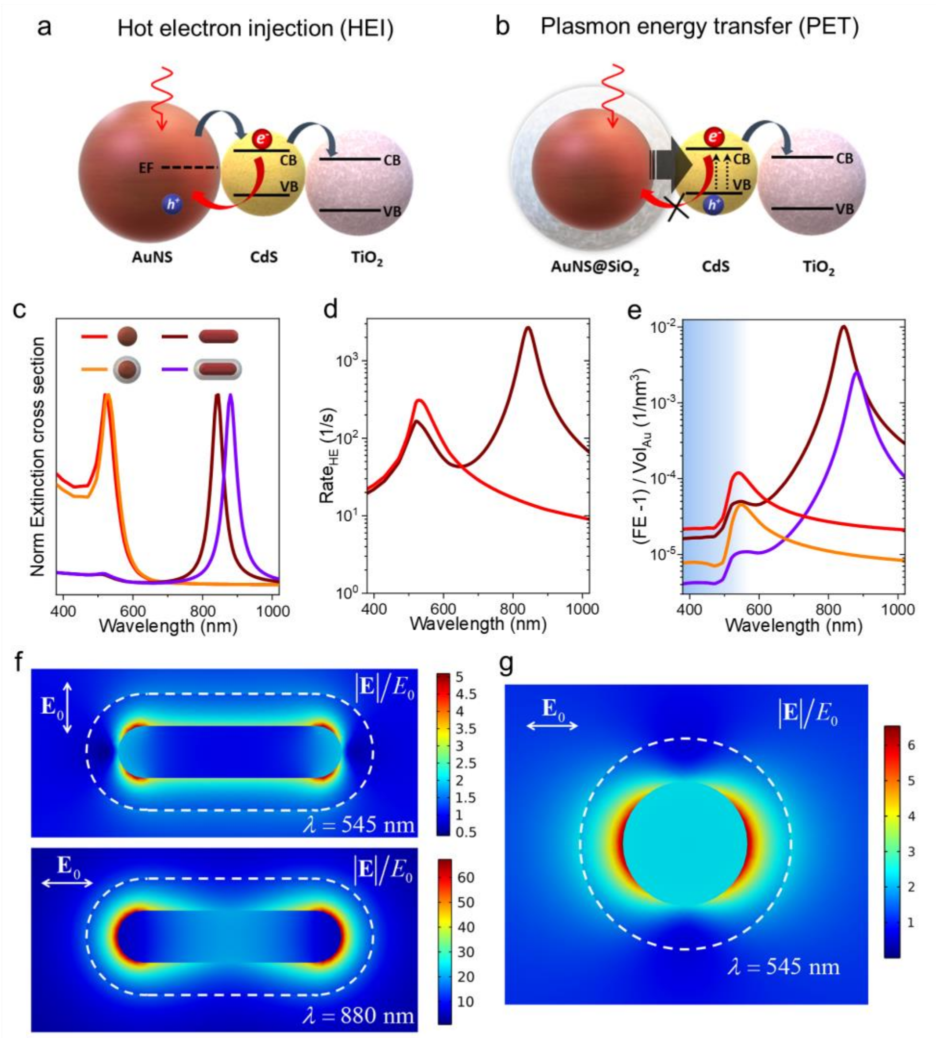

Figura 10. (a) Representación del mecanismo de inyección de electrones calientes (HEI) en el híbrido compuesto por AuNS/CdS-QDs/TiO_2 (panel superior) y transferencia de energía por transferencia de electrón de excitación (PET) en el híbrido compuesto por AuNS@SiO_2/CdS-QDs/TiO_2 (panel inferior). (b) Secciones transversales teóricas de extinción de AuNS, AuNS@SiO_2, AuNR y AuNR@SiO_2. (c) Tasa de excitación de portadores calientes intrabanda para AuNS y AuNR desnudos. (d) Mejora promedio del campo eléctrico (eq. 1) y (e) mejora promedio del campo eléctrico, referenciada a cero y normalizada por el volumen de Au de cada partícula. La región azul en los paneles d y e indica la región espectral con absorción no nula de QD. En todas las figuras, AuNS, AuNS@SiO_2, AuNR y AuNR@SiO_2 se representaron en rojo, naranja, marrón y morado, respectivamente. (f,g) Mapas de campo eléctrico para los modos transversales y longitudinales de AuNR@SiO_2 (f) y para el modo plasmónico de AuNS@SiO_2 (g). El límite externo de la capa de SiO_2 está resaltado con una línea punteada blanca.

3- **Conversión electrocatalítica selectiva de metanol a formiato sobre óxido mixto de cobalto-níquel**

La oxidación del metanol a formiato ha captado una mayor atención debido a su mayor valor económico en comparación con la propia pila de combustible y se considera un químico esencial en muchos sectores, como las industrias textil, farmacéutica y de impresión. Actualmente, el ácido fórmico se produce industrialmente mediante la reacción del metanol con CO a alta presión y temperatura, lo que hace que su producción sea prohibitiva en términos de costos. En este estudio, variando la temperatura de reacción, el tipo de surfactante y la relación estequiométrica Co:Nii (1:1, 2:1 y 3:1), se prepararon fase pura de cobaltita de níquel y fases mixtas de nanoláminas de cobaltita de níquel con óxido de níquel mediante síntesis hidrotermal. Las nanopartículas sintetizadas exhiben una conversión electroquímica de metanol a formiato de casi el 100% en condiciones normales de presión y temperatura. Cuando se utiliza CoNi (2:1) como ánodo para la oxidación electrocatalítica de metanol, se alcanza el valor de densidad de corriente más alto hasta ahora (290 mA/cm^2 a 0.65 V (vs. RHE)) en 1 M KOH y 2 M de metanol. Además, el material con mejor desempeño retiene el 100% de la densidad de corriente anódica inicial durante 33 horas, superando a los catalizadores más avanzados para esta reacción. Una batería de técnicas de caracterización, incluyendo XRD, EDS, SEM, HRTEM, XPS y voltametría de CO, nos permitió racionalizar las razones detrás de este comportamiento, que se relacionan principalmente con la mayor cantidad de sitios activos. Este trabajo proporciona una forma sencilla y eficiente de convertir metanol en materiales orgánicos de mayor valor y la primera evidencia de una vía de reacción selectiva hacia formiato, abriendo nuevas oportunidades para el diseño de materiales novedosos para la producción de bienes de consumo.

Resultados y discusión

Los resultados de ICP-OES demuestran que la relación molar real de las muestras, es decir, 1.1, 2 y 3.2 para CoNi 1:1, CoNi 2:1 y CoNi 3:1, respectivamente, coincide con los valores nominales. La Figura 11 ilustra los patrones de difracción de rayos X de los sintetizados CoNi 1:1, CoNi 2:1 y CoNi 3:1. CoNi 3:1 exhibe los picos de difracción característicos de la fase cristalina NiCo2O4 (JCPDS 20-0781). Estos picos están ligeramente desplazados hacia ángulos más bajos para las muestras CoNi 1:1 y CoNi 2:1, lo que indica que ambas fases, NiCo2O4 y NiO (JCPDS 47-1049), existen juntas.

La morfología de las muestras se observó mediante análisis con microscopía electrónica de barrido de emisión de campo. La Figura 12(a-c) muestra las imágenes FE-SEM de CoNi 1:1, CoNi 3:1 y CoNi 2:1. Se observa claramente que el óxido mixto de cobalto-níquel tiene una estructura en forma de lámina en todos los casos.

Las imágenes TEM de las nanopartículas CoNi 1:1, CoNi 3:1 y CoNi 2:1 se ilustran en la Figura 13. Las nanopartículas de óxido mixto de cobalto-níquel sintetizadas bajo condiciones controladas de presión y temperatura exhiben una estructura esférica. Estas morfologías son consistentes con las reportadas en la literatura y son corroboradas por las imágenes obtenidas mediante Microscopía Electrónica de Barrido de Emisión de Campo (FE-SEM). El histograma de distribución del tamaño de las partículas de los polvos preparados y los diámetros promedio estimados de las partículas fueron de 9.35, 9.4 y 9.31 nm para CoNi (1:1, 3:1 y 2:1), respectivamente.

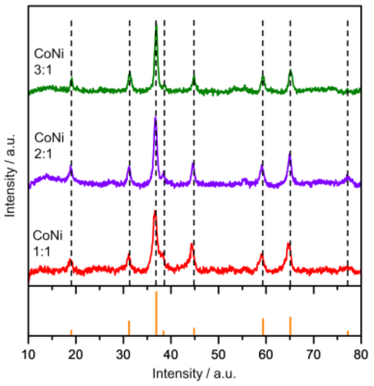

Fig. 11 Difracción de rayos X de CoNi 1:1, CoNi 2:1 y CoNi 3:1.

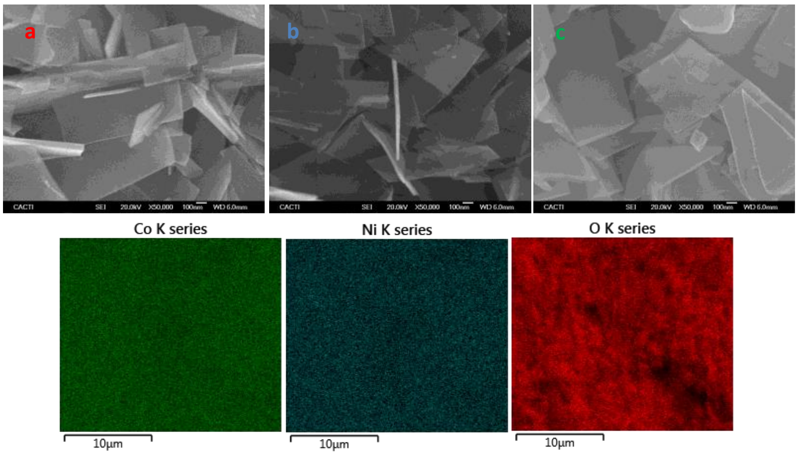

Fig. 12 Imágenes FE-SEM de a- CoNi 1:1, b- CoNi 2:1 y c- CoNi 3:1, con imágenes de mapeo de elementos de nanoláminas CoNi 2:1 de Co, Ni y O.

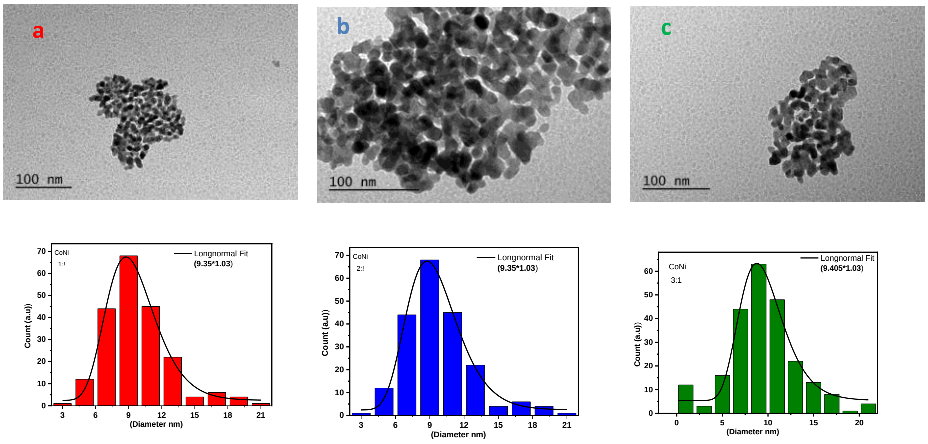

Fig. 13 Imágenes TEM de a- CoNi 1:1, b- CoNi 2:1 y c- CoNi 3:1, con su respectivo histograma de distribución del tamaño de partículas depositado.

Cyclic voltammetry (CV) analysis was followed up. Figure 14 shows the electrochemical activity of CoNi 1:1, CoNi 3:1, and CoNi 2:1 nanoparticles over a glassy carbon (GC) modified electrode. All the prepared materials were tested in 1.0 M KOH solution at a scan rate of 50 mV/s and room temperature in the potential range between 0.9 and 1.7 V (vs. RHE). La mayor actividad electrocatalítica de CoNi 2:1 sobre los otros electrodos podría atribuirse a una mayor tendencia a formar estructuras porosas.

La producción de formiato a partir de metanol utilizando un catalizador de cobalto (Co) en un proceso electroquímico puede lograr una alta selectividad y eficiencia cuando se optimiza. Sin embargo, aumentar la cantidad de Co más allá de un nivel óptimo disminuye la eficiencia, como en el caso de CoNi 3:1. En la Figura 15, se observa claramente que la concentración de formiato aumentó en todos los casos con el tiempo de paso de corriente, es decir, con la cantidad total de carga fluída. Además, la concentración de formiato es mayor en el caso de CoNi 2:1 que en los otros catalizadores preparados.

La composición de fase y la estructura del CoNi antes y después de la exposición catalítica fueron examinadas mediante difracción de rayos X en polvo (XRD). Como se muestra en la Figura 16. Después de 40 horas de reacción catalítica, el precursor de Ni-Co interactuó con la solución de reacción formando otros picos. Li et al. registran que el pico a 25° ocurre debido al carbono apilado de los materiales anódicos, derivado de la descomposición incompleta de los ingredientes orgánicos. Mientras que el pico alrededor de 35º puede estar relacionado con la presencia de Ni1-xCox(OH)2. Se estudió la estabilidad de los electrodos sintetizados y los resultados mostraron que la corriente de oxidación del metanol muestra una mayor estabilidad hasta las 33 horas, asegurando la mayor estabilidad de los electrodos preparados.

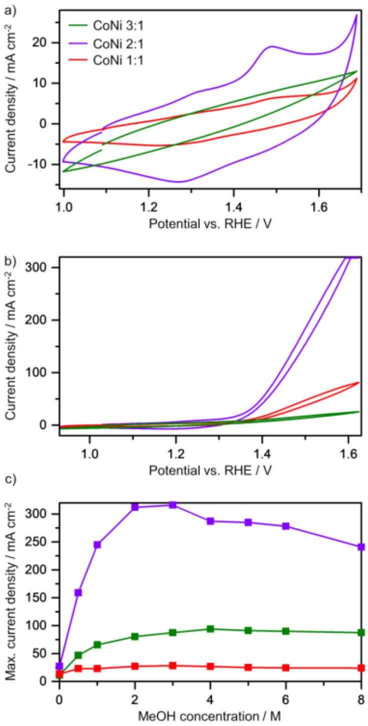

La Figura 14 muestra los voltamperogramas cíclicos de CoNi 1:1, CoNi 2:1 y CoNi 3:1.

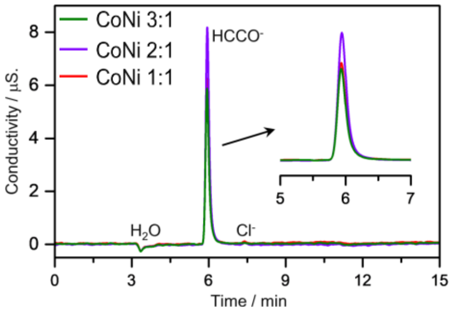

Fig.15 IC profile in 1 M KOH containing 2 M methanol during 10 000 s CP testing obtained at 2000 s intervals of CoNi 1:1, CoNi 2:1 and CoNi 3:1.

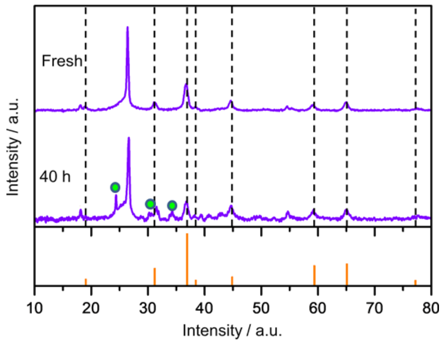

La Figura 16 presenta el patrón de difracción de rayos X (XRD) del CoNi 2:1 antes y después de 40 horas de la prueba de estabilidad de los cronoamperogramas.

La química superficial del polvo de CoNi 2:1, pulverizado sobre papel de carbono después de 40 horas de reacción catalítica, se verificó mediante mediciones de (XPS), Figura 17. Basándose en los resultados del cálculo, se encontró que la relación de Co^{3+} a Co^{2+} del polvo de CoNi 2:1 y depositado sobre papel de carbono era solo de 1.4 en su superficie, lo cual está lo suficientemente cerca de su relación estequiométrica de 2:1. Mientras que la de las películas después de someterse a 40 horas de reacción catalítica, la relación disminuyó hasta 0.94, lo que puede atribuirse a la inestabilidad de Co^3+ en la superficie. Es bien sabido que las especies trivalentes en los óxidos metálicos de espinela se consideran los sitios activos para reacciones catalíticas y la sustitución de Ni mejora la estabilidad de Co^{3+} en la superficie. Además, se observan claramente los picos de potasio, que aumentan con el tiempo de reacción, confirmando la formación de la fase de perovskita.

Para aclarar la brecha catalítica entre CoNi 2:1 y otros catalizadores utilizados para producir formiato, se ha utilizado la voltametría de desprendimiento de CO, Figura 18. La superficie reactiva y la fuerza de interacción CO-metal pueden detectarse. Es bien sabido que los catalizadores con los sitios activos más grandes adsorben una mayor cantidad de CO y muestran un pico de oxidación más alto, como en el caso de CoNi 2:1. Este estudio investigó la síntesis hidrotermal de nanoláminas de cobaltita de níquel ($NiCo_2O_4$), produciendo fases puras y mixtas con óxido de níquel. Las nanopartículas resultantes demostraron una conversión electroquímica casi del 100% de metanol a formiato, con CoNi (2:1) mostrando la mayor densidad de corriente y estabilidad superior durante 33 horas. Los estudios electroquímicos confirmaron su rendimiento superior sobre otros ratios (1:1 y 3:1), destacando la forma rectangular ideal en los perfiles de voltametría cíclica. El análisis de difracción de rayos X reveló interacciones entre el precursor Ni-Co y la solución de reacción, mientras que la voltametría de desprendimiento de CO mostró una mayor adsorción de Co en CoNi

(2:1). En resumen, las nanoláminas de CoNi (2:1) muestran un gran potencial como electrocatalizadores estables y eficientes para la oxidación de metanol.

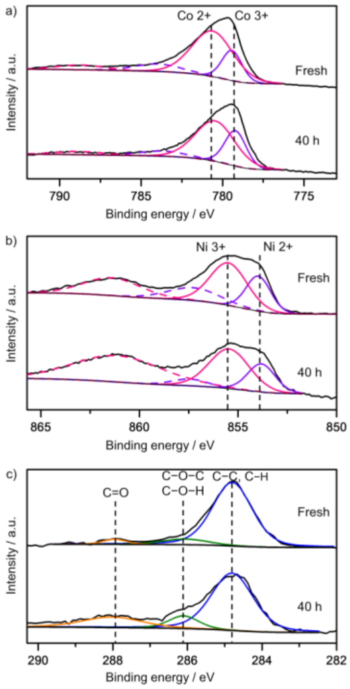

Figura 17 Patrón XPS del muestra fresca de CoNi 2:1 y después de 40 h de prueba de estabilidad de cronoamperogramas.

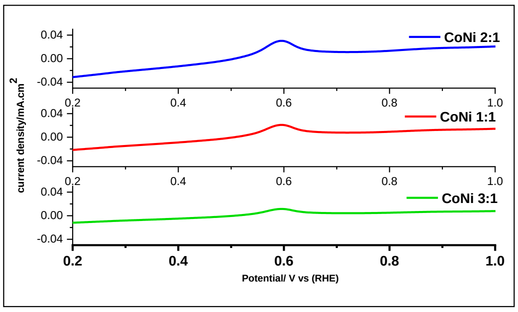

Figura 18 oltametría de desprendimiento de CO a un potencial aplicado de 1.65 V RHE.